1-1-2008

Mechanical properties of wrought magnesium alloys

Sanjida Begum
Ryerson University

MECHANICAL PROPERTIES OF WROUGHT MAGNESIUM ALLOYS

By

SANJIDA BEGUM

Bachelor of Science in Mechanical Engineering

Bangladesh University of Engineering and Technology (BUET), 2003

A thesis presented to Ryerson University

in partial fulfillment of the requirements for the degree of

Master of Applied Science in the program of Mechanical Engineering

Toronto, Ontario, Canada, 2008

AUTHOR'S DECLARATION

I hereby declare that I am the sole author of this thesis.

I authorize Ryerson University to lend this thesis to other institution or other individuals for the purpose of scholarly research.

Sanjida Begum _____

I further authorize Ryerson University to reproduce this thesis by photocopying or by other means, in total or in part, at the request of other institutions or individuals for the purpose of scholarly research.

Sanjida Begum _____

BORROWER'S PAGE

Ryerson University requires the signature of all persons using or photocopying this thesis.

Please sign below provide address and date.

Name	Signature	Address	Date

MECHANICAL PROPERTIES OF WROUGHT MAGNESIUM ALLOYS

Sanjida Begum

MASc., Mechanical Engineering

Abstract

Lightweight magnesium alloys are being increasingly used in automotive and other transportation industries to achieve energy efficiency. The objective of this thesis was to study the mechanical properties of two wrought alloys AZ31 and AM30. With increasing strain rate the yield strength and ultimate tensile strength increased and the strain hardening exponent decreased for AM30 and increased for AZ31. Both alloys exhibited stable cyclic characteristics at lower strain amplitudes and cyclic hardening characteristics at higher strain amplitudes. The Bauschinger effect was pronounced at higher strain amplitudes, resulting in asymmetric hysteresis loops in both alloys. The influence of strain ratio (R_S), strain rate, and initial straining direction on the cyclic deformation characteristics and fatigue life was evaluated. At low R_S, both alloys exhibited strong cyclic hardening, which decreased as R_S increased. Fatigue crack initiation was observed to occur from the specimen surface and crack propagation was basically characterized by striation-like features.

ACKNOWLEDGEMENTS

I would like to thank my supervisor Dr. Daolun Chen for his guidance, support and encouragement during my studies at Ryerson University. I would also like to thank Dr. S. Xu, CANMET-Materials Technology Laboratory, Natural Resources, Ottawa, Ontario, Canada; Dr. Alan A. Luo from General Motors Research and Development Center, Warren, MI , USA and Professor S.D. Bhole for their helpful discussion.

I would also like to thank the National Sciences and Engineering Research Council of Canada (NSERC) and AUTO21 for providing financial support. This investigation involves part of the Canada-China-USA Collaborative Research Project on the Magnesium Front End Research and Development (MFERD), and financial support from CANMET-MTL is also acknowledged.

I would like to extend my thanks to all my friends and colleagues at Ryerson University for helping me and keeping my spirits up. Special thanks to A. Machin, J. Amankrah, Q. Li and R. Churaman for their strong support in providing easy access to the facilities.

Words cannot express my deepest gratitude towards my parents and towards my siblings. I would also like to thank my husband for his support and help during my graduate study.

To

My Parents

Mrs. Mazeda Khatun, Md. Mohsin Ali

TABLE OF CONTENTS

LIST OF TABLES

LIST OF FIGURES

NOMENCLATURE

Acronym Definition

Al	Aluminum
ASTM	American Society for Testing of Materials
BCC	Body centered cubic
Cu	Copper
ED	Extrusion direction
EDS	Energy dispersive X-ray spectroscopy
FCC	Face centered cubic
Fe	Iron
HCF	High cycle fatigue
HCP	Hexagonal closed packed
HV	Vickers hardness
LCF	Low cycle fatigue
Mg	Magnesium
Mn	Manganese
Ni	Nickel
SEM	Scanning electron microscope
TD	Transverse direction
USAMP	United states automotive materials partnership
UTS	Ultimate tensile strength

YS	Yield strength
Zn	Zinc

Symbol Definition

σ	Stress, MPa
ε	Strain
n	Strain hardening exponent
E	Young's modulus of elasticity, GPa
$\left(\frac{\Delta\varepsilon_t}{2}\right)$	Total strain amplitude
$\left(\frac{\Delta\varepsilon_e}{2}\right)$	Elastic strain amplitude
$\left(\frac{\Delta\varepsilon_p}{2}\right)$	Plastic strain amplitude
β	Cyclic strain hardening coefficient
N	Number of cycles
N_f	Number of cycles to failure
n'	Cyclic strain hardening exponent
K'	Cyclic strength coefficient, MPa
σ'_f	Fatigue strength coefficient, MPa
b	Fatigue strength exponent

$\varepsilon_f^{'}$	Fatigue ductility coefficient, %
c	Fatigue ductility exponent
R_s	Strain ratio
ε_{max}	Maximum strain
ε_{min}	Minimum strain
$\dot{\varepsilon}$	Strain rate

CHAPTER 1

INTRODUCTION

Except for the fact that magnesium alloys have limited formability due to the hexagonal close-packed (HCP) crystal structure, their light weight trait (density: 1.7 gm/cc versus 2.7 gm/cc for aluminum and 7.8 gm/cc for steel), high strength-to-weight ratio and good damping capacity have made these alloys more desirable than conventional structural materials – steels and aluminum alloys [1-4]. Rising concern about global warming that is directly affected by vehicle emissions can be reduced to an extent if the total weight of each car can be decreased. A report published by USAMP (United States Automotive Materials Partnership) expressed the vision of increasing the use of magnesium alloys by 340 lbs per car by the year of 2020 (only about 10~12 lbs of magnesium alloys were used in a typical car in 2006), which will lead to a substantial reduction of the car weight (about 15%). To achieve that goal, it is essential to develop high strength wrought magnesium alloys with good formability as a substitute of some structural parts considered.

Currently, the majority of the magnesium alloys used in car body parts are cast alloys because of their high productivity, even though wrought magnesium alloys normally provide better properties in terms of strength than the cast magnesium alloys. Substantial progress has been made in the last few years in the development of wrought magnesium alloys. The extrusion process results in a large range of possible geometries, with a combination of different shapes. This feature reduces the number of joints and eliminates

fabrication costs. Because of this magnesium extruded bars and shapes, either standard or special cross-sections can successfully compete in cost with other materials [2].

Still now, mechanical properties of some wrought Mg alloys are not properly defined, and, specially there is limited strain-controlled low cycle fatigue data available [5-13]. To increase the formability of magnesium alloys, numerous efforts have been made. Recent development of a new wrought magnesium alloy, AM30, by General Motors Research and Development Center [14], has certainly appended to some increasing properties. Experimental results showed that AM30 magnesium alloy has better formability than AZ31 alloy, leading to a higher productivity in manufacturing automotive components. While a material in the automotive applications would inevitably be subjected to alternating loading, so far no work has been reported on the low cycle fatigue behavior of AM30 alloy, in spite of a limited number of publications available on the fatigue behavior of other magnesium alloys, e.g., AZ31 [5, 6, 11], ZK60 [8], AZ91 [9] and AM50 [12].

The objective of this study is to evaluate the mechanical properties of two wrought Mg alloys, namely, AZ31 and AM30. Both of these alloys were provided by General Motors Research and Development Center. This investigation also compares the microstructure, micro-hardness, tensile properties, low cycle fatigue properties, monotonic and cyclic strain hardening exponent and cyclic deformation characteristics of AZ31 and AM30 alloys at different test conditions.

A literature survey is presented in Chapter 2 on Mg alloys, their properties and current uses; the microstructural characterization and evolution of mechanical properties of AZ31 and AM30 wrought alloys after tensile and low cycle fatigue tests are also included. Chapter 3 gives the experimental procedures involved in this study. Chapters 4 and 5 presents the test results obtained in this work. Microstructural characterization, micro-hardness, tensile and fatigue properties of extruded AZ31 and AM30 are presented and analyzed in Chapter 4 and Chapter 5, respectively. Chapter 6 presents conclusions and future scope of the relevant work.

CHAPTER 2

LITERATURE REVIEW

2.1 Magnesium and Its Alloys

Magnesium was discovered and isolated by Sir Humphrey in 1808, but it took about 100 years before a real demand for magnesium developed. The uses of magnesium as a structural material were, however, very few. The bulk was used as an alloying element in aluminum alloys. Since 1993 there has been renewed interest in using magnesium based alloys in automobile, aerospace and other household and sport applications. The driving force is the weight saving. Magnesium is substantially less dense than aluminum. It is also relatively expensive to produce, not as easily worked as aluminum, relatively few developed alloys exist, no secondary recycling procedure has been developed and there are questions as to corrosion resistance, safety and reliability; all factors which prevent its wide acceptance. Unless the automobile industry embraces its use, magnesium would not become economically viable in other fields [2].

2.1.1 Physical Metallurgy and Properties

Magnesium and magnesium alloys have been employed in a wide variety of structural applications because of their favorable combination of tensile strength (160 to 365 MPa), elastic modulus (45 GPa) and low density (1.74 gm/cm^3). Magnesium alloys have high

strength-to-weight ratios and relatively good electrical conductivity and thermal conductivity. They have also high damping capacity, that is, the ability to absorb elastic vibrations.

Magnesium is a silvery white metal. It is the sixth most abundant metal on earth. Table 2-1 shows the physical properties of magnesium and other structural materials. Its density is less than one quarter that of iron and two-thirds that of aluminum. The melting point and specific heat of magnesium are almost the same as those of aluminum. The Young's modulus and shear modulus of magnesium are about two-thirds of those of aluminum. Another aspect is good damping behavior. Pure magnesium shows even higher damping properties than cast iron, although these properties are highly dependent on the prior heat treatment [1].

Table 2-1 Physical properties of metals [1].

	Mg	Al	Ti	Fe	Cu
Lattice Structure	HCP	FCC	HCP	BCC	FCC
Density (gm/cm^3)	1.74	2.70	4.51	7.87	8.98
Melting Point (^oC)	650	660	1668	1535	1083
Specific Heat ($cal/m.^oC$)	0.24	0.22	0.13	0.11	0.09
Young's Modulus (GPa)	45	76	114	190	136
Shear Modulus (GPa)	17	26	45	80	44
Thermal Conductivity (W/m.K)	167	238	16	73	394

Figure 2.1 shows the lattice structure and slip systems of magnesium. Magnesium with a structure has poor formability at room temperature because of its HCP structure. The directions for easy crystallographic slip in HCP single crystals are the three <11-20> or closed packed directions. At low temperatures, the three dominant sets of planes which contain this slip direction are (0001)<11-20> basal plane. The activation of pyramidal and prismatic slip systems in polycrystalline aggregates occurs primarily due to the high temperature and large stresses generated in grain-boundary regions because of the misorientation between neighboring grains. Thus, magnesium has high ductility at elevated temperatures, because of the activation of three prismatic slip systems of {10-10}<11-20> and the six pyramidal slip systems of {10-11}<11-20> [15]. Therefore, commercially available magnesium is deformed normally at elevated temperature. For example, plastic processes for magnesium, such as rolling, forging and extrusion, are usually performed at elevated temperatures.

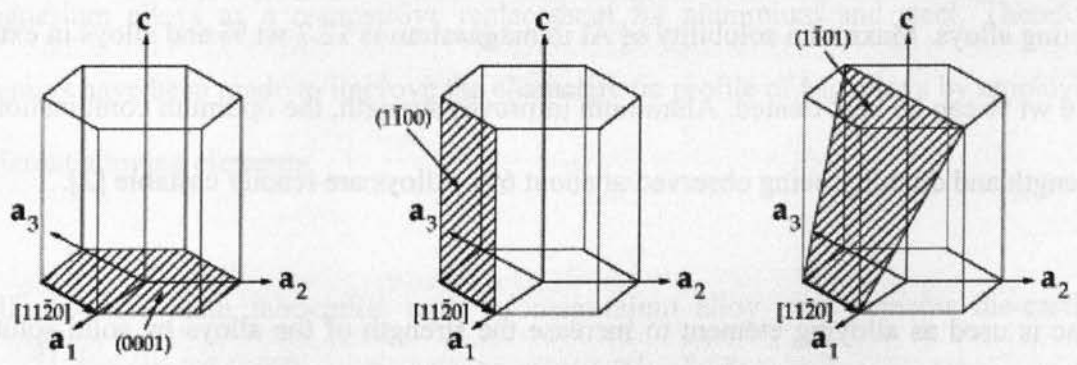

Figure 2.1: Basal, Prismatic and Pyramidal slip systems in pure magnesium [15].

2.1.2 Types of Magnesium Alloys

For the materials where only alloying can lead to sufficient strength for construction purposes, for practical design, two categories of magnesium alloys are usually used:

- This type of Mg alloys contains 2-10% of Al, with minor content of Zn and Mn. The productions cost for this type of alloys is relatively low and the mechanical properties of alloys fall down rapidly at higher temperature.
- This type contains wide variety of chemical elements, such as, Zn, Th, Ag, Si, with low content of Zr, which means close-grained structure and higher mechanical strength. These alloys have better properties at higher temperatures but their production cost is very high because of the expensive elements and the special production technology.

Aluminum is the most commonly used alloying element and forms the basis of the die casting alloys. Maximum solubility of Al in magnesium is 12.7 wt % and alloys in excess of 6 wt % can be heat treated. Aluminum improves strength, the optimum combination of strength and ductility being observed at about 6%. Alloys are readily castable [2].

Zinc is used as alloying element to increase the strength of the alloys by solid solution and precipitation. However, it reduces the ductility of the Mg alloys [16]

Manganese is usually not employed alone but with other elements, e.g., Al. In this case, compounds MnAl, $MnAl_6$ or $MnAl_4$ are formed. It reduces the solubility of iron and

produces relatively innocuous compounds. It increases the yield strength and improves salt water corrosion resistance of Mg-Al and Mg-Al-Zn alloys. Binary alloys are used in forgings or extruded bars. The maximum amount of manganese is 1.5-2 wt %. [2]

From other point of view, magnesium alloys are divided into casting alloys, wrought alloys, composites and powder materials. Most magnesium alloys show very good machinability and processability. Cast, moulded and forged parts are inert gas weld-able and machinable. Along with the excellent properties, there are some disadvantages to the application of these alloys. The cold working ability of the magnesium alloys is very poor and the corrosion resistance is very low. Again, when cast, magnesium has a high mold shrinkage, about 4% when solidifying and about 5% during cooling. This high degree of shrinkage leads to microporosity and low toughness that cannot be ignored [1].

The negative properties mentioned above kept engineers away from accepting magnesium alloys as a competitive replacement for aluminium and steel. Therefore, attempts have been made to improve the characteristic profile of Mg alloys by employing different alloying elements.

Still now, the main fabrication route of magnesium alloy parts remains die-casting because of its high productivity and dimensional accuracy. It is well known that wrought magnesium alloys have superior mechanical properties than cast alloys. Often these superior properties are attained through hot working such as rolling, forging and extrusion during which the grains are greatly refined.

2.2 Mechanical Properties

2.2.1 Tensile Properties

So far, some mechanical properties of different magnesium alloys were studied and experimented by researchers. Due to the HCP structure, Mg alloys show high anisotropy in mechanical properties, which is the main barrier to the wider application of wrought Mg alloys. The following sub-sections describe the tensile behavior of some wrought Mg alloys.

2.2.1.1 Tensile Strength and Ductility

Experimental results of the tensile tests from different investigations on Mg alloys show the dependence of tensile properties such as yield strength, tensile strength, elongation and strain hardening exponent on applied strain rate and temperature. However, in this study, only the effect of strain rate on the tensile behavior is considered. El-Magd and Abouridouane [17] conducted tensile tests on AZ80, AA7075 and Ti-6Al-4V at different temperature levels and observed a high tensile stress and low ductility in high strain rate tests at room temperature. Different strain rate tensile tests on AZ31, AZ61 by Yokoyama [18] and on AM30 by Jiang *et al.* [19] showed that yield strength increased; however, the strain hardening exponent decreased with increasing strain rate. Deformation of Mg alloys at low temperature is mainly dominated by twinning and grain boundary sliding as summarized by Roberts [20]. The relative contribution of twinning to the overall

deformation depends on the strain rate, temperature and microstructure (grain size and precipitates). High strain rate, low temperature and coarse grain promote mechanical twinning [21]. The strain hardening phenomenon mainly arises from the interactions among the dislocations that impede the motion of the dislocations,; particularly, the HCP structure of magnesium alloys facilitate twinning which acts as a barrier to the dislocation and cause the formation of dislocation pile-ups, which initiate the back stress and result in the strain hardening [22-24]. Twinning induced softening was also observed due to the annihilation and rearrangement of dislocations [19, 21]. Luo *et al.* [19] observed that wrought AM30 showed softening at high strain rates. Basically, when twinning induced softening overrides both the twinning induced hardening and dislocation hardening, the n value increases with decreasing strain rate.

2.2.1.2 Tensile Fracture Surfaces

The tensile fracture mode of wrought magnesium alloys is affected by strain rate and temperature. The HCP structure of Mg alloys facilitates its deformation by twinning at room temperature. During tensile deformation, formation of voids or micro-cracks near the twinned region causes the alloy to fracture. The tensile fracture surface of wrought AZ31 alloy investigated by Marya *et al.* [25] showed that, at a strain rate of $1\times10^{-3}s^{-1}$, the alloy exhibited a mixed mode fracture, with the presence of a brittle type of both inter-granular and trans-granular separation and ductile fracture in the form of micro-voids. Mg-Nd alloy, investigated by Yunqi *et al.* [26], exhibit tensile dimple fracture at room temperature. El-Magd and Abouridouane [17] observed that, at a strain rate $1\times10^{-3}s^{-1}$, the

tensile fracture of AZ80 wrought alloy was due to the initiation and growth of micro-cracks. Similarly, nucleation of voids was observed in the twinned region interlinked to form large cavities, which finally result in tensile fracture of AM30 [19].

2.2.2 Fatigue and Its Characteristics

In materials science, fatigue is progressive, localized, and permanent structural damage that occurs when a material is subjected to cyclic or fluctuating strains at nominal stresses that have maximum values less than (often much less than) the static yield strength of the material. The consequence is usually catastrophic failure.

Fatigue can occur in many different forms. Fluctuations in externally applied stresses or strains result in mechanical fatigue. Cyclic loads acting in association with high temperatures cause creep-fatigue. When the temperature of the cyclically loaded component also fluctuates, thermo-mechanical fatigue is induced. Recurring loads imposed in the presence of a chemically aggressive embrittling environment give rise to corrosion fatigue. Generally, fatigue failure takes place under the influence of cyclic loads, whose peaks are considerably smaller than the safe loads estimated on the basis of static fracture analyses [27].

A fatigue failure is particularly harmful because it occurs without any obvious warning. Fatigue results in a brittle appearing fracture, with no gross deformation at the fracture.

On a macroscopic scale, the fracture surface is usually normal to the direction of the principal stress [23].

Three basic factors are necessary to cause fatigue failure [23]. These are,

- A maximum tensile stress of sufficiently high value,
- A large enough variation or fluctuation in the applied stress,
- A sufficiently large number of applied cycles.

In addition, there are a host of other variables, such as stress concentration, corrosion, temperature, overload, metallurgical structure, residual stresses, and combined stresses, which tend to alter the conditions for failure.

2.2.2.1 Low Cycle Fatigue

Low cycle fatigue conditions frequently are created where the repeated stresses are of thermal origin [28]. Since thermal-stresses arise from the thermal expansion of the material, it is easy to see that in this case fatigue results from cyclic strain rather than from cyclic stress. The low cycle fatigue occurs at the high stress level and low numbers of cycles. Usually, nuclear pressure vessels, steam turbines, and most other type pressure vessels must be considered for low cycle fatigue [23]. The usual way of presenting low cycle fatigue test is to plot the plastic strain range $\Delta\varepsilon_p$ against N. Figure 2.2 shows the straight line obtained when plotted on log-log co-ordinates.

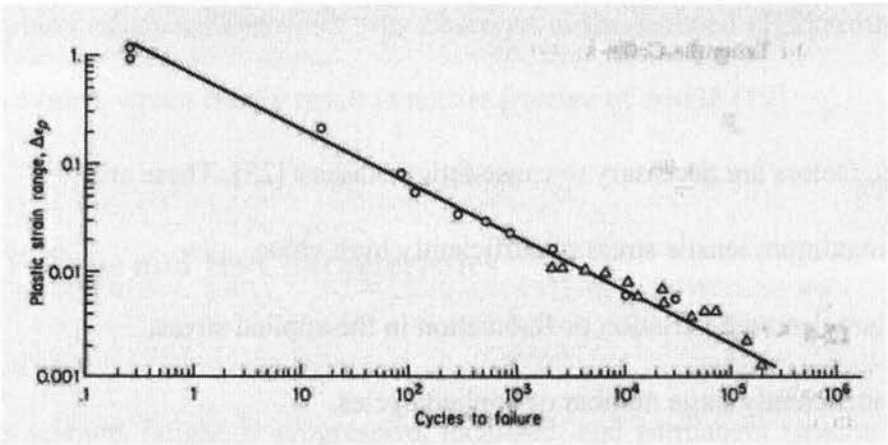

Figure 2.2: Low cycle fatigue curves [23].

This behavior could be best described by the following equation known as the Coffin-Manson relation:

$$\frac{\Delta\varepsilon_p}{2} = \varepsilon_f' \left(2N_f\right)^c \quad \text{.....(1)}$$

where, $\frac{\Delta\varepsilon_p}{2}$ = Plastic strain amplitude,

ε_f' = Fatigue ductility coefficient defined by the slope of the curve plotted by using equation 1. ε_f' is approximately equal to the true fracture strain ε_f for many metallic materials.

$2N_f$ = Number of strain reversals to failure (one cycle equals two reversals).

c = Fatigue ductility exponent, which varies between -0.5 to -0.7 for many metallic materials.

2.2.2.2 Cyclic Stress-Strain Curve

Cyclic strain control fatigue is different from the cyclic stress controlled fatigue. This occurs when the strain amplitude is held constant during cycling. Strain controlled cyclic loading is usually found in thermal cycling, where a component expands and contracts in response to fluctuations in the operating temperature, or in reversed bending between fixed displacements [23].

Figure 2.3 shows a schematic stress-strain loop under controlled constant strain cycling. O-A-B is the initial loading stress-strain curve. On unloading, yielding begins in compression at a lower stress C due to the Bauschinger effect. In reloading in tension, a hysteresis loop develops.

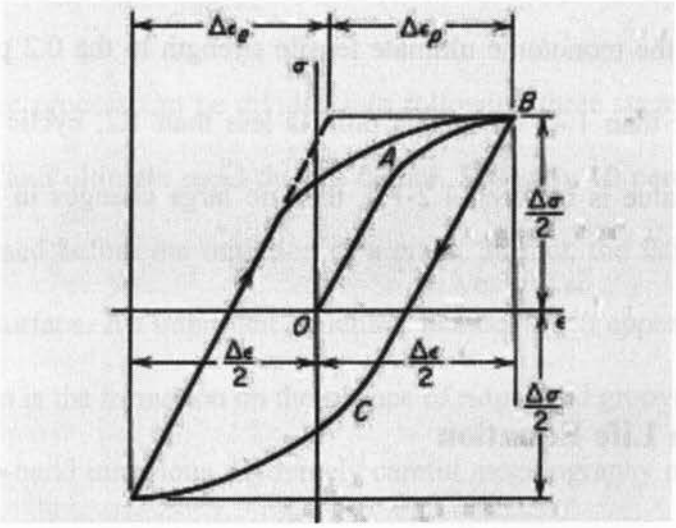

Figure 2.3: Stress-strain loop for constant strain cycling [23].

The dimensions of the hysteresis loop are described by its width $\Delta\varepsilon$, the total strain range, and its height $\Delta\sigma$, the stress range. The total strain range $\Delta\varepsilon$ consists of the

elastic strain component $\Delta\varepsilon_e = \frac{\Delta\sigma}{E}$ plus the plastic strain component $\Delta\varepsilon_p$. The width of the hysteresis loop will depend on the level of cyclic strain. The cyclic stress- strain curve may be described by the following equation:

$$\frac{\Delta\sigma}{2} = K'\left(\frac{\Delta\varepsilon_p}{2}\right)^{n'} \quad \text{.....(2)}$$

n' = Cyclic strain hardening exponent

K' = Cyclic strength coefficient

For metals n' varies between 0.10 and 0.20. In general, metals with high monotonic strain-hardening exponents (n> 0.15) undergo cyclic hardening; those with a low strain-hardening exponent (n < 0.15) undergo cyclic softening. Cyclic hardening is expected when the ratio of the monotonic ultimate tensile strength to the 0.2 percent offset yield strength is greater than 1.4. When this ratio is less than 1.2, cyclic softening is to be expected. If the value is between 1.2-1.4, then no large changes in hardness are to be expected [23].

2.2.2.3 Strain Life Equation

For the high cycle regime, where the nominal strains are elastic, Basquin's equation can be expressed as:

$$\frac{\Delta\varepsilon_e}{2} = \frac{\sigma_f'}{E}(2N_f)^b \quad \text{.....(3)}$$

An equation valid for the entire range of fatigue lives can then be obtained by using the following relationships:

$$\frac{\Delta\varepsilon}{2} = \frac{\Delta\varepsilon_e}{2} + \frac{\Delta\varepsilon_p}{2} \quad \text{.....(4)}$$

Replacing $\frac{\Delta\varepsilon_p}{2}$ with equation (1) and $\frac{\Delta\varepsilon_e}{2}$ with equation (3) we can get:

$$\frac{\Delta\varepsilon}{2} = \frac{\sigma_f'}{E}(2N_f)^b + \varepsilon_f'(2N_f)^c \quad \text{.....(5)}$$

This equation is valid for the entire fatigue life.

2.2.2.4 Characteristic Feature of Fatigue Fracture Surface

The fatigue fracture process can be divided into following three stages: crack initiation, crack propagation and ultimate rapid ductile failure. Basically 10 percent of the fatigue life of metals elapsed before the initiation of a crack. In fact, the fatigue crack usually initiates at a free surface. An important structural feature which appears to be unique to fatigue deformation is the formation on the surface of ridges and grooves called slip-band extrusions and slip-band intrusions. Extremely careful metallography on tapered sections through the surface of the specimen has shown that fatigue cracks initiate at intrusions and extrusions.

Fatigue crack propagation usually occurs in two stages. During stage I, the crack propagates along the persistent slip bands. Stage I crack propagation is very slow compared to the stage II propagation, where the crack is basically normal to the loading direction. During stage I, the crack propagation rate may be on the order of angstroms per cycle. But, for stage II, the rate could be microns per cycle [23].

2.2.2.5 Crack Initiation and Propagation

In magnesium alloys, fatigue crack also initiates at slip bands. These slip bands form due to plastic deformation. The deformation mode of HCP structures is more complex than the BCC or FCC structures. Figure 2.4 shows the fatigue slip bands in AZ91 which act as crack nucleation sites.

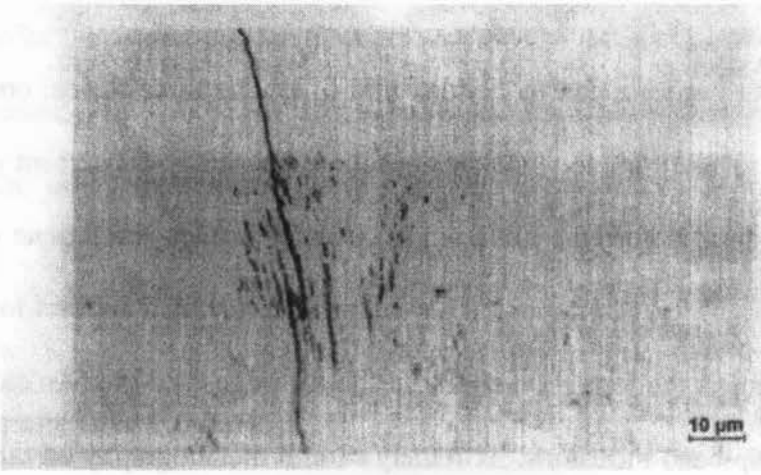

Figure 2.4: Fatigue slip bands, acting as crack initiation sites in AZ31 [29].

Since magnesium has a hexagonal closed packed (HCP) structure, at room temperature, the dislocation movement occurs along the basal slip (0001) planes in the <1120>

direction. But at elevated temperatures, the other slip systems are activated, which include, pyramidal slip planes {1011} <1120> and prismatic planes {1010} <1120>. In HCP structures, twinning is also a mode of deformation in {1012}, {1011}, {1122}, and {1121} planes. In magnesium, {1012} is the most common twinning plane. In defect free material, fatigue slip bands are the sites for crack initiation. Cast magnesium alloys contain casting defects, even though they have good castability. The formation of casting defects often depends on the solidification process. The large solidification range of most magnesium alloys leads to the formation of microshrinkage (Figure 2.5), which is favored by the dendritic structure.

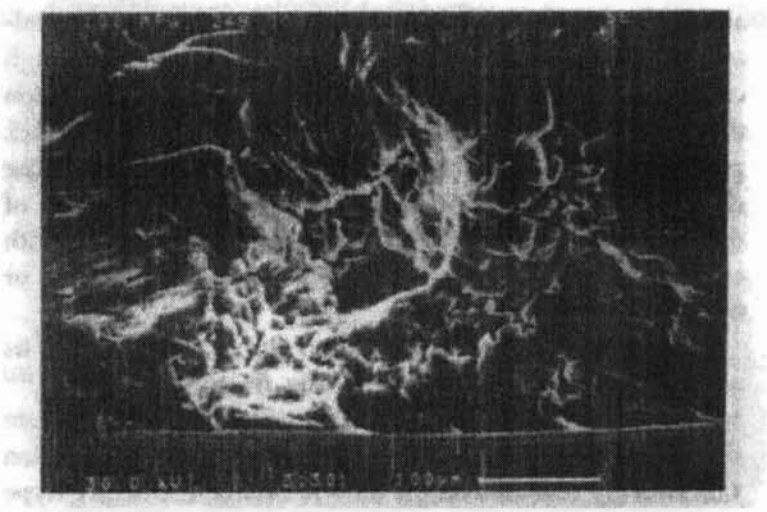

Figure 2.5: Microporosity at the fatigue crack initiation site in AZ91 [29].

The reason for the formation of casting defects may lie in the processing route of the high pressure die-casting. Due to the high casting speed, the melt flow is non-laminar and air can be trapped which causes porosity when it solidifies. As a consequence, high stress concentrations at casting defects initiate fatigue cracks instead of slip bands. Casting

defects like pores and microshrinkage reduce the crack initiation stage. As a result, the lifetime of the component also reduces.

After the crack initiation, the propagation of the crack occurs at an angle of 45° to the applied load and this propagation is also affected by the microstructure of the alloy, such as grain boundaries and the orientation of basal slip planes to the load direction. Though the crack initially propagates at an angle of 45° to the applied load, after a certain limit, it changes its direction and the crack grows perpendicular to the loading direction [29]. Figure 2.6 shows the growth of a crack in AZ91. Though the fatigue crack initiates at the slip band, 45° to the cyclic loading, it propagates perpendicular to the cyclic loading.

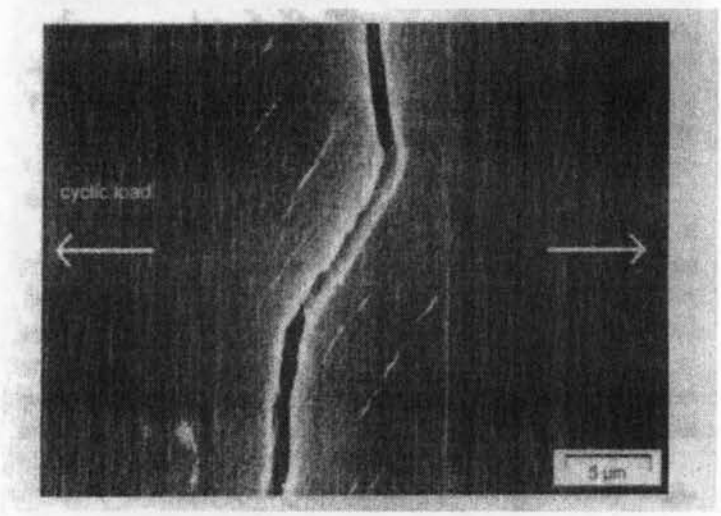

Figure 2.6: Fatigue crack with initial slip bands in AZ91 [29].

Fatigue crack propagation can be transgranular or intergranular. In cast magnesium alloys such as AZ91, the brittle intermetallic compound $Mg_{17}Al_{12}$ at the grain boundary helps to increase the cracking. Besides, high crack tip driving forces tend to promote crack propagation through the $Mg_{17}Al_{12}$ phase, while lower loads assist crack propagation

through the primary alpha-Mg grains [29]. The crack growth is also assisted by the connection of different microcracks of casting defects (in cast alloys), which developed between pores or microshrinkage.

Magnesium alloys show relatively low fracture toughness. Concerning the crack propagation rate, which promotes a higher crack propagation rate in magnesium alloys than in other light metals. The crack propagation rate strongly depends on the individual microstructure and the microstructural constituents. Ogarevic and Stephens [30] showed that Mg-Nd and Mg-Zn based alloys have a low crack propagation rate because of the precipitates formed. But in AZ91 (age hardened (T6) and as-cast (F)), the precipitates of $Mg_{17}Al_{12}$ increase the crack propagation rate [31].

CHAPTER 3

EXPERIMENTAL PROCEDURE

3.1 Materials and Composition

Two wrought alloys of similar extruded shape, namely, AZ31 and AM30, are selected in this study. Both materials are developed and provided by General Motors Research and Development Center. Figure 3.1 shows part of the extruded material received. Microstructure and test samples are taken from section A which has a thickness of 7 mm.

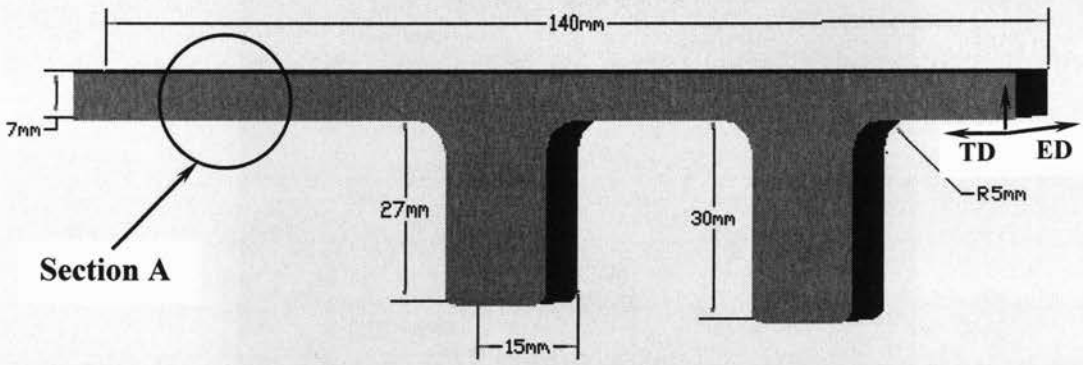

Figure 3.1: AZ31 and AM30 extruded test materials selected in the present investigation.

Figure 3.2 shows areas along the thickness of the plate used for microstructural investigation. AZ31 is extruded in a temperature range of 360-382°C at an extrusion exit speed of 50.8 mm/s. The applied extrusion ratio was about 6, and after extrusion the alloy was air quenched, while AM30 was extruded at an extrusion exit speed of 76.2 mm/s, i.e., 1.5 times faster than that of AZ31, with an extrusion ratio of about 6. The extrusion

temperature range was 360°-382°C and the alloy was air quenched after the extrusion process. The chemical compositions of AZ31 and AM30 are listed in Table 3-1. In AM30 the amount of Zn has been eliminated to increase the ductility of the alloy.

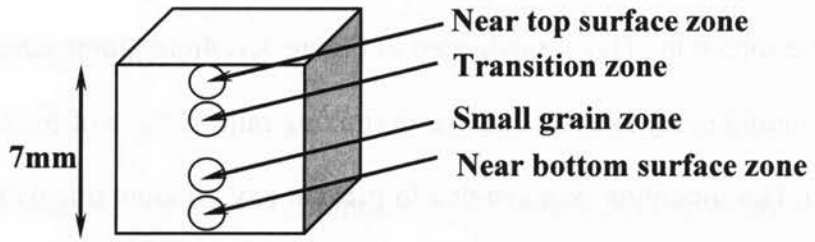

Figure 3.2: Schematic illustration of section A.

Table 3-1 Chemical composition of AZ31 and AM30, selected in the present study.

Alloy	Al	Zn	Mn	Fe	Ni	Cu	Mg
AZ31	3.1	1.05	0.54	0.0035	0.0007	0.0008	Balance
AM30	3.4	0.16	0.33	0.0026	0.0006	0.0008	Balance

3.2 Sample Preparation and Testing

The experimental tests are conducted and metallographic sample are prepared in the Mechanical Engineering Department laboratories at Ryerson University.

3.2.1 Metallography

All metallographic samples for microstructural characterization were taken from the cross section perpendicular to the extrusion direction. The extrusion direction (ED) and the transverse direction (TD) are indicated in Figure 3.1. 4mm×4mm samples were taken for cold mounting using Lecoset 7007 resin (mixing ratio: 2 parts of resin added to 1 part of catalyst). Hot mounting was avoided to prevent any possible microstructure change due to the effect of temperature during sample preparation.

The mounted samples were manually ground with SiC papers up to a grit of #1200 with water as the lubricant and then polished with 6μm, 3μm and 1μm diamond paste followed by finer Master-Prep solution. The polishing lubricant for the diamond paste was a mixture of rust inhibiting solution and distilled water (10% solution by volume). Due to the reactive nature of magnesium in the presence of water, ethanol was used as a cleaning agent during the polishing stages.

The polished samples were etched with Acetic-Picral to reveal the macroscopic structure (grain boundaries) of the alloys. The Acetic-Picral acid was a solution of 10 ml acetic acid, 4.2 g picric acid, 10 ml distilled water, and 70 ml ethanol (95%).

3.2.2 Quantitative Image Analysis

Microscopic images were taken using a light microscope and image analyses were subsequently performed using Clemex software to obtain the grain size, aspect ratio and fractal dimension of the grains.

The Clemex image analysis system was comprised of a Clemex CMT software adaptable to ASTM standards, a Nikon optical microscope (10× eye piece, five different object lenses with magnifications of 5×, 10×, 20×, 40×, and 100×), a high-resolution digital camera, and a high performance computer to carry out the detailed analysis.

The microstructural characteristics of the alloy were observed in parallel to the extrusion direction (Figure 3.1).

3.2.3 Micro-hardness Tests

A computerized Buehler microhardness testing machine was used for the micro-indentation hardness tests where a load of 50 g and duration of 15 s were used. The test results were recorded in the computer using a Hyper Terminal. Micro-indentation tests were performed along a path of 7 mm thickness of the plate for the longitudinal direction, with an interval of 0.05 mm between two successive indentations near the bottom surface zone, 0.1 mm indentation interval at the small grain zone and transition zone and 0.25 mm indentation interval near the top surface zone.

3.2.4 Tensile Tests

The samples for tensile tests were prepared according to the ASTM E8M [32] standard for sub-sized sheet type material (i.e., 25 mm gage length and 6 mm gauge width). Specimen dimensions are shown in Figure 3.3. All samples for the tensile tests were taken parallel to the extrusion direction. The tests were carried out using a computerized United testing machine at 4 different strain rates: $1\times10^{-2}s^{-1}$, $1\times10^{-3}s^{-1}$, $1\times10^{-4}s^{-1}$ and $1\times10^{-5}s^{-1}$. All the tests are conducted at room temperature. After tensile tests, fracture surfaces were examined using a scanning electron microscope (SEM) equipped with an energy dispersive X-ray spectroscopy (EDS) system.

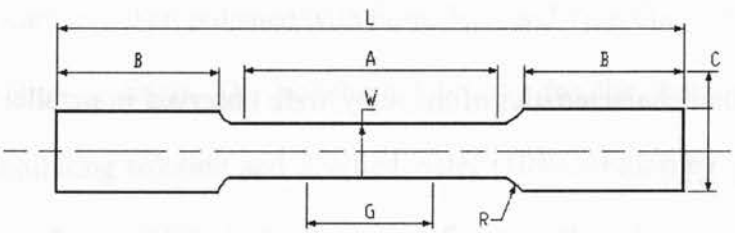

	Dimensions in mm
G – Gauge length	25
W – Width	6
R – Radius	6.35
L – Overall length	140
A – Length of the reduced section	32
B – Length of the Grip Section	50
C – Width of the grip section	9.52

Figure 3.3: Geometry and dimensions of the sub-sized tensile/fatigue test specimen according to ASTM E8M [32].

3.2.5 Fatigue Tests

Fatigue tests were performed using a fully computerized servo-hydraulic INSTRON 8801 fatigue testing system. The tests were carried out in a strain control mode according to ASTM E606 [33] standards. Samples were subjected to fatigue cycling parallel to the extrusion direction. The fatigue tests were carried out at zero mean strain (R_ε=-1, completely reversed strain cycle), a constant strain rate of 1×10^{-2} s^{-1} and room temperature of 25°C. Triangular waveform loading was applied during the tests. The strain controlled tests at lower strain amplitude levels were continued up to 10000 cycles, then the tests were changed to load control tests with a frequency of 50 Hz. Low cycle fatigue tests were conducted at total strain amplitudes of 0.1%, 0.2%, 0.3%, 0.4%, 0.5% and 0.6%, and at least two tests were performed at each level of the strain amplitudes.

To study the effects of mean strain and mean stress on the LCF behavior of the AZ31 alloy, five different strain ratios, R_s= 0.5, 0, -0.5, -1 and -2, were used at a given total strain amplitude of 0.4% and a constant strain rate of 1×10^{-2} s^{-1}. Different strain rates of 1×10^{-3}, 1×10^{-2} and 8×10^{-2} s^{-1} were further applied to observe the effect of stain rate on the fatigue life of the alloy. The tests were normally started with tensile loading. To examine the effect of reverse loading direction on the fatigue life, a test was also started with compressive loading while keeping all the other parameters unchanged (i.e., R_s= -1, strain rate of 1×10^{-2} s^{-1} and strain amplitude of 0.4%). After fatigue tests, the scanning electron microscope (SEM) equipped with an energy dispersive X-ray spectroscopy (EDS) system

was used to examine the fatigue crack initiation sites and identify the mechanism of fatigue crack propagation under the above applied conditions.

CHAPTER 4

MECHANICAL PROPERTIES OF AZ31 EXTRUDED MAGNESIUM ALLOY

4.1 Microstructure

Figure 4.1(a)-(d) shows typical microstructures of the extruded AZ31 across the thickness at the longitudinal face. It is seen that the microstructure is non-uniform along the thickness of the specimen.

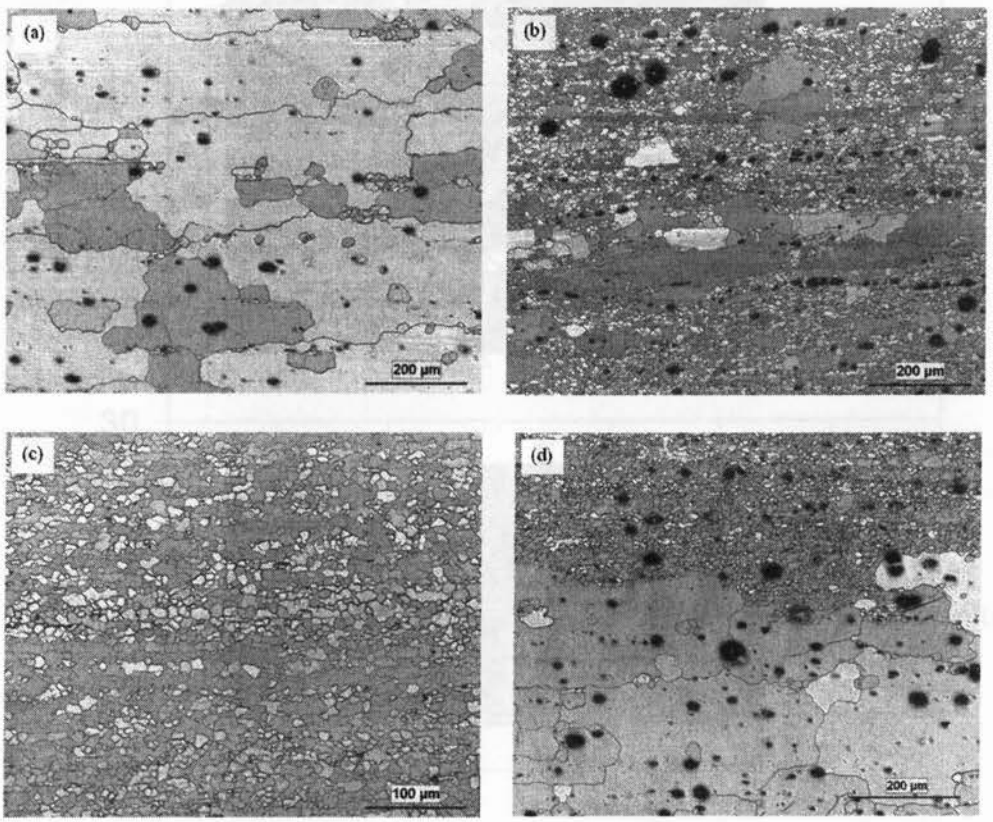

Figure 4.1: Optical microscope images of AZ31 alloy in the, (a) zone near the top surface, (b) transition zone, (c) small grain zone, and (d) zone near the bottom surface.

Larger grains were observed at both top and bottom surfaces of the specimen, where the zones near the top surface and near the bottom surface are indicated in Figure 3.2. with an average grain size of about 60 μm. The center of the specimen contained very small grains with an average size of about 6 μm, as shown in Figure 4.1(c). The transition area from the large grains to small grains is shown in Figure 4.1(b). Figure 4.1(d) shows a sudden change of the grain sizes from small to large grains. EDS analysis revealed that the black dots on the images were Mn- and Al-containing particles. The following Figure 4.2 shows the EDS analysis of particles. It was observed that the particles contain 67% Mn, 23% Al and a very small amount of Mg, mainly known as Mn-Al particles.

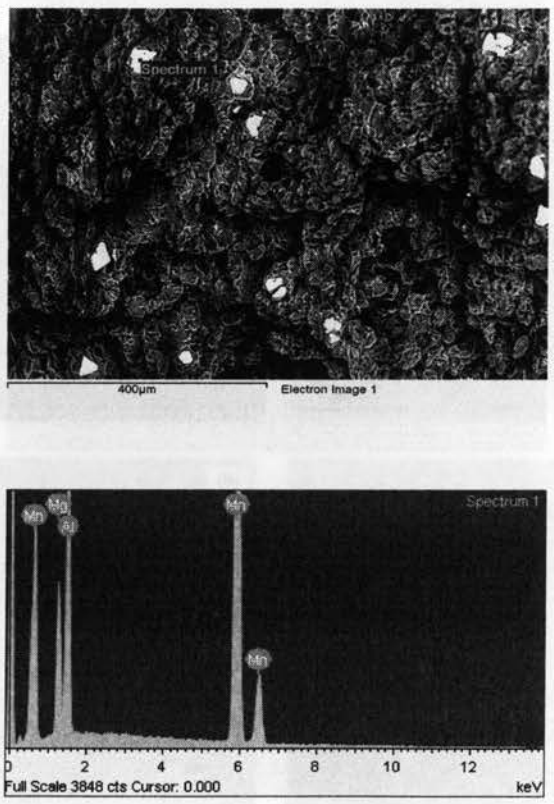

Figure 4.2: EDS analysis of particles of the AZ31 alloy.

4.2 Micro-hardness

Figure 4.3 shows a typical hardness profile along the 7 mm thickness, viewed in the longitudinal direction. Four zones containing different grain sizes are identified using dashed lines. The hardness profile shows that near the bottom surface and near the top surface the hardness is low due to the presence of large grains.

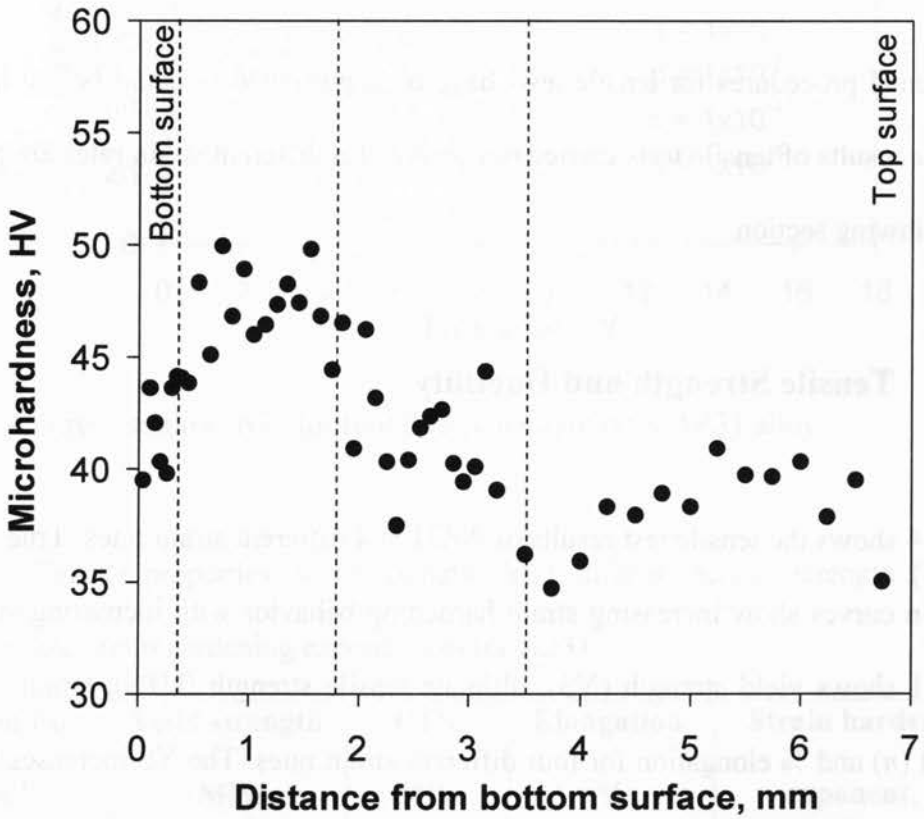

Figure 4.3: Micro-hardness profile along the thickness of plate, viewed in the longitudinal direction for AZ31 alloy.

Near the top surface zone, the large grains have an average hardness value of about 40 HV and near the bottom surface zone the average hardness value of grains is about 41 HV. However, about 0.5 to 1.8 mm from the bottom surface, the small grains lead to the highest average hardness value of about 48 HV.

4.3 Tensile Properties of AZ31

Experimental procedures for tensile tests have been presented in detail before in section 3.2.4. The results of tensile tests carried out on AZ31at different strain rates are presented in the following section.

4.3.1 Tensile Strength and Ductility

Figure 4.4 shows the tensile test results of AZ31 at 4 different strain rates. True stress vs. true strain curves show increasing strain hardening behavior with increasing strain rate. Table 4-1 shows yield strength (YS), ultimate tensile strength (UTS), strain hardening exponent (n) and % elongation for four different strain rates. The YS increases from 182 MPa to 199 MPa, ultimate tensile strength increases from 228 MPa to 264 MPa and the strain hardening exponent increases from about 0.11 to 0.14 with increasing strain rate; however, the ductility of the alloy decreases 19.6 to 15.2 with increasing strain rates. Figure 4.5 (a), (b), (c) and (d) shows the change of tensile properties such as YS, UTS, n and % elongation with strain rates, respectively.

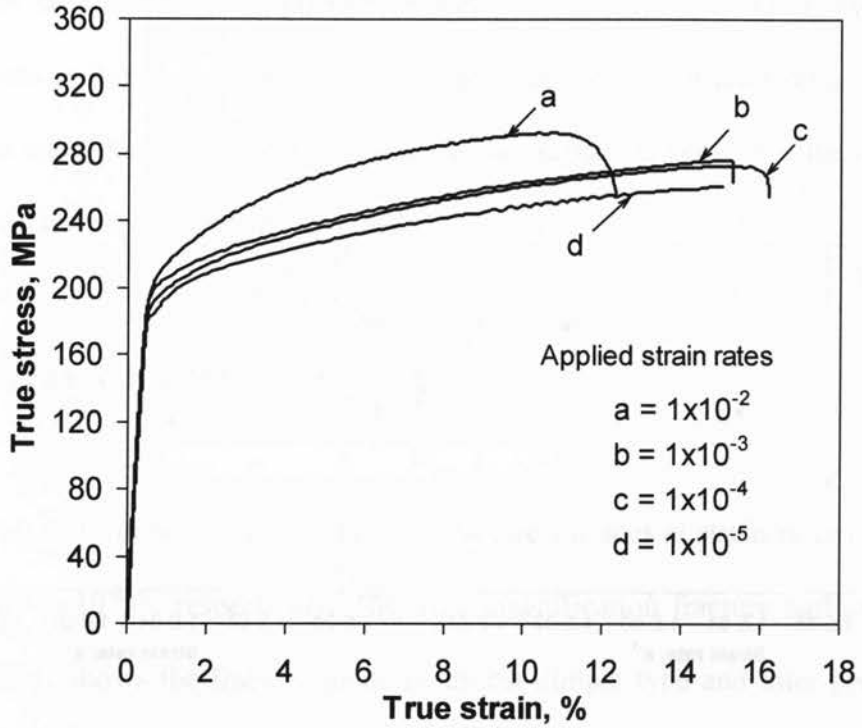

Figure 4.4: Stress-strain curves for four different strain rates-AZ31 alloy.

Table 4-1 Tensile properties: yield strength (YS), ultimate tensile strength (UTS), % elongation and strain hardening exponent (n) for AZ31.

Strain rate, s^{-1}	**Yield strength, MPa**	**UTS, MPa**	**Elongation, %**	**Strain hardening exponent, *n***
$1x10^{-2}$	199	264	15.2	0.137
$1x10^{-3}$	196	239	17.7	0.130
$1x10^{-4}$	190	237	19.1	0.133
$1x10^{-5}$	182	228	19.6	0.107

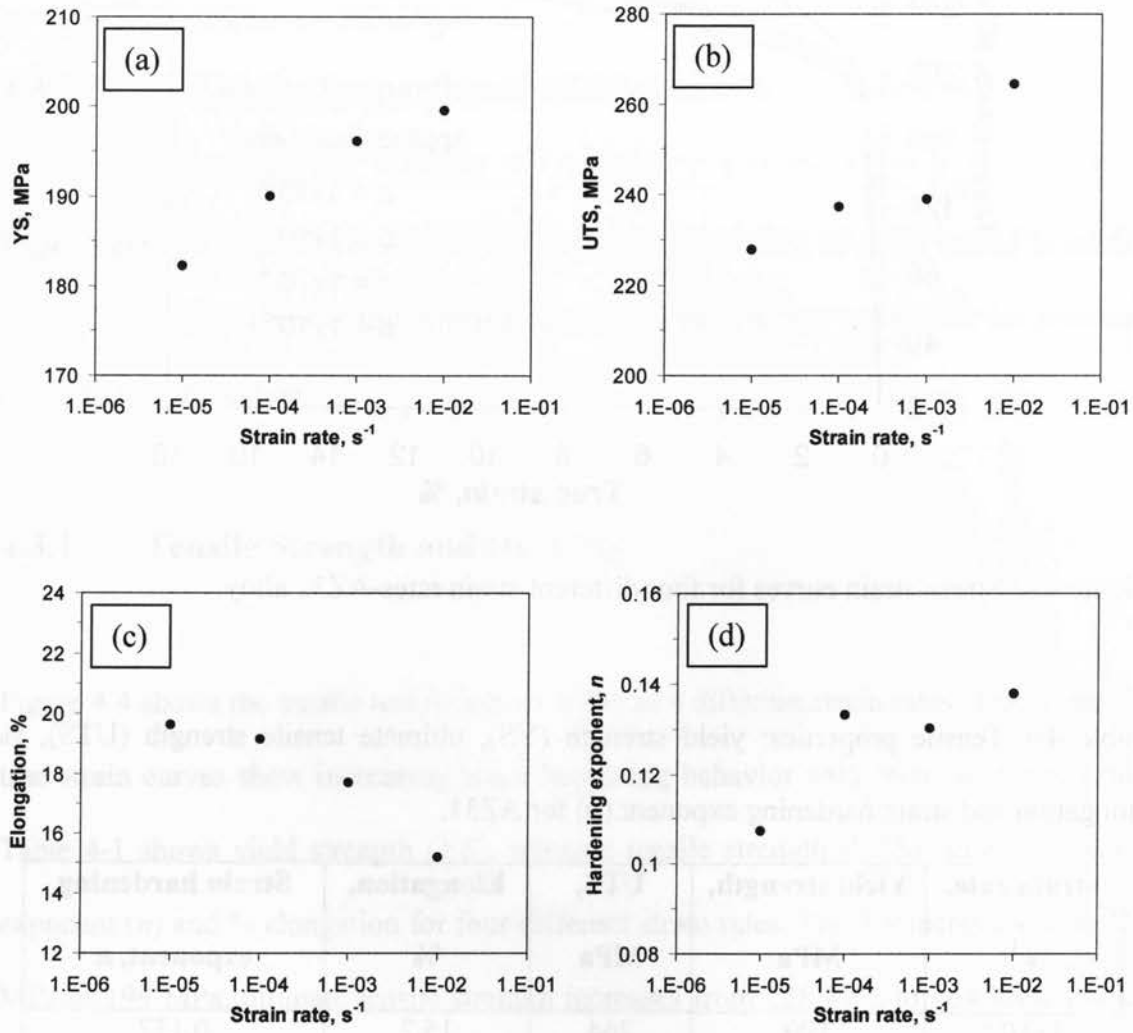

Figure 4.5: Tensile properties as a function of strain rate, (a) YS, (b) UTS, (c) % elongation and (d) strain hardening exponent, for AZ31.

The reason for such an increase in tensile properties at high strain rates could be explained by the formation of higher amount of twins at high strain rates. Twinning can act as barriers to the dislocation movement and cause the strain hardening. Dislocation pile-ups can cause back stresses which impede the further movement of the dislocations and can result in the strain hardening [22-24].

4.3.2 Tensile Fracture Surfaces

Figure 4.6 (a), (b), (c) show SEM images of fracture surfaces at strain rates of $1\times10^{-5}s^{-1}$, $1\times10^{-3}s^{-1}$ and $1\times10^{-2}s^{-1}$, respectively. The high magnification fracture surface image in Figure 4.6(a)-II shows the fracture mode is almost dimple type and inter-granular. The presence of small micro-voids containing almost rectangular shape particles are visible and the particles are Mn-Al particles in section 4.1.

Figure 4.6 (b) shows that, at a strain rate of 100 times higher, the alloy shows a mixed fracture mode with both brittle type cleavage facets and dimple like ductile surfaces. Intergranular and trans-granular fracture mode is visible in the high magnification image (Figure 4.6 (b)-II). The microvoids are bigger than in the previous sample, suggesting that the large microvoids are in fact grain pullouts, a form of ductile fracture. At the higher strain rate, 10 times higher (Figure 4.6 (c)), the alloy shows more brittle type fracture with cleavage-like features. Micovoids formation at the higher strain rate is larger than at lower strain rates. Plate-like features in Figure 4.6 (c)-II strongly suggest fracture either along twin boundaries or shear bands.

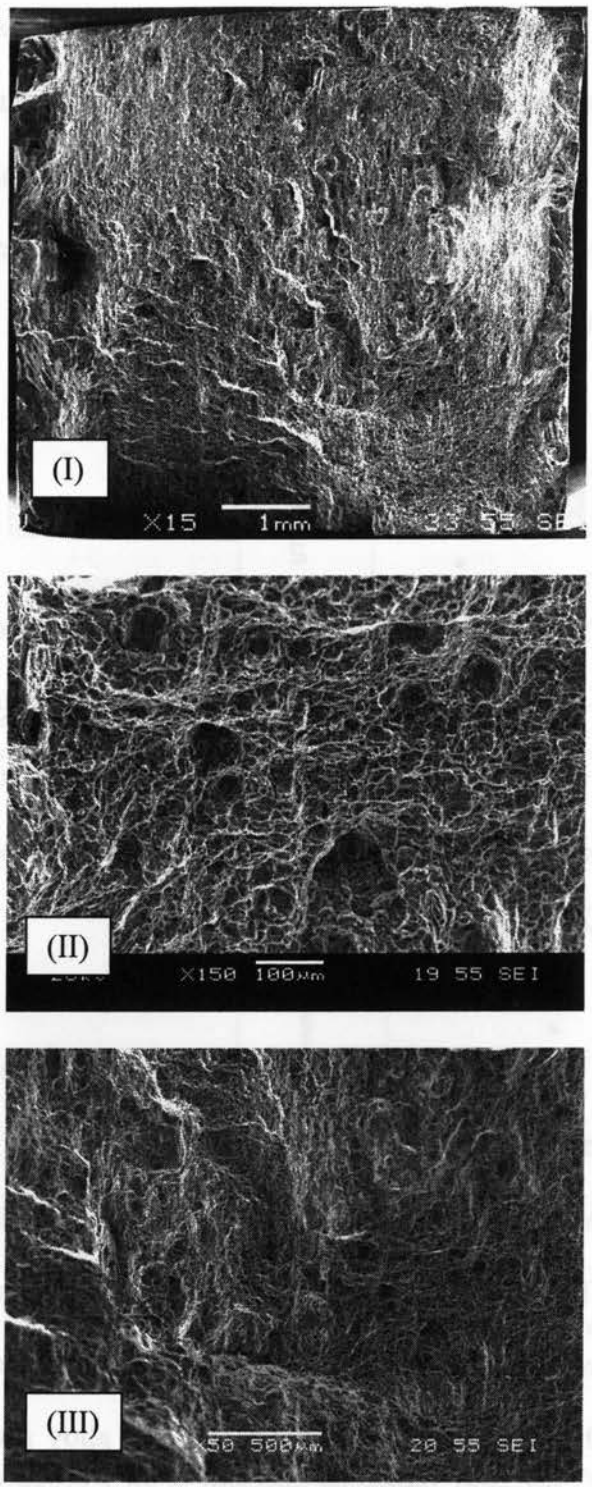

Figure 4.6 (a): SEM micrographs of fracture surfaces of AZ31 alloy after tensile testing at a strain rate of $1\times10^{-5}s^{-1}$, (I) entire fracture surface (II) magnified view of dimples and particles and (III) small pull-outs near the particles.

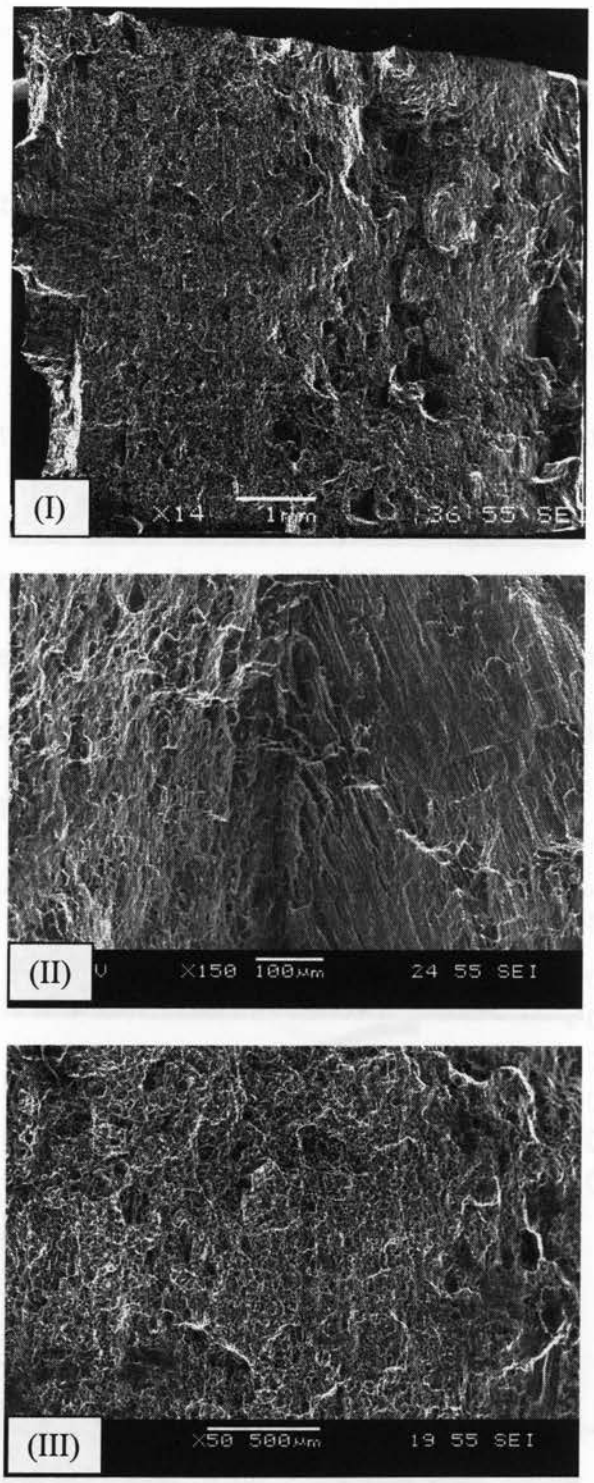

Figure 4.6 (b): SEM micrographs of fracture surfaces of AZ31 alloy after tensile testing at a strain rate of $1\times10^{-3}s^{-1}$, (I) entire fracture surface (II) magnified view of shear surfaces (III) small pull-outs near the particles.

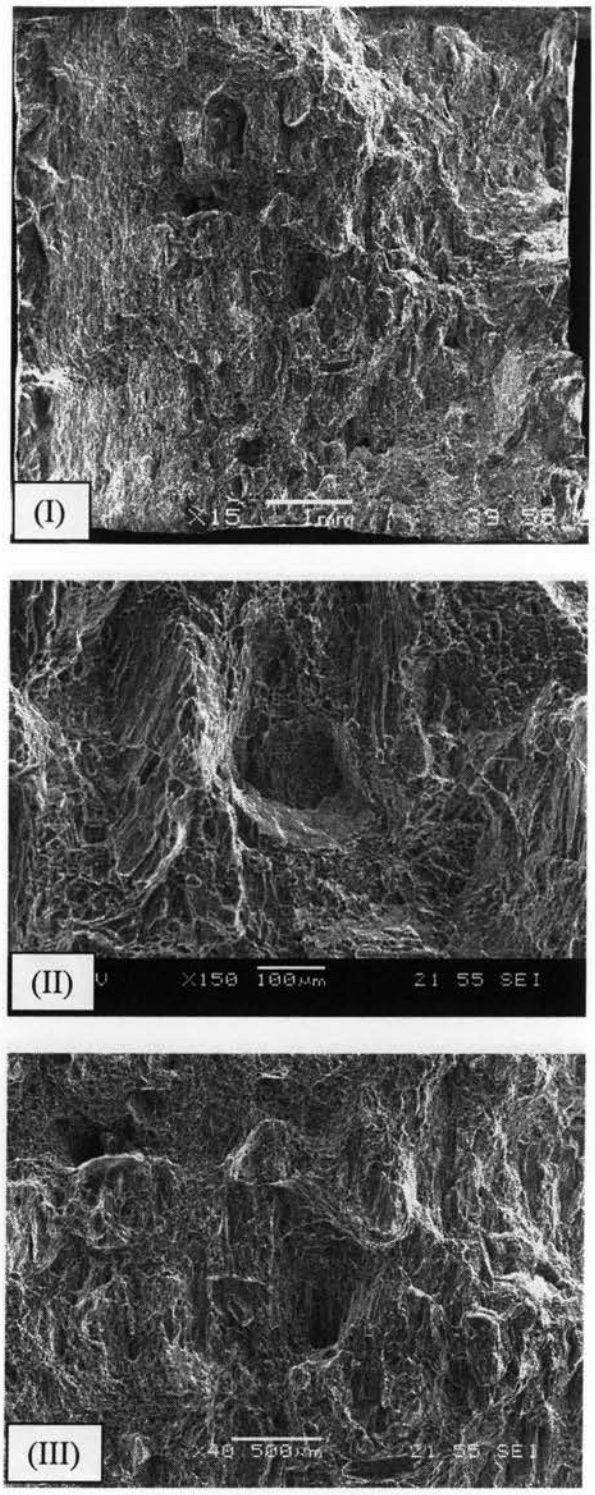

Figure 4.6 (c): SEM micrographs of fracture surfaces of AZ31 alloy after tensile testing at a strain rate of $1\times10^{-2}s^{-1}$, (I) entire fracture surface (II) magnified views mixed type fracture surface, and (III) large pull-outs and void formation during tensile testing.

4.4 Low Cycle Fatigue Properties of AZ31

4.4.1 Cyclic Stress Responses

Figure 4.7 shows the evolution of stress amplitude with respect to the number of cycles at different strain amplitudes on a semi log scale. At high strain amplitudes (0.5%, 0.6%), during the early cycles (up to 10 cycles), the alloy showed very little cyclic softening which was followed by cyclic hardening until failure. At strain amplitudes of 0.3% and 0.4%, the cyclic hardening started a little later and the cyclic hardening effect was not so strong as that at higher strain amplitudes. The stress amplitudes remained almost constant at the lower strain amplitudes (0.1%, 0.2%).

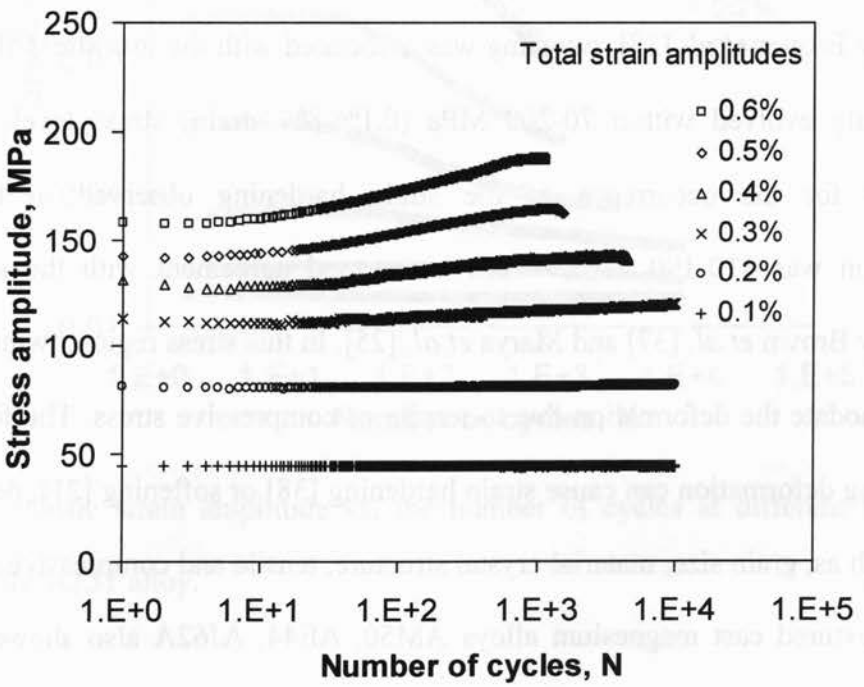

Figure 4.7: Stress amplitude vs. the number of cycles at different total strain amplitudes for AZ31.

Noster and Scholtes [5] mentioned in their work that the strain hardening effect was very small at room temperature; rather, they reported basically the temperature effect on the stress response, while the results presented in this paper showed that, at room temperature, the material could undergo cyclic strain hardening at high strain amplitudes.

Strain hardening is a phenomenon that arises from the interactions among the dislocations that impede the motion of the dislocations. Twinning and particles can act as barriers to the dislocation movement and cause the strain hardening. Dislocation pile-ups can cause back stresses which impede the further movement of the dislocations and can result in the strain hardening [23, 34].

Twinning plays an important role in plastic deformation of magnesium alloys [35-37]. As reported by Brown *et al.* [37], twinning was associated with the low stress flow regime, and typically evolved within 70-200 MPa (0.1%-8% strain) stress level. The stress amplitudes for the occurrence of the strain hardening observed in the present investigation was 110-190 MPa, which is in good agreement with the stress range reported by Brown *et al.* [37] and Marya *et al.* [25]. In this stress region, twinning is seen to accommodate the deformation due to tensile or compressive stress. The formation of twins during deformation can cause strain hardening [38] or softening [21], depending on factors such as, grain size, material crystal structure, tensile and compressive asymmetry. Random textured cast magnesium alloys AM50, AE44, AJ62A also showed twinning induced hardening behavior in fine grained structure, though coarse grained AM50 showed twinning induced softening [21].

4.4.2 Cyclic Strain Resistance

In the low cycle fatigue tests, the plastic strain amplitude is a physical quantity that initiates several damaging processes and influences the internal microstructure which eventually affects the strain resistance and finally the fatigue life. The variation of the plastic strain amplitude $\left(\frac{\Delta\varepsilon_p}{2}\right)$ during cyclic deformation is shown in Figure 4.8 for different total strain amplitudes.

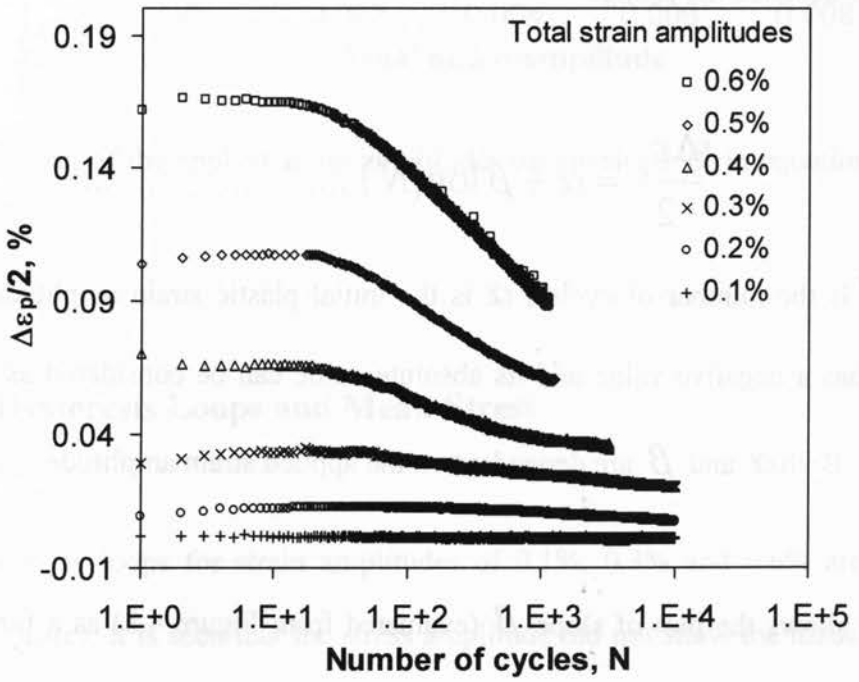

Figure 4.8: Plastic strain amplitude vs. the number of cycles at different total strain amplitudes for AZ31 alloy.

As the total strain amplitude increased, the value of the plastic strain amplitude also increased and the fatigue life of the material decreased. At lower total strain amplitudes

(0.1%, 0.2%), the plastic strain amplitude remained nearly constant over the entire fatigue life.

However, as the total strain amplitude increased, the slope of the curve became steeper, which could also be seen from the results obtained by Noster and Scholtes [5]. For each total strain amplitude up to about 20 cycles, the curves were almost horizontal. The range of 20-50 cycles can be considered as a transition zone, and, after about 50 cycles, the slope decreased with increasing number of cycles. The following relationship is thus proposed to describe the change:

$$\frac{\Delta\varepsilon_p}{2} = \alpha + \beta \log(N) \quad \text{.....(6)}$$

Where, N is the number of cycles, α is the initial plastic strain amplitude at the 50^{th} cycle, β has a negative value and its absolute value can be considered as a hardening coefficient. Both α and β are dependent on the applied strain amplitude.

Figure 4.9 shows the plot of slope β (evaluated from Figure 4.8) as a function of the total strain amplitude. At the lower total strain amplitudes, the β value decreased slightly with increasing strain amplitudes. When the total strain amplitude was higher than 0.4%, the β value decreased drastically. As a result, the rate of decrease of plastic strain amplitudes increased more rapidly as the total strain amplitude increased above 0.4% during cyclic deformation. This is in agreement with the observation reported in [5].

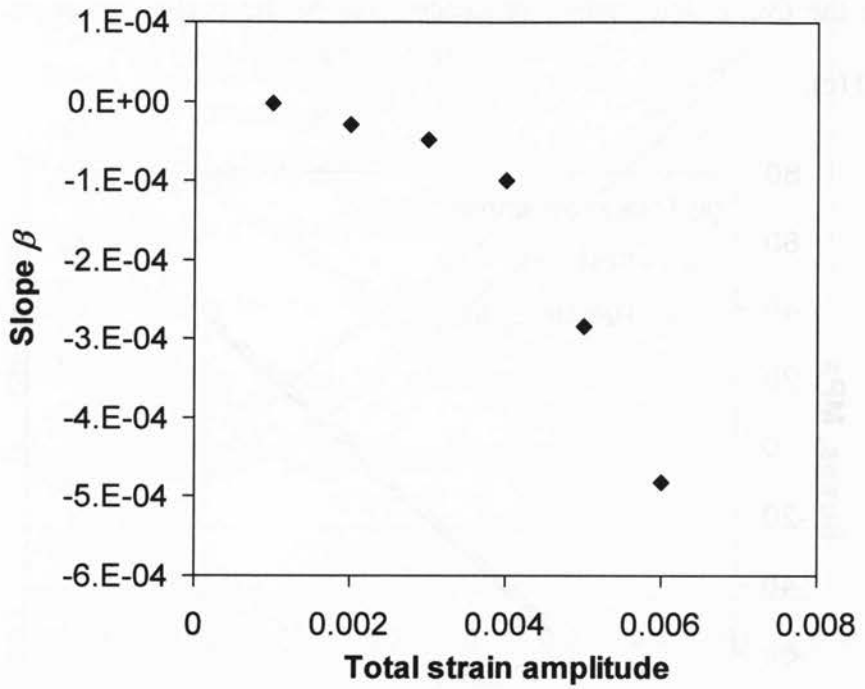

Figure 4.9: Effect of the applied strain amplitudes on the slope β in equation (6)-AZ31 alloy.

4.4.3 Hysteresis Loops and Mean Stress

Typical hysteresis loops for strain amplitudes of 0.1%, 0.3% and 0.6% are shown in Figure 4.10 (a)-(c). It is seen that the stress amplitude did not show the hardening effect at the lower strain amplitudes of 0.1% and 0.2%; therefore, the hysteresis loops did not change much in the entire fatigue process. But at the higher strain amplitudes, the difference in the initial and the mid-life cycle hysteresis loops was clearly observed, exhibiting the strain hardening effect due to plastic deformation. The hysteresis loops at the beginning of the fatigue life were strongly asymmetrical with pronounced plastic yielding in the compression phase of the cycle. The hysteresis loop asymmetry slightly

reduced as the cyclic deformation proceeded due to the cyclic hardening, as seen in Figure 4.10 (c).

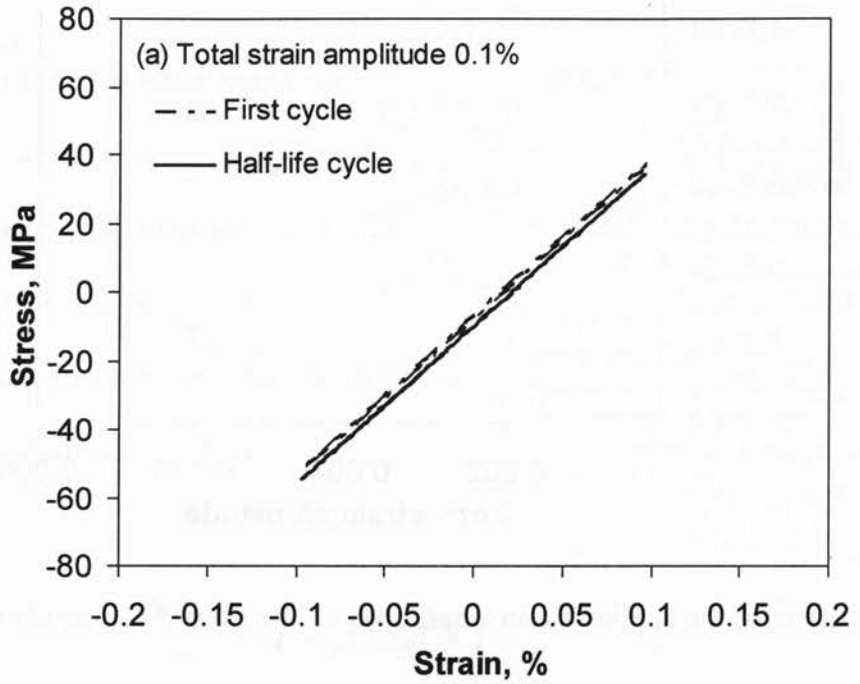

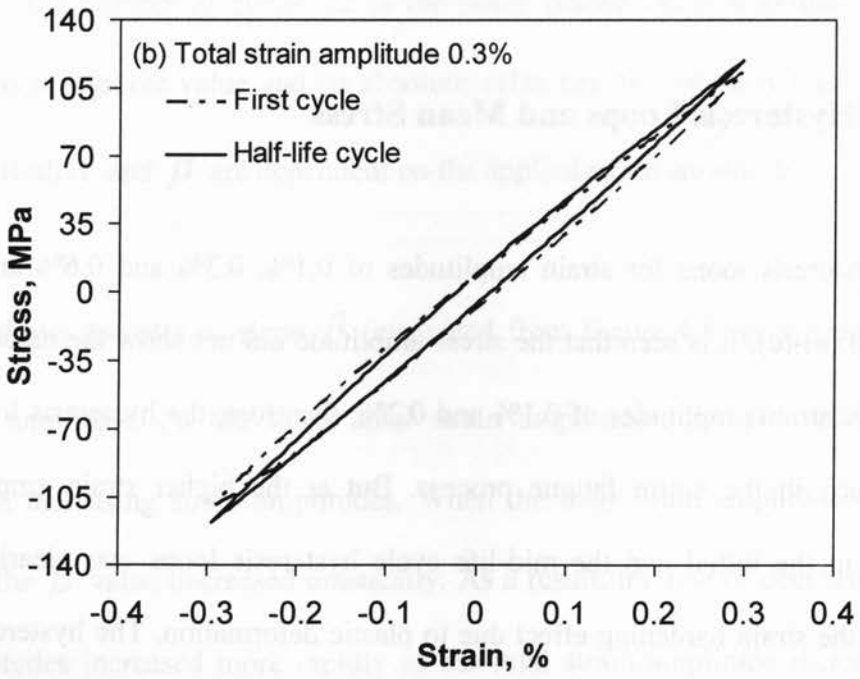

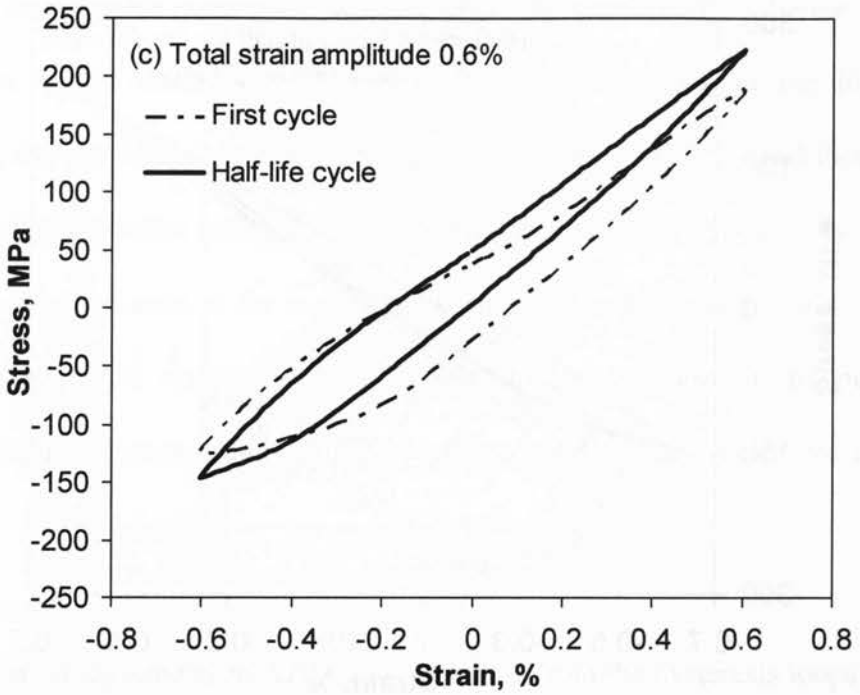

Figure 4.10: Typical hysteresis loops of AZ31 alloy at the first cycle and half-life cycle at different total strain amplitudes of (a) 0.1%, (b) 0.3%, and (c) 0.6%.

Figure 4.11 shows the effect of strain amplitudes on the shape of hysteresis loops, where all the loops at the half life of the LCF tests are plotted. At the lower strain levels (0.1%, 0.2%), the compressive stress was almost the same as the tensile stress. With increasing total strain amplitude, the asymmetry between the tensile and compressive stresses increased progressively. At the higher strain amplitudes (0.5% and 0.6%), a considerable difference between the tensile and compressive stresses appeared. This can also be seen in Figure 4.12, where the mean stress is plotted as a function of the number of cycles at different applied strain amplitudes. The mean stress increased with increasing total strain amplitudes, which is also in agreement with the result reported in [5, 6].

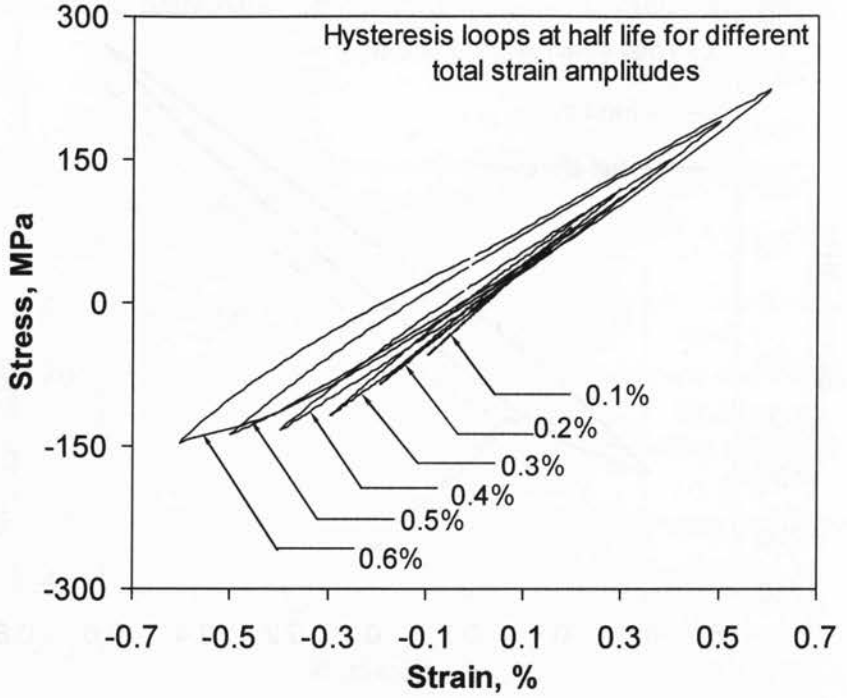

Figure 4.11: Hysteresis loops of AZ31 alloy at the half-life cycle for different total strain amplitudes.

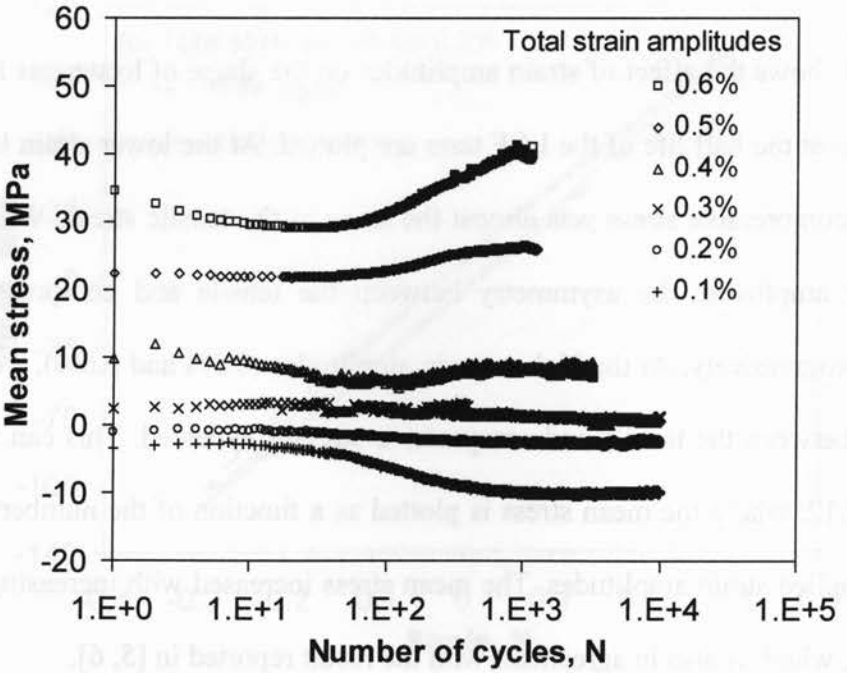

Figure 4.12: Mean stress of AZ31 alloy versus the number of cycles.

In general, the negative mean stress would increase fatigue lifetime, whereas the positive mean stress would decrease the fatigue lifetime [5-7]. Also, at the higher strain amplitudes, the mean stress initially decreased up to about 50 cycles and then increased. A similar initial reduction and subsequent increase in the mean stress was also reported in the strain controlled tests at the higher strain amplitudes [6]. The increase in the mean stress after about 50 cycles would be related to the decrease of the plastic strain amplitude with increasing number of cycles (Figure 4.8), as also described by equation (6).

The deformation asymmetry in AZ31 alloy obtained from the hysteresis loops at different strain amplitudes also concurs with the results reported by other investigators [5, 39]. The effect of deformation anisotropy on fatigue behavior of magnesium alloys was also reported by Thomas *et al.* [40]. The deformation asymmetry behavior of metals is normally associated with the Bauschinger effect [23]. After having examined the hysteresis loops obtained at different strain amplitudes in Figure 4.11, it can be clearly seen that, at lower strain amplitudes, the Bauschinger effect is not as strong as at higher strain amplitudes. At the total strain amplitudes of 0.1% and 0.2%, the ratio of the compressive to the tensile stress was almost 1, indicating that there was almost no deviation in the tensile and compressive yielding. However, at higher strain amplitudes, the stress ratio decreased to ~0.6, which implies that the yielding in the compressive phase occurred earlier than that in the tensile phase. It was also observed that, at cycle 1 and at the half-life cycle, the stress ratio showed no significant change. At 0.6% strain amplitude, the stress ratio is 0.64 for the first cycle and 0.65 for the half life. At strain

amplitudes of 0.4% and 0.5%, similar asymmetry was observed at the initial and half-life cycles. The yielding asymmetry in the AZ31 magnesium alloy reported in other publications [5, 41-43] showed resemblance to the results presented above. This is basically due to the activity of twinning in compression during unloading and subsequent untwinning in tension during loading [41].

4.4.4 Change of Elastic Modulus during Cyclic Deformation

As pointed out by Sommer *et al.* [44], the change in the elastic modulus during cyclic deformation of a roller bearing steel SAE 52100 was associated with the asymmetries in the shape of the hysteresis loops. Therefore, the variation of elastic modulus during the cyclic deformation of the extruded AZ31 magnesium alloy was also evaluated. Figures 4.13, 4.14 and 4.15 show the modulus of elasticity in the loading and unloading phases, and the average value, respectively, vs. the number of cycles on a semi-log scale, where the loading modulus is the slope of the curve of the hysteresis loop after the reversal at the minimum stress and the unloading modulus is the slope of the curve of the same hysteresis loop after the reversal at the maximum stress.

The initial modulus of elasticity at the beginning of low cycle fatigue was higher at small strain amplitudes, which remained almost constant. The increase in the total strain amplitudes led to a decrease in the initial modulus in both loading and unloading phases (Figures 4.13 and 4.14).

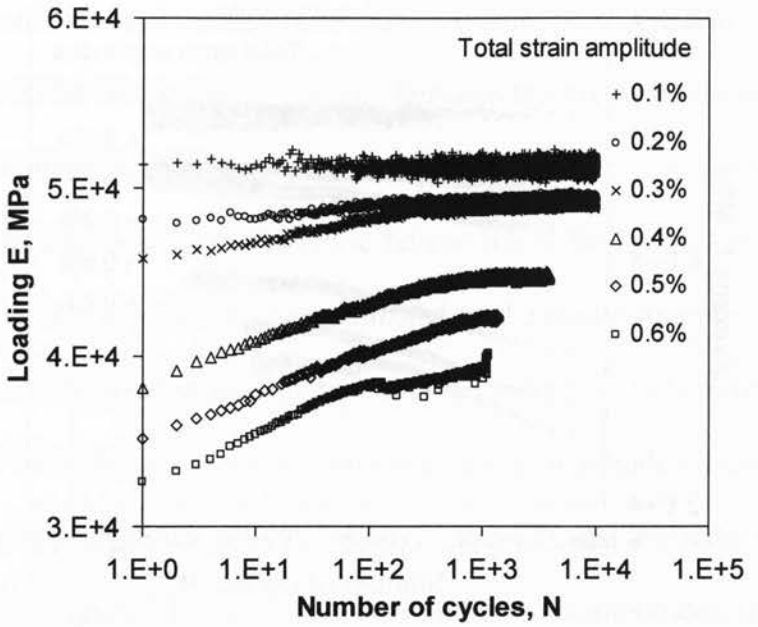

Figure 4.13: Variation of loading modulus of AZ31 alloy with the number of cycles at different strain amplitudes.

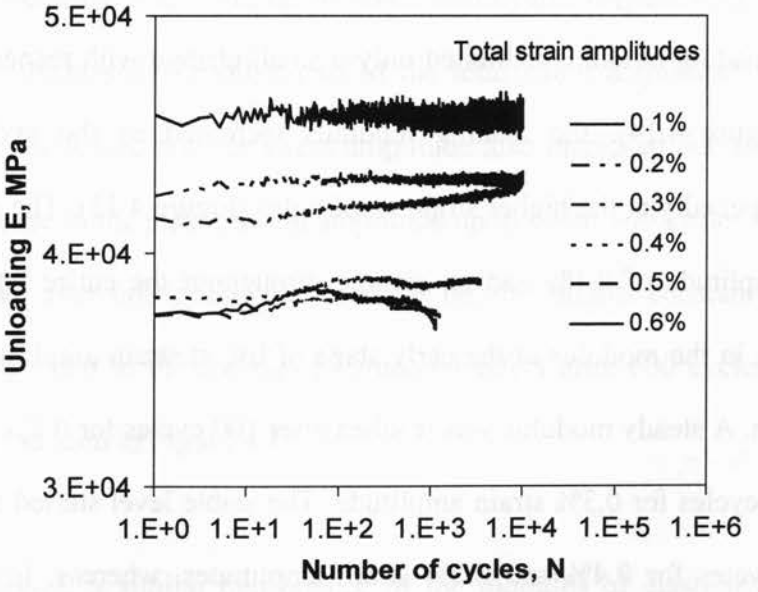

Figure 4.14: Variation of unloading modulus of AZ31 alloy with the number of cycles at different strain amplitudes.

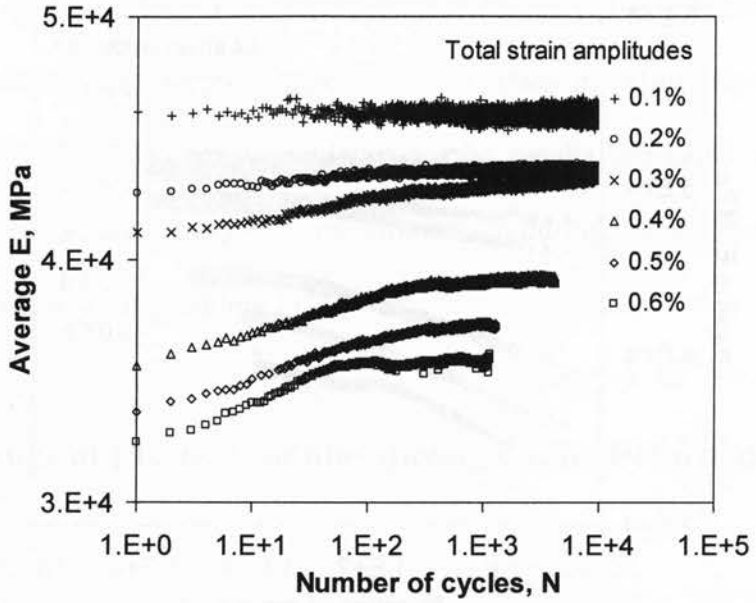

Figure 4.15: Variation of average modulus of AZ31 alloy with the number of cycles at different strain amplitudes.

While the unloading modulus exhibited only a small change with respect to the number of cycles (Figure 4.14), the loading modulus increased as the cyclic deformation progressed, especially at the higher strain amplitudes (Figure 4.13). The loading modulus at a strain amplitude of 0.1% had no change throughout the entire fatigue process. A slight increase in the modulus at the early stage of life at strain amplitudes of 0.2% and 0.3% was seen. A steady modulus was reached after 100 cycles for 0.2% strain amplitude and after 250 cycles for 0.3% strain amplitude. The stable level started at approximately 600 to 850 cycles for 0.4% and 0.5% strain amplitudes, whereas, for the high strain amplitude (0.6%), the modulus increased until failure and no stable stage was observed. Due to the strong increase in the loading modulus (Figure 4.13), the increase in the average modulus at the higher strain amplitudes also increased significantly as the cyclic deformation proceeded, as shown in Figure 4.15.

Based on the Holloman-type equation $\sigma = E\varepsilon^n$, within the elastic limit, the modulus is a constant value and it represents the linearity between the stress and the strain, i.e., n=1 and Hooke's law holds true. The curves shown in Figure 4.14 for the unloading modulus do agree with this equation. Since the entire fatigue life at the low total strain amplitude (0.1% strain amplitude in Figure 4.8) is dominated by the elastic strain (plastic strain is in the order of 1% of the total stain amplitude), so the modulus of elasticity obtained was constant for the entire fatigue process. As the total strain amplitude increased, the plastic part of the total strain amplitude also increased (Figure 4.8), and this reduced the modulus more significantly (Figure 4.14). For each level of the strain amplitudes, the plastic strain amplitude during initial cycles was large, as shown in Figure 4.8. For example, at the strain amplitude of 0.4%, the plastic strain amplitude was initially large, then decreased and the rate of decrease was high, up to about 600 cycles (Figure 4.8). As the plastic strain amplitude decreased, the other part of the total strain amplitude, i.e., the elastic strain amplitude, increased and the stress amplitude also increased due to the hardening effect. The decrease in the plastic strain amplitude up to about 600 cycles would increase the modulus, and, after 600 cycles, the modulus became almost constant (Figure 4.13). This also corresponded to the ending of hardening effect after 600 cycles for the 0.4% strain amplitude, as seen in Figure 4.7.

As mentioned above, a similar dependence of the modulus of elasticity during cyclic loading was observed for the roller bearing steel SAE 52100 [44], where the elastic modulus was found to be stress-dependent as a consequence of nonlinear elastic effects, also referred to as pseudoelasticity. Pseudoelasticity may arise from several origins such

as reversible movement of dislocations, twinning, and stress induced phase transformations. Twinning pseudoelasticity is caused by the reversible movement of twin boundaries, since the position of the twins in the deformed state is not stable, and a driving force can cause them to return upon unloading [45]. Caceres *et al.* [45] have recently examined the change of elastic modulus in a cast AZ91 magnesium alloy, using tensile loading-unloading procedures, and observed that, with increasing plastic strain up to 1-2%, the elastic modulus decreased drastically, i.e., the anelastic or pseudoelastic strain could cause a decrease of up to 70% in the elastic modulus of the alloy. This was attributed to the partial reversal of $\{10\bar{1}2\}$ twins upon unloading [45]. The decrease of the elastic modulus with increasing applied strain amplitude, observed in the present fully-reversed strain-controlled LCF tests of the extruded AZ31 magnesium alloy (Figures 4.13-4.15), is in agreement with the results reported in [45].

4.4.5 Fatigue Life and Low Cycle Fatigue Parameters

Total strain amplitudes $\left(\frac{\Delta\varepsilon_t}{2}\right)$ vs. the number of cycles to failure $(2N_f)$ on a semi-log scale are shown in Figure 4.16. To obtain the fatigue parameters required for the calculation of fatigue life, $\log\left(\frac{\Delta\sigma}{2}\right)$ vs. $\log\left(\frac{\Delta\varepsilon_p}{2}\right)$, $\log\left(\frac{\Delta\varepsilon_e}{2}\right)$ vs. $\log(2N_f)$ and $\log\left(\frac{\Delta\varepsilon_p}{2}\right)$ vs. $\log(2N_f)$ are plotted and the relevant parameters are summarized in Table 4-2.

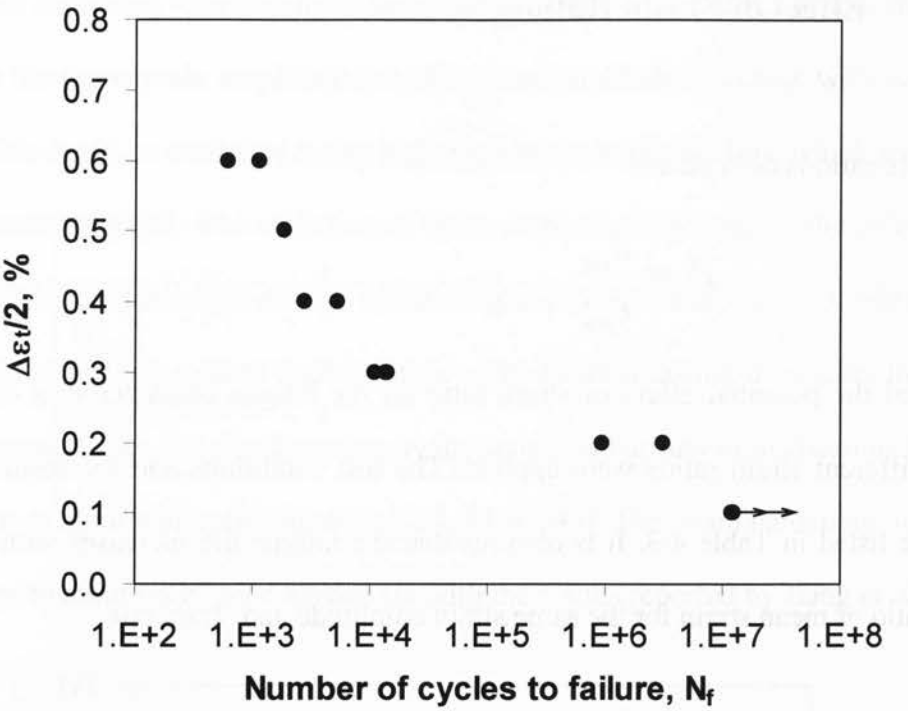

Figure 4.16: Total strain amplitude as a function of the number of cycles to failure for the extruded AZ31 magnesium alloy.

Table 4-2 Low cycle fatigue parameters for the extruded AZ31 magnesium alloy.

Low Cycle fatigue parameters	**Extruded AZ31**
Cyclic strain hardening exponent, n'	0.34
Cyclic strength coefficient, K', MPa	1976
Fatigue strength coefficient, σ_f', MPa	616
Fatigue strength exponent, b	-0.15
Fatigue ductility coefficient, ε_f', %	1.78
Fatigue ductility exponent, c	-0.40

4.4.6 Effect of Strain Ratio

The strain ratio is defined as:

$$R_s = \frac{\varepsilon_{min}}{\varepsilon_{max}} \quad \text{.....(7)}$$

To reveal the potential effect of strain ratio on the fatigue characteristics of the AZ31 alloy, different strain ratios were applied. The test conditions and the resulting fatigue lives are listed in Table 4-3. It is obvious that the fatigue life increases with decreasing strain ratio or mean strain for the same strain amplitude and strain rate.

Table 4-3 Test parameters and fatigue life under different strain ratios at a strain rate of 1×10^{-2} s^{-1} and strain amplitude of 0.4% with the starting loading direction in tension for AZ31.

Strain ratio (R_s)	**Mean strain (ε_{mean}), %**	**Number of cycles to failure, N_f**
0.5	1.2	3545
0	0.4	4090
-0.5	0.13333	4234
-1	0	4294
-2	-0.13333	7189

The evolution of the stress amplitude during cyclic deformation is shown in Figure 4.17. It is of interest to observe that, at the lower (negative) strain ratio, the material shows

higher strain hardening than that at the higher strain ratio. From the figure, it is also clear that, under the same strain amplitude test, the stress amplitude increases with increasing R_s value. This could be attributed to the higher mean strain (Table 4-3), which introduced a higher stress range [6]. The evolution of stress response during the cyclic deformation is an important characteristic of low cycle fatigue process. The cyclic stability of the microstructural features related to dislocation multiplication mainly dominates the cyclic stress response [8, 22, 46]. Furthermore, twins acting as barriers to dislocation slip also facilitate the evolution of cyclic stress [22, 24, 34, 47-49]. The strain hardening due to the formation of twinning is in good agreement with the results reported by Jiang *et al.* [50].

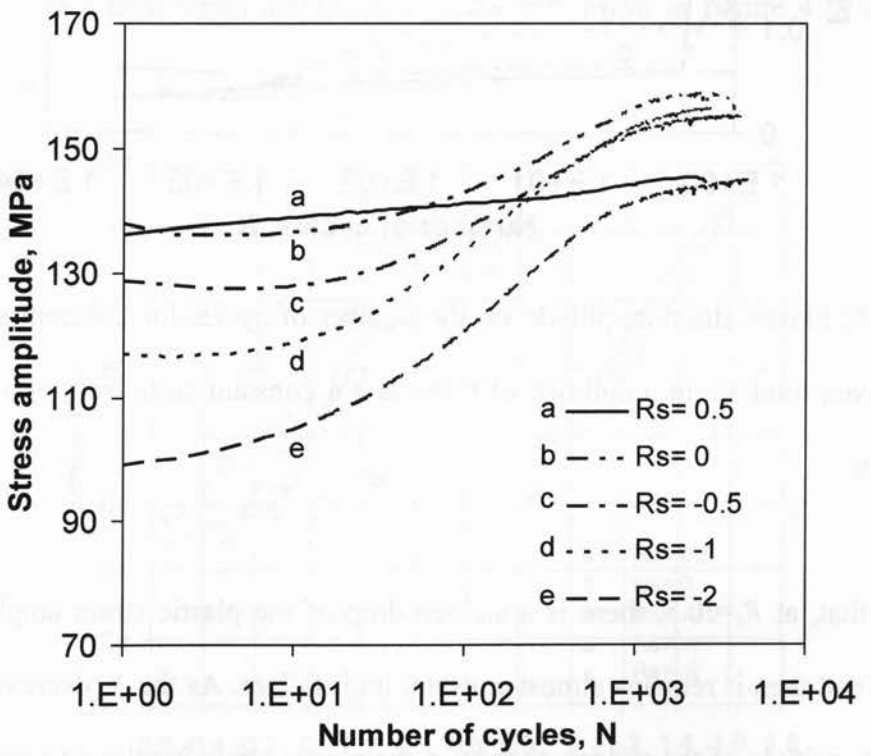

Figure 4.17: Stress amplitude vs. the number of cycles for different strain ratios at a given strain amplitude of 0.4% and a constant strain rate of 1×10^{-2} s^{-1} for AZ31 alloy.

Figure 4.18 shows the variation of the plastic strain amplitude with the number of cycles for different applied strain ratios, R_s.

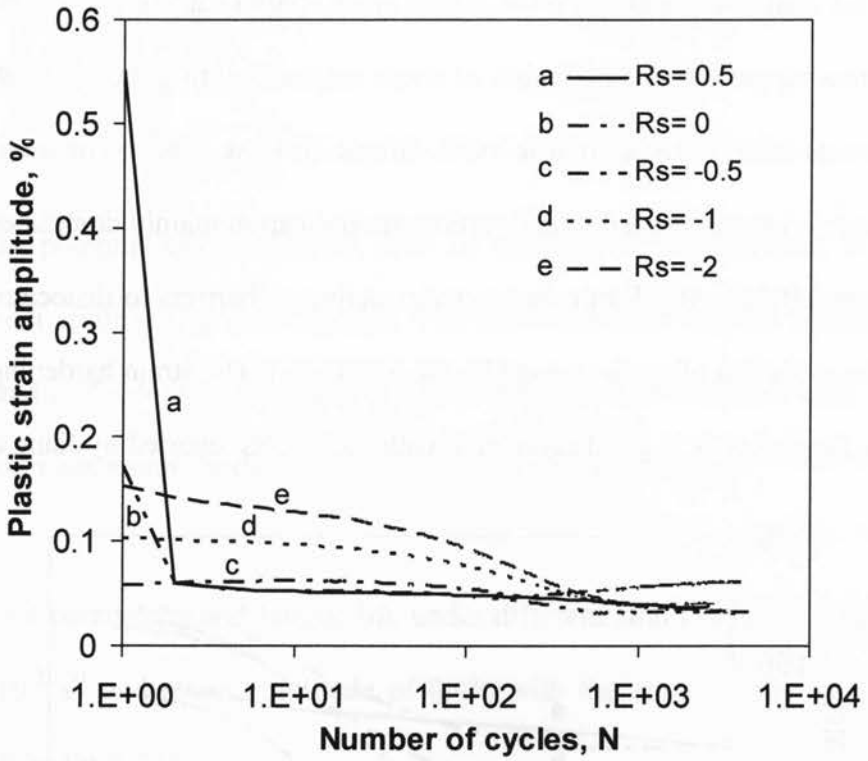

Figure 4.18: Plastic strain amplitude vs. the number of cycles for different strain ratios, R_s, at a given total strain amplitude of 0.4% and a constant strain rate of 1×10^{-2} s^{-1} for AZ31 alloy.

It is seen that, at R_s= 0.5, there is a sudden drop of the plastic strain amplitude at the beginning and then it remains almost constant until failure. As the R_s decreases from 0.5 to 0, the magnitude of the sudden change in the plastic strain amplitude decreases. Such an abrupt drop is related to the high positive mean strain (Table 4-3). At negative strain ratios, the abrupt change disappears and the plastic strain amplitude decreases gradually as the cyclic deformation progresses and it becomes nearly constant after ~750 cycles. It

is also observed that the plastic strain amplitude becomes higher for more negative strain ratios, as indicated by curves c, d and e in Figure 4.18. It is known that, in the plastic deformation of magnesium alloys, twinning plays an important role [22, 42]. The cyclic deformation behavior is mostly dominated by the formation and propagation of the twins as well [51]. In the cyclic deformation process, twinning starts at the compression loading [39] and detwinning occurs at the tension loading [41, 52]. The plastic deformation is explained in the following paragraph in terms of hysteresis loops.

The first cycle hysteresis loops and approximate half-life hysteresis loops for each strain ratio at a constant total strain amplitude of 0.4% are shown in Figure 4.19 and Figure 4.20, respectively.

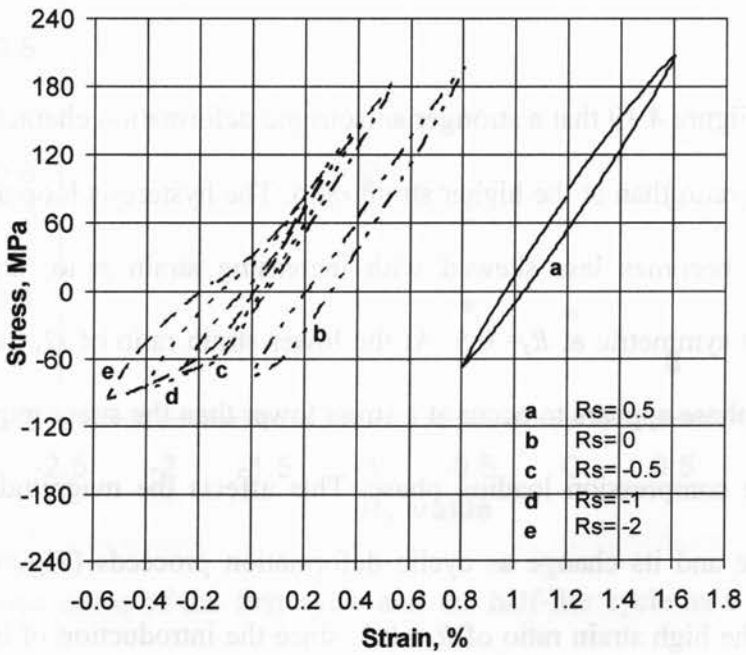

Figure 4.19: Hysteresis loops of the first cycle for different strain ratios for AZ31 alloy.

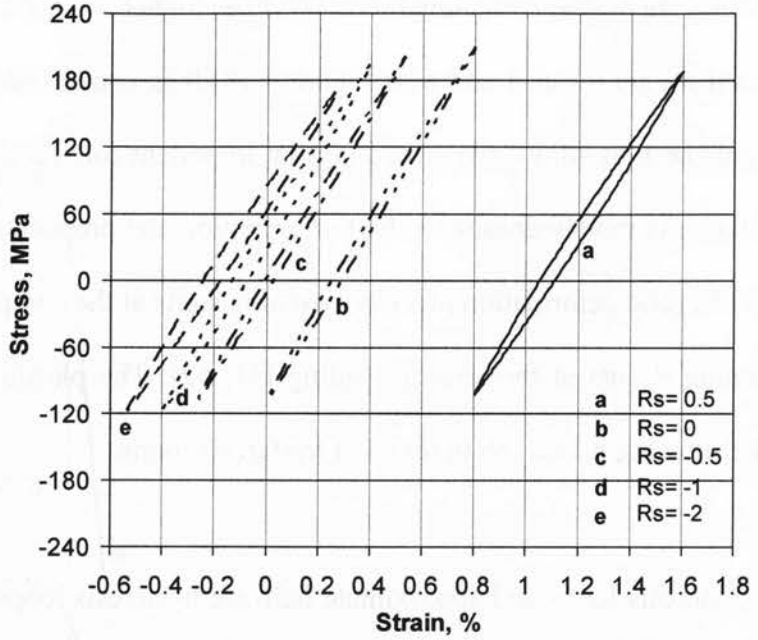

Figure 4.20: Hysteresis loops of the half-life cycle for different strain ratios for AZ31 alloy.

It is seen from Figure 4.19 that a stronger anisotropic deformation characteristic occurs at the lower strain ratio than at the higher strain ratio. The hysteresis loop at R_s= -2 is most skewed, which becomes less skewed with increasing strain ratio, and eventually it becomes almost symmetric at R_s= 0.5. At the lower strain ratio of -2, detwinning in the tensile loading phase appears to occur at a stress lower than the stress required to activate twinning in the compression loading phase. This affects the magnitude of the plastic strain amplitude and its change as cyclic deformation proceeds (Figure 4.18). On the other hand, at the high strain ratio of R_s= 0.5, since the introduction of high mean strain (Table 4-3) causes an insufficient compressive stress, the twinning is basically not involved, leading to the disappearance of the skewness of the hysteresis loop, as shown in

Figure 4.19. But the minimum-to-maximum stress ratio is lower than that at R_s= -2 (Figure 4.21).

As seen from Figure 4.20, the hysteresis loops of the half-life cycle become basically symmetric but a tensile and compressive stress asymmetry is observed. This is attributed to the tensile and compressive yield asymmetry observed in wrought magnesium alloys [39]. The obtained compressive-to-tensile stress ratio of the first cycle and the half life cycle as a function of the applied strain ratio is shown Figure 4.21.

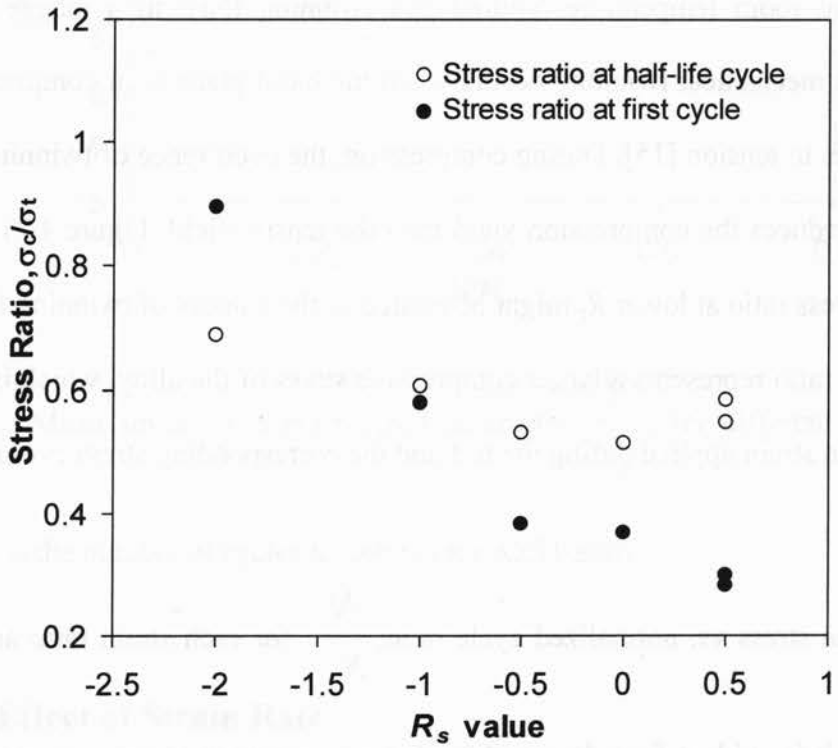

Figure 4.21: Stress ratios of the first cycle and the half-life cycle as a function of the applied strain ratio for AZ31 alloy.

The stress ratio evaluated from the first cycle test data decreases as the strain ratio increases. But when the test specimen reaches its half life, due to plastic deformation and stress relaxation, the stress ratio becomes smaller than the initial value (except for the R_s= -2 test), and, as the R_s increases, the stress ratio decreases and it continues to decrease until R_s= 0 and then the stress ratio increases. The compressive stress is much larger at the lower strain ratio. The twinning during compression and detwinning during tension control the yield behavior of the alloy [5, 39, 42, 53]. It is well known that two characteristic deformation mechanisms occur during the plastic deformation of magnesium at room temperature: sliding and twinning [53]. In a magnesium single crystal, basic mechanical twinning occurs when the basal plane is in compression or the prism plane is in tension [15]. During compression, the occurrence of twinning along the basal plane reduces the compression yield than the tensile yield. Figure 4.21 shows that the higher stress ratio at lower R_s might be related to the amount of twinning formed. The higher stress ratio represents a larger compressive stress of the alloy, which is associated with the mean strain applied during the test and the corresponding stress evolution.

Plots of mean stress vs. normalized cycle ratio, $\frac{N}{N_f}$, for each strain ratio are shown in Figure 4.22. It is evident from Figure 4.22 that a lower mean stress was obtained at the lowest than at the highest strain ratio. It can be seen that the mean stress relaxation occurs during the 5-10% of the fatigue life and, near the half life cycle, it becomes stabilized for the applied strain ratios, except for the strain ratio 0.5. This is in good agreement with the tests presented by Goodenber and Stephens [9]. The mean stress in the 0.5 strain ratio test

decreases throughout the entire fatigue life and it never become stable. The amount of stress relaxation is significant for the strain control test of R_s= -1.

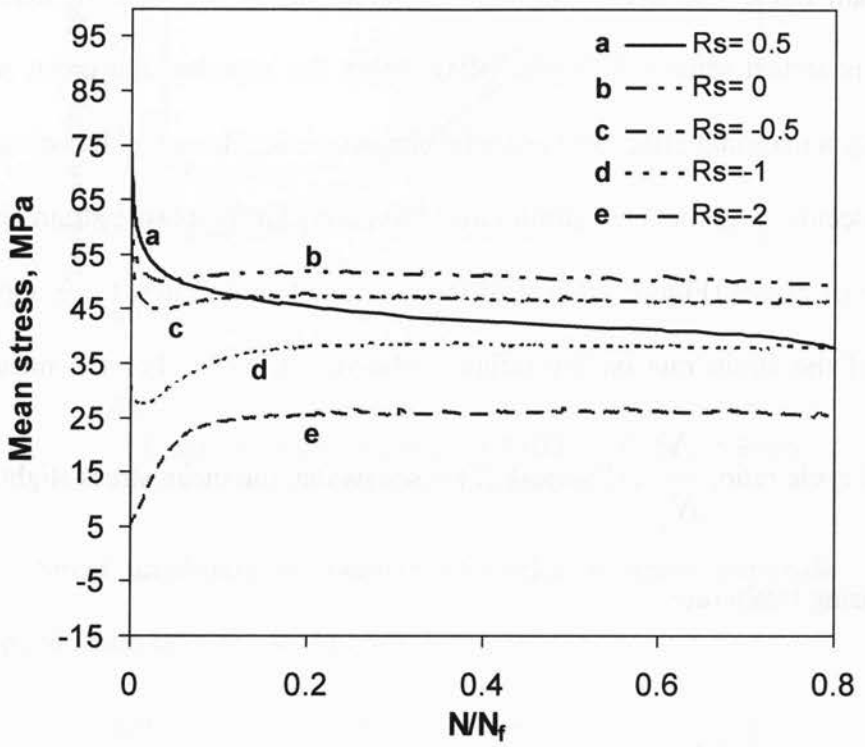

Figure 4.22: Mean stress vs. a normalized parameter, $\frac{N}{N_f}$, for different strain ratios (where N_f is the number of cycles to failure) for AZ31 alloy.

4.4.7 Effect of Strain Rate

Three different strain rates $(\dot{\varepsilon})$ - very low, moderate and very high were applied to examine the strain rate effect on the fatigue life of the AZ31. Table 4-4 lists the test results of the applied strain rates. It is seen that a higher strain rate corresponds to longer

fatigue life. Figure 4.23 shows the stress evolution during the low cycle fatigue tests where the stress amplitude vs. the number of cycles to failure is plotted for different applied strain rates. The stress amplitude evolved during the high, moderate and low strain rate is almost same (~120-130 MPa) within the experimental error, so the strain rate has only a marginal effect on the cyclic characteristic. However, it is clear that cyclic hardening occurs at all the three strain rates. Similarly, for the plastic strain amplitude vs. the number of cycles (Figure 4.24) at different applied strain rates, there appears almost no effect of the strain rate on the fatigue behavior of AZ31. For the mean stress vs. normalized cycle ratio, $\frac{N}{N_f}$, (Figure 4.25) it seems that the mean stress slightly increases with increasing strain rate.

Table 4-4 Variation of fatigue lifetime with the strain rate applied at a strain amplitude of 0.4% and strain ratio of -1 with the starting loading direction in tension for AZ31.

Strain rate, s^{-1}	**Number of cycles to failure, N_f**
1×10^{-3}	2467
1×10^{-2}	4294
8×10^{-2}	7268

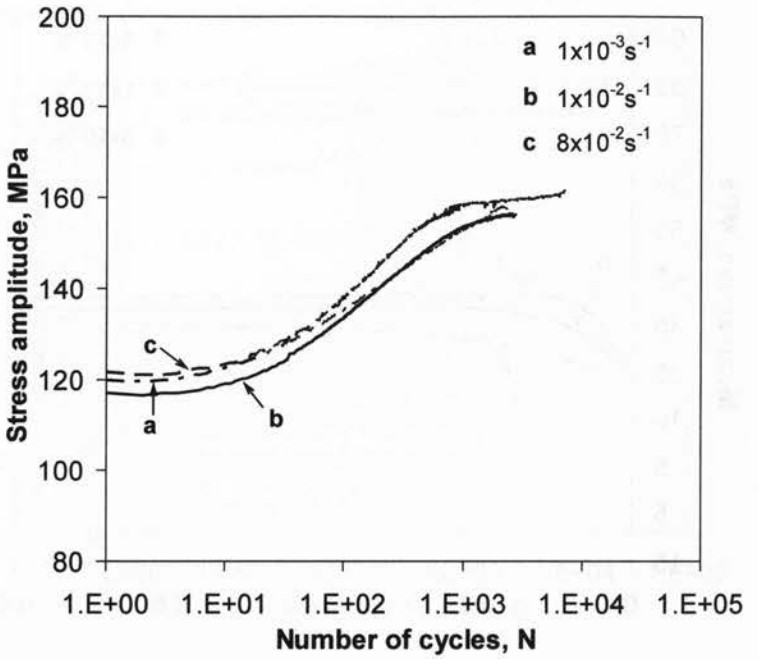

Figure 4.23: Stress amplitude vs. number of cycles at strain amplitude of 0.4% at different applied strain rates for AZ31 alloy.

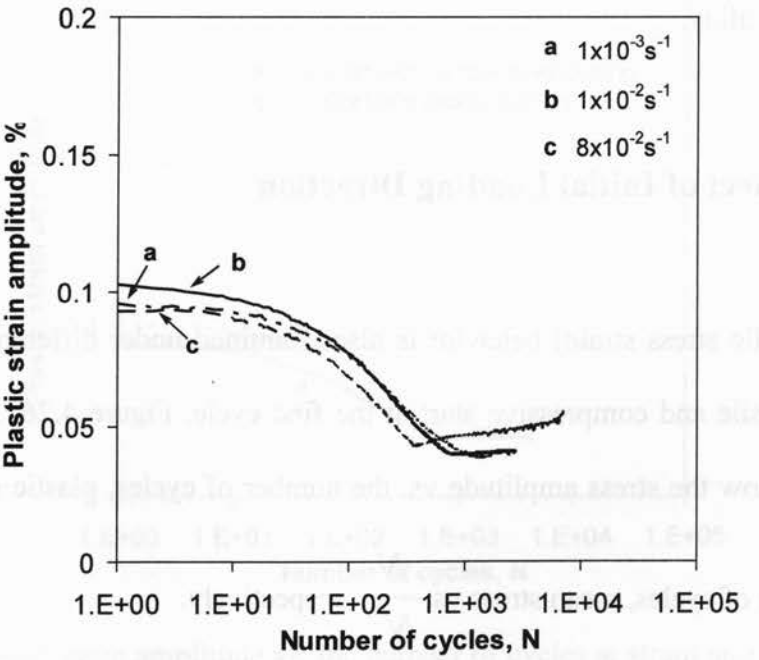

Figure 4.24: Plastic strain amplitude vs. the number of cycles at a strain amplitude of 0.4% and different applied strain rates for AZ31 alloy.

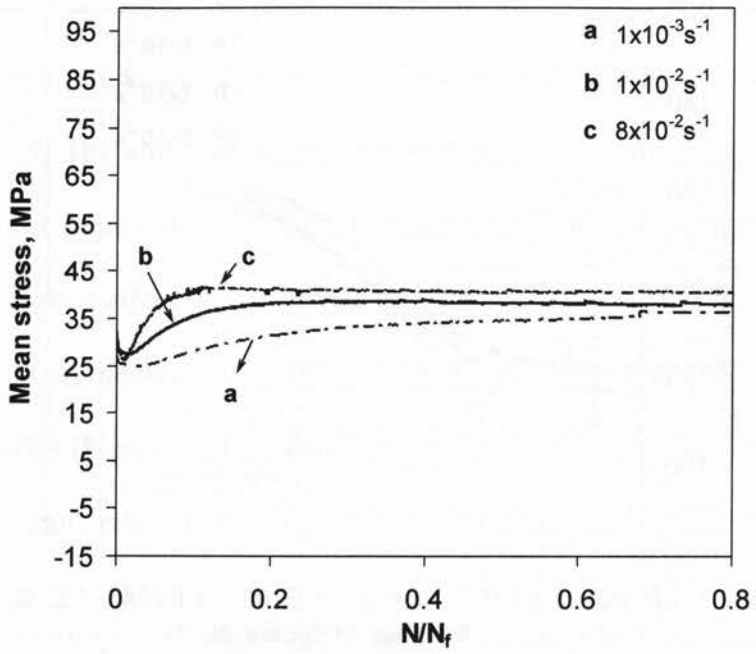

Figure 4.25: Mean stress vs. a normalized parameter, $\frac{N}{N_f}$, at different applied strain rates for AZ31 alloy.

4.4.8 Effect of Initial Loading Direction

The CSS (cyclic stress strain) behavior is also examined under different initial loading directions: tensile and compressive start at the first cycle. Figure 4.26, Figure 4.27 and Figure 4.28 show the stress amplitude vs. the number of cycles, plastic strain amplitude vs. the number of cycles, mean stress vs. $\frac{N}{N_f}$, respectively.

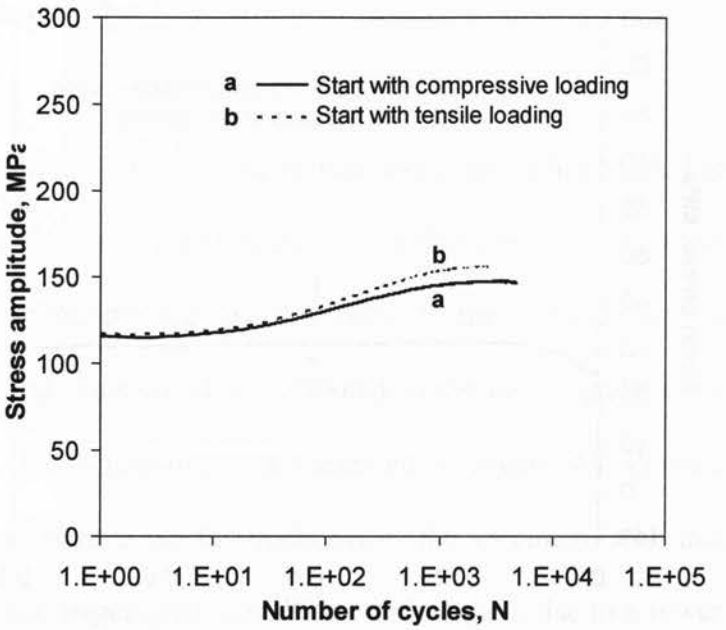

Figure 4.26: Stress amplitude vs. the number of cycles at a strain amplitude of 0.4% in different initial loading directions for AZ31 alloy.

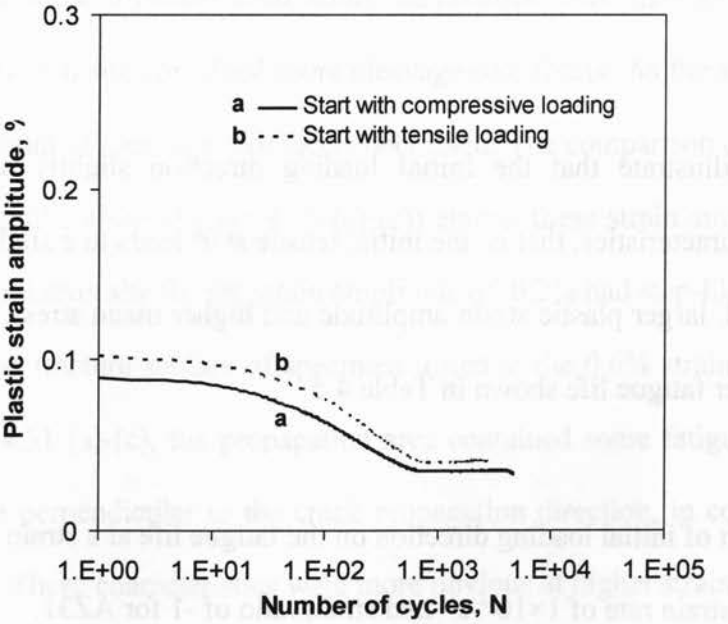

Figure 4.27: Plastic strain amplitude vs. the number of cycles at strain amplitude of 0.4% in different loading directions for AZ31 alloy.

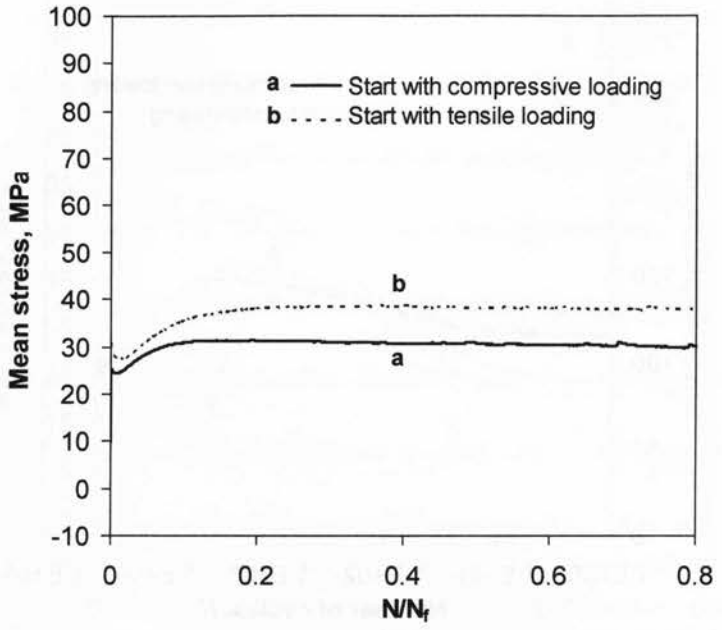

Figure 4.28: Mean stress vs. a normalized parameter, $\frac{N}{N_f}$, in different loading directions for AZ31 alloy.

These results illustrate that the initial loading direction slightly affects the cyclic deformation characteristics, that is, the initial tensile start leads to a slightly greater cyclic hardening trend, larger plastic strain amplitude and higher mean stress, corresponding to a slightly shorter fatigue life shown in Table 4-5.

Table 4-5 Effect of initial loading direction on the fatigue life at a strain amplitude of 0.4%, strain rate of 1×10^{-2} s^{-1} and strain ratio of -1 for AZ31.

Initial loading direction	**Number of cycles to failure, N_f**
Tensile start	4294
Compressive start	5482

4.4.9 Fractography

Fracture surfaces of fatigued specimens were examined using SEM. Figure 4.29 (a)-(c) shows some typical images taken at low magnifications. It is seen that fatigue cracks initiated basically from the specimen surface. At the initiation site the cleavage-like facets were observed. This could be attributed to the coarse grain sizes of the material near the surface. The microstructures presented in Figure 4.1 showed a non-uniform distribution of grain size along the thickness of the specimen, with much larger grains near the surface. The larger grain size at the surface gave rise to a lower strength on the basis of the well-known Hall-Petch relationship, and thus led to the fatigue crack initiation at the surface. The basic differences among the three fracture surfaces of samples tested at three different total strain amplitudes were that at the low strain amplitude the initiation site contained more cleavage-like facets. As the strain amplitude increased, the amount of cleavage-like facets decreased. The comparison on the initiation sites at larger magnifications (Figure 4.30 (a)-(c)) among these strain amplitudes clearly showed that the initiation site for the strain amplitude of 0.2% had step-like facets, which were absent on the fracture surface of specimen tested at the 0.6% strain amplitude. As shown in Figure 4.31 (a)-(c), the propagation area contained some fatigue striation-like features that were perpendicular to the crack propagation direction, in conjunction with secondary cracks. These characteristics were more obvious at higher strain amplitudes, as seen in Figure 4.31 (c).

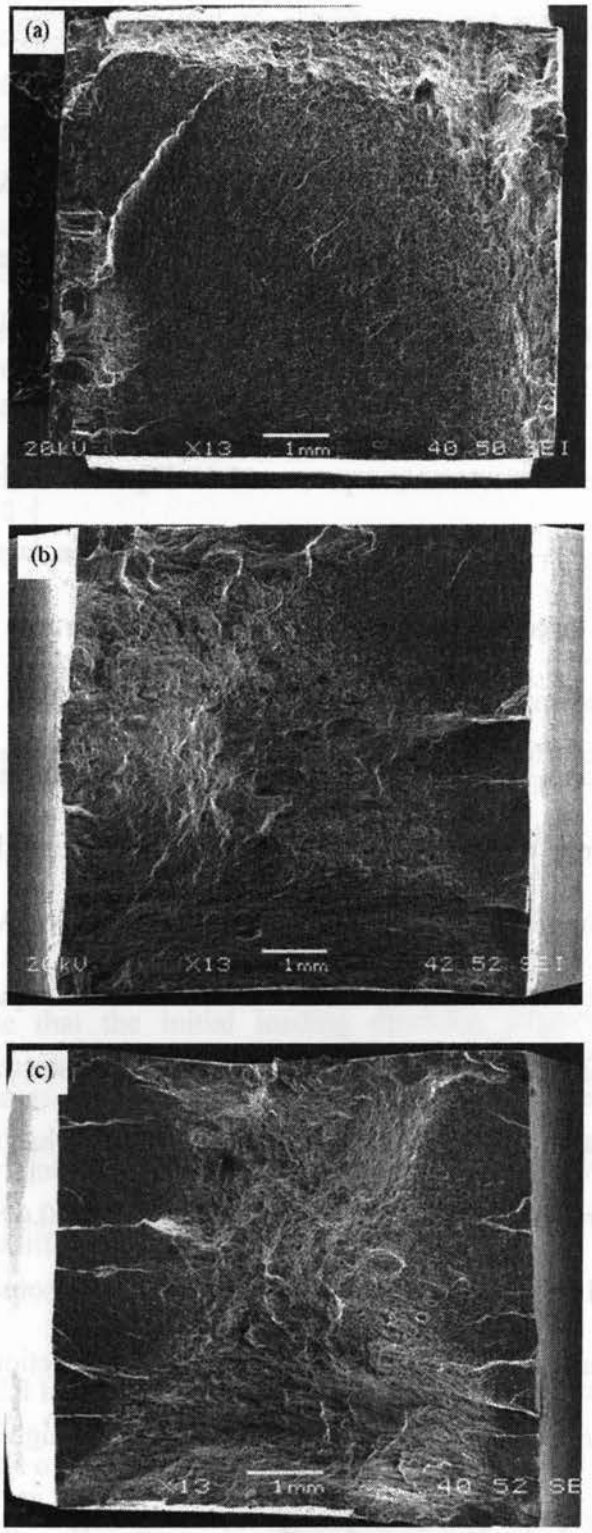

Figure 4.29: SEM images of overall fracture surfaces of specimens fatigued at the total strain amplitudes of (a) 0.2%, (b) 0.4%, and (c) 0.6% for AZ31 alloy.

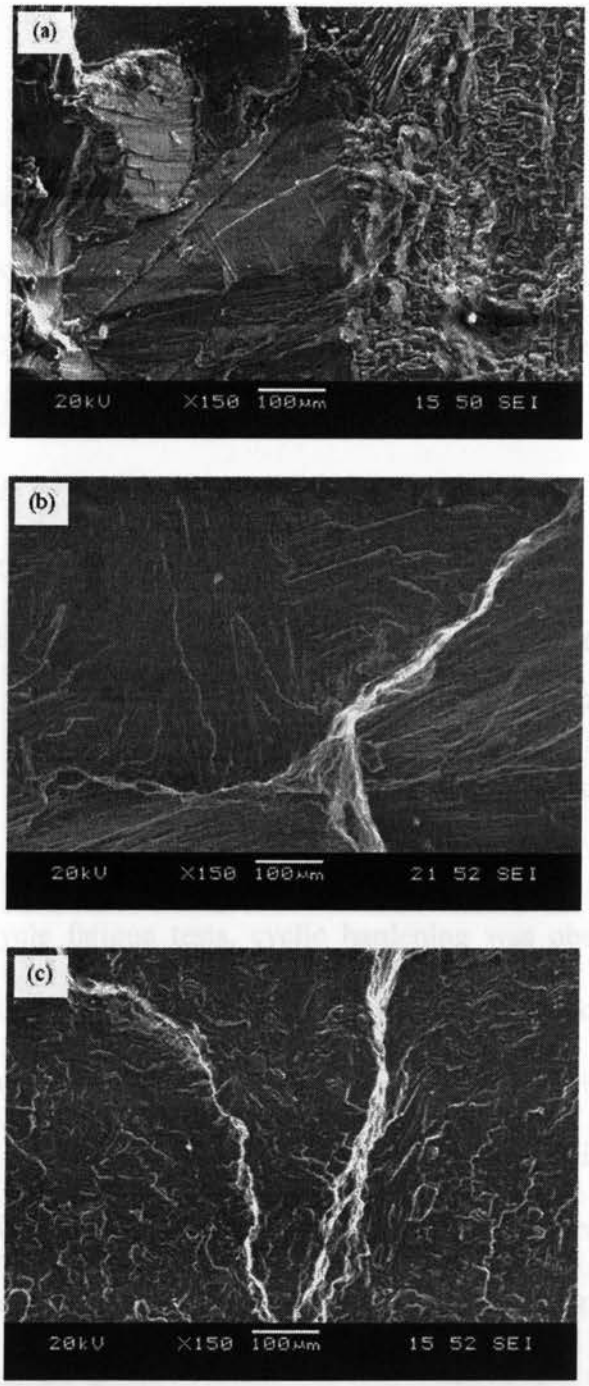

Figure 4.30: SEM micrographs of the fracture surface near crack initiation of the specimens fatigued at the total strain amplitudes of (a) 0.2%, (b) 0.4%, and (c) 0.6% for AZ31 alloy.

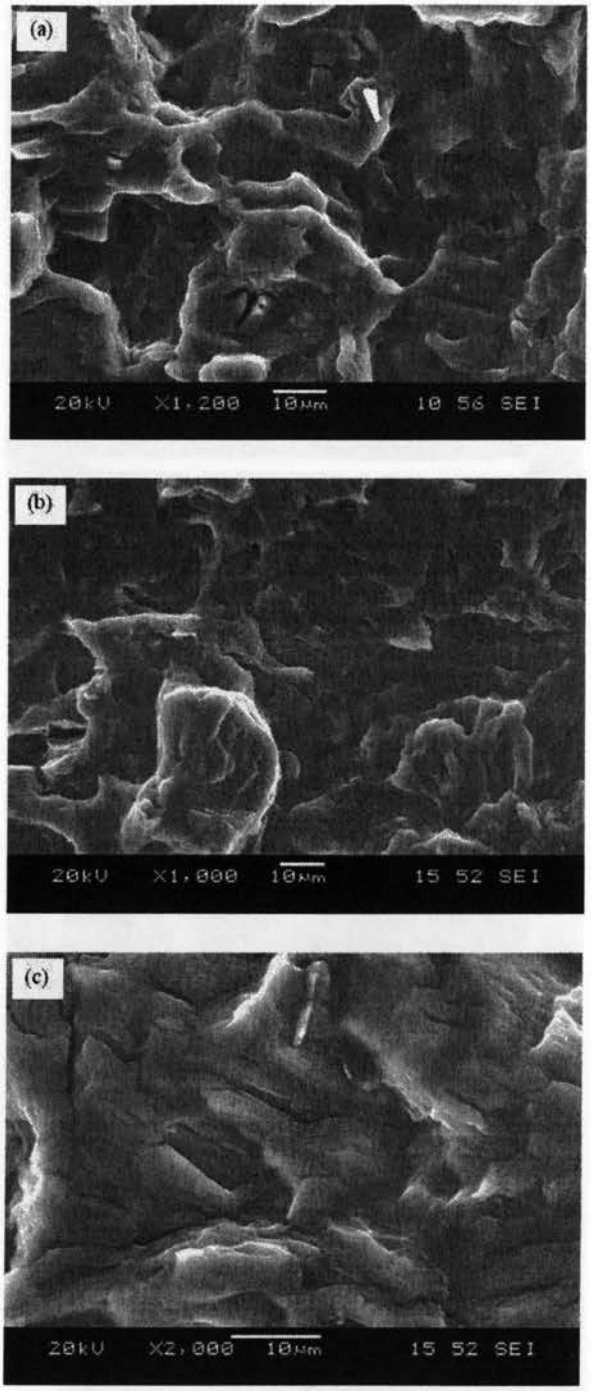

Figure 4.31: SEM micrographs of the fatigue crack propagation region of the specimens fatigued at the total strain amplitudes of (a) 0.2%, (b) 0.4%, and (c) 0.6% for AZ31 alloy.

4.5 Summary

1. Microstructural observation of AZ31 across the thickness in the longitudinal direction showed a non-uniform grain distribution, with a grain size ranging from about 6 μm to about 60 μm. Larger grain sizes were observed near the top and bottom surfaces whereas the middle section exhibited small grains of about 6 μm.
2. Micro-hardness of this alloy basically varied between HV 35 and 50 due to the non-uniform grain size distribution.
3. Tensile test showed a higher strain hardening exponent at a high strain rate. It changed from 0.1 to 0.14 from strain rate $1\times10^{-5}s^{-1}$ to $1\times10^{-2}s^{-1}$. The yield strength and ultimate tensile strength also increased and the ductility decreased with increasing strain rate.
4. During low cycle fatigue tests, cyclic hardening was observed at higher total strain amplitudes, which could be due to the formation and interaction of twins. At low strain amplitudes, the cyclic stress amplitude basically remained constant.
5. Compared to the monotonic tensile tests, the alloy exhibited stronger cyclic hardening capacity. A cyclic strain hardening exponent of 0.34 was obtained, which was much higher than the monotonic strain hardening exponent of 0.14.
6. After an initially stable period of about 50 cycles, the plastic strain amplitude $\left(\frac{\Delta\varepsilon_p}{2}\right)$ decreased linearly with increasing number of cycles (N) on a semi-log scale. Thus the following relationship between the plastic strain amplitude and the log number of cycles was introduced:

$$\frac{\Delta\varepsilon_p}{2} = \alpha + \beta \log(N),$$

The cyclic strain hardening coefficient β with a negative value was observed to decrease with increasing strain amplitude.

7. The Bauschinger effect was pronounced at higher strain amplitudes, leading to a big difference between the tensile and compressive yield stresses and thus asymmetric hysteresis loops. This is basically attributed to the activity of twinning in compression during unloading and subsequent untwinning in tension during loading. The mean stress increased with increasing strain amplitudes.
8. The elastic modulus during cyclic deformation, being constant at the low strain amplitude, was observed to decrease with increasing strain amplitudes and increase with increasing number of cycles at the high strain amplitudes due to the presence of pseudoelastic behavior.
9. Fatigue lifetime increased with decreasing strain amplitude. The fatigue parameters used to determine the fatigue life following the Coffin-Manson law and Basquin's equation were evaluated.
10. Stronger cyclic strain hardening was observed to occur at the lower strain ratio than at the higher strain ratio. This is due to the fact that the formation of twins during the cyclic deformation in the compressive phase and the twins acting as subsequent barriers to dislocation slip and pile-up were the main cause for occurrence of the cyclic strain hardening. The decrease of cyclic strain hardening capacity at the higher strain ratio was due to a smaller compressive stress, leading to the formation of fewer twins.

11. The strain ratio at R_s=-2 gave rise to an obvious skewness on the hysteresis loop of the first cycle because of the presence of larger compressive stress. With increasing strain ratio, the skewness of the hysteresis loop vanished gradually.
12. While the initial stress ratio decreased drastically with increasing strain ratio applied, this decrease became modest at the half life.
13. As the strain ratio or mean strain decreased, the fatigue life of the extruded AZ31 magnesium alloy increased.
14. The effect of strain rate on the cyclic deformation characteristics seemed to be not so significant, but the fatigue life of the AZ31 alloy was observed to increase with increasing strain rate.
15. The initial tensile start seemed to give rise to slightly greater cyclic hardening, larger plastic strain amplitude and higher mean stress, and resulted in a slightly shorter fatigue life.
16. SEM examination revealed that fatigue cracks initiated from the specimen surface due to the larger grain sizes near the specimen surface. The initiation site contained cleavage-like facets, which were observed to decrease as the strain amplitude increased.
17. The atigue crack propagation area was basically characterized by fatigue striation-like features, coupled with the presence of the secondary cracks.

CHAPTER 5

MECHANICAL PROPERTIES OF AM30 EXTRUDED MAGNESIUM ALLOY

5.1 Microstructure

Figure 5.1(a)-(d) shows typical microstructures of extruded AM30 alloy across the thickness (7mm). It is seen that the microstructure was also non-uniform along the thickness of the specimen and the grain size varied from the top to bottom of the surface.

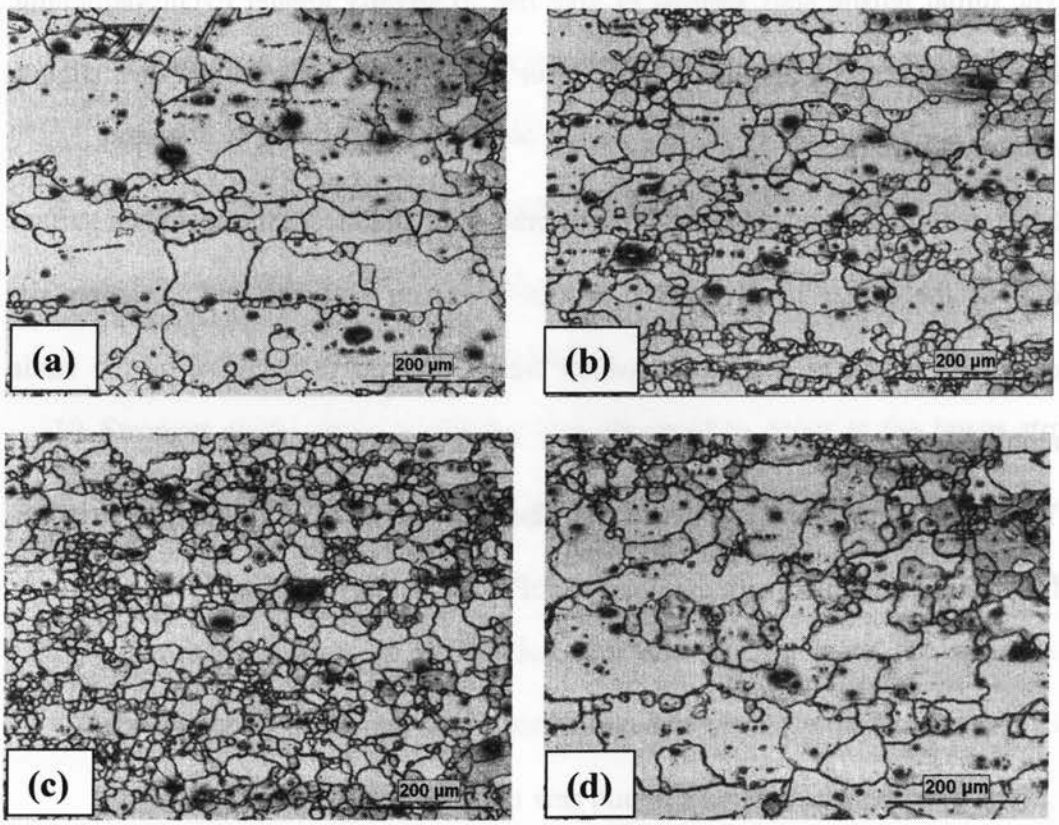

Figure 5.1: Optical microscope images of (a) near the top surface zone, (b) transition zone, (c) small grain zone, and (d) near the bottom surface zone for AM30 alloy.

Larger grains were observed at both top and bottom surfaces of the specimen. The top surface contained a layer of large grains about 0.9 mm into the surface with an average grain size of about 44 μm, as shown in Figure 5.1 (a). Figure 5.1 (b) shows the transition of the grains, and this layer was about 3.5 mm wide. Apparently the grains became smaller and the lower section of the specimen contained an average grain size of about 15 μm, as shown in Figure 5.1 (c). This layer contained clusters of very fine grains less than 8 μm of size around comparatively large grains and the thickness of this layer is about 2 mm. The bottom of the specimen contained a thin layer (~0.6 mm) of larger grains of about 25 μm of size. EDS analysis revealed that the black dots on the specimen surface are similar to Mn-Al particles, which were also observed in AZ31.

5.2 Micro-hardness

Figure 5.2 shows a typical hardness profile along the 7 mm thickness for viewed in the longitudinal direction. From the hardness profile it is seen that the hardenss of AM30 varies within the range of 32-48 HV. Dashed lines are used to define different grain size zones. Due to the presence of large grains near the top and bottom surface zones, the hardness is low. The average hardness is about 39 HV near the bottom surface, which increases to an average of about 45 HV because of the presence of the very small clusters of grains. And near the top surface the grains have an average hardness of about 36 HV. The wide variation in the hardness values was consistent with the wide range of grain sizes present in the microstructure.

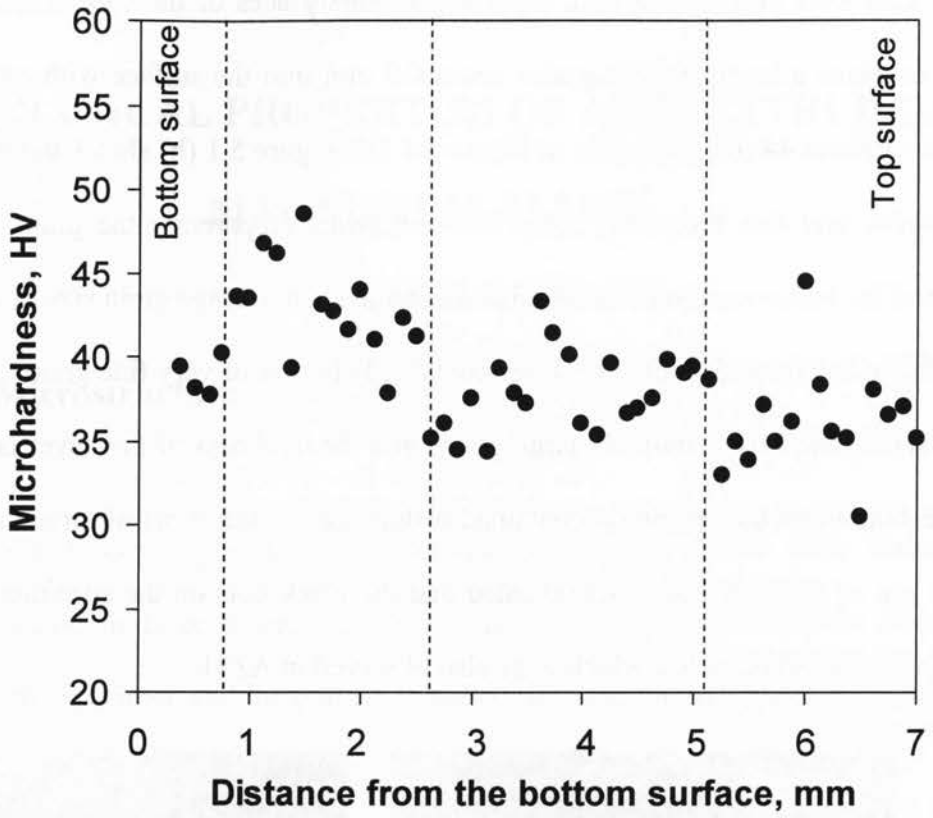

Figure 5.2: Micro-hardness profile along the thickness of plate viewed in the longitudinal direction for AM30 alloy.

5.3 Tensile Properties of AM30

5.3.1 Tensile Strength and Ductility

Figure 5.3 shows the stress vs. strain curve at four different strain rates at room temperature. As expected, flow stress decreases with decreasing strain rate. The ductility of AM30 was characterized in terms of elongation (%) to fracture.

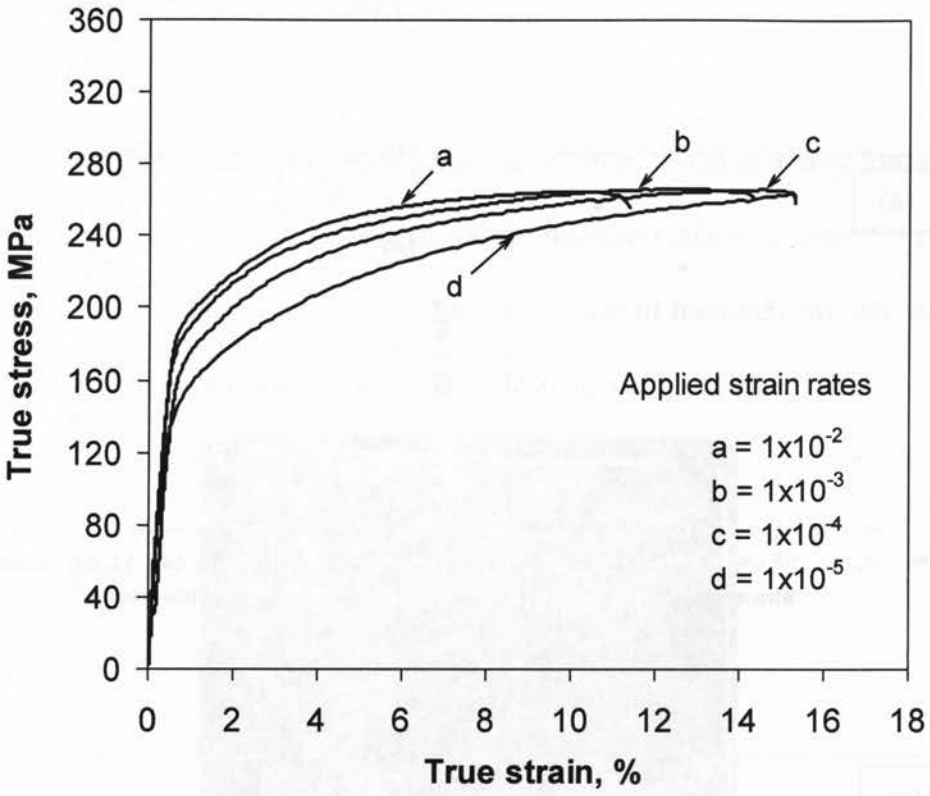

Figure 5.3: Stress-strain curves obtained at four different strain rates for AM30.

It is seen that the elongation decreases with increasing strain rate. It is well known that the uniform deformation is directly related to the strain hardening exponent, *n*. The effect of strain rate on the yield strength (YS), ultimate tensile strength (UTS), % elongation and *n* value are shown in Figure 5.4 (a), (b), (c) and (d), respectively. From these figures, it is seen that yield strength, ultimate tensile strength increases with increasing strain rate. But the elongation or ductility of the alloy decreases with increasing strain rate. One obvious difference from the normal dependence of *n* value on strain rate was observed, i.e., the n value decreases with increasing strain rate. This phenomenon was reported by Jiang *et al.* [19], and this could be due to the softening effect by contraction twinning. In comparison with AZ31, the *n* value of AM30 is higher.

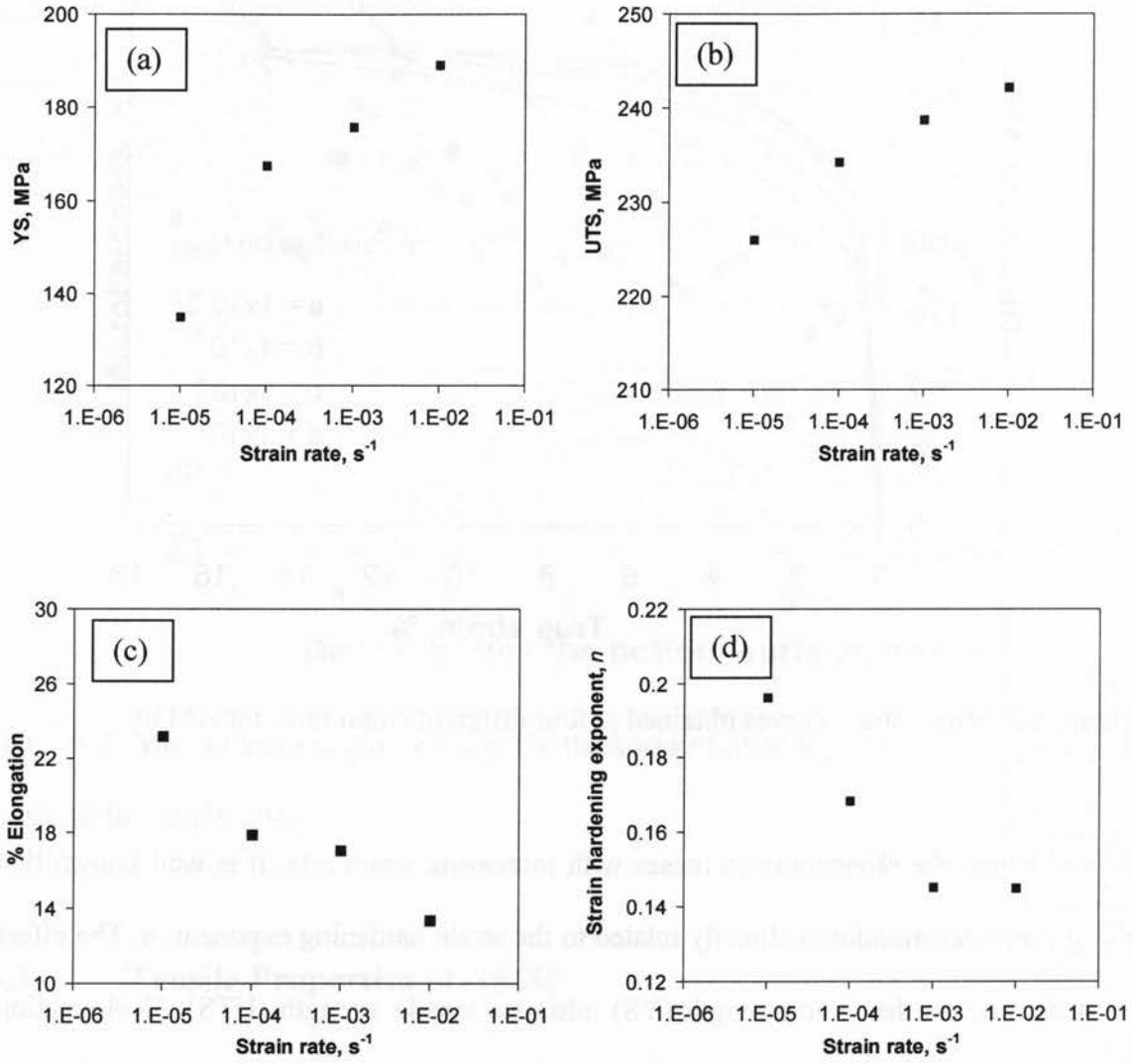

Figure 5.4: The dependence of tensile properties on the strain rate, (a) YS, (b) UTS, (c) % elongation and (d) strain hardening exponent curves for AM30.

5.3.2 Tensile Fracture Surfaces

Figure 5.5 (a) and (b), shows the tensile fracture surfaces tested at a very low strain rate ($1\times10^{-5}s^{-1}$). Grain pull outs are very clear on the fracture surface. Figure 5.5 (b) shows the magnified view of the fractured specimen. The mode of fracture is mostly mixed type with the presence of brittle facets and few ductile elongated dimples.

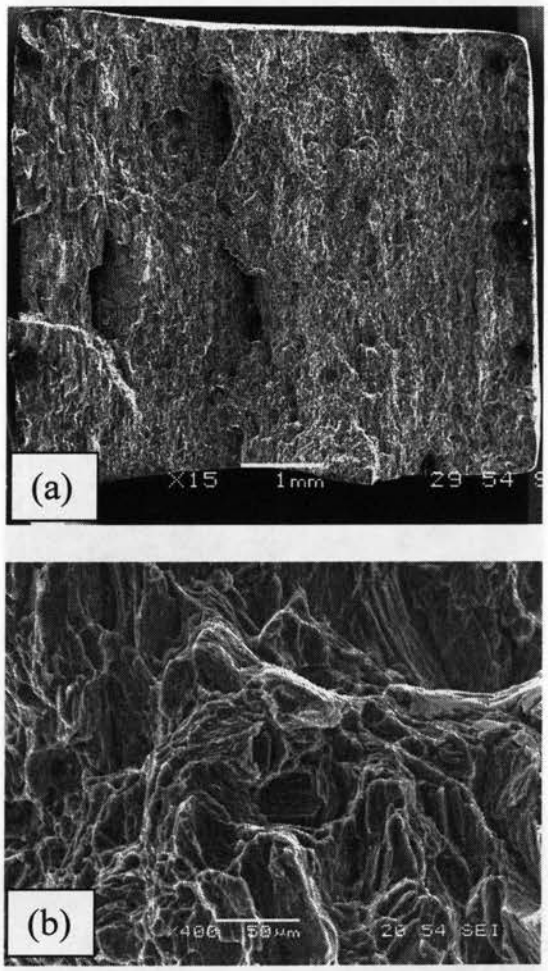

Figure 5.5: SEM micrographs of fracture surfaces of AM30 alloy after tensile testing at a strain rate of $1\times10^{-5}s^{-1}$, (a) entire fracture surface (b) magnified view of the fracture surface.

Figure 5.6 (a) and (b), shows the tensile fracture surfaces tested at a strain rate of $1\times10^{-3}s^{-1}$. Grain pull-outs are also present in this specimen. However, the magnified view (Figure 5.6) shows very clear presence of brittle cleavage like facets. Few ductile type fractures are also observed. And Figure 5.7 (a) and (b), shows the tensile fracture surfaces tested at a high strain rate of $1\times10^{-2}s^{-1}$. Along with the presence of brittle facets and ductile type fracture surface, the specimen also shows large grain pullouts. These grain pull-outs are mainly micro-voids, formed near the twinned region during the deformation and grew into large cavities by means of void inter-linkage.

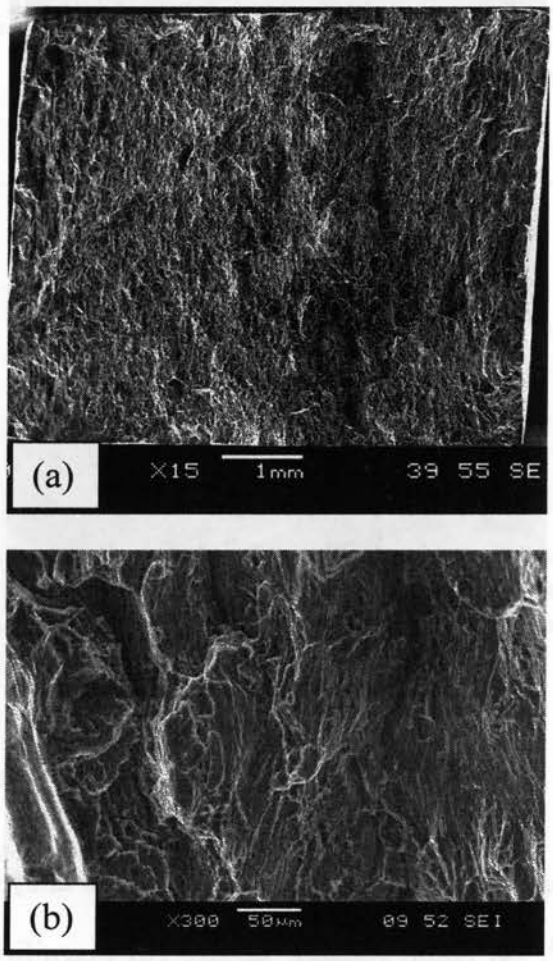

Figure 5.6: SEM micrographs of fracture surfaces of AM30 alloy after tensile testing at a strain rate of $1\times10^{-3}s^{-1}$, (a) entire fracture surface (b) magnified view of fracture surface.

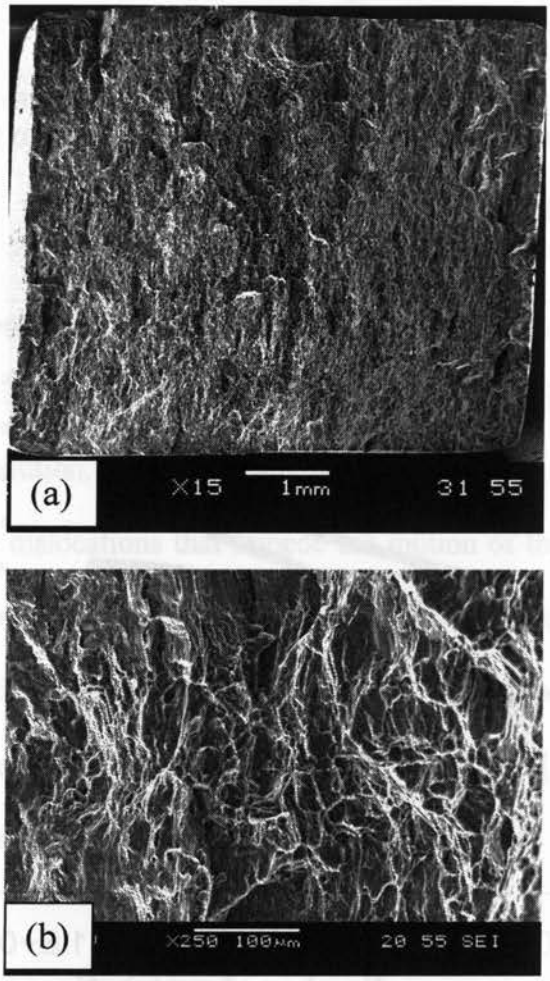

Figure 5.7: SEM micrographs of fracture surfaces of AM30 alloy after tensile testing at a strain rate of $1\times10^{-2}s^{-1}$, (a) entire fracture surface (b) magnified view of mixed type fracture surface.

5.4 Low Cycle Fatigue Properties of AM30

5.4.1 Stress Response during Cyclic Deformation

Figure 5.8 shows the evolution of stress amplitude with respect to the number of cycles at different strain amplitudes.

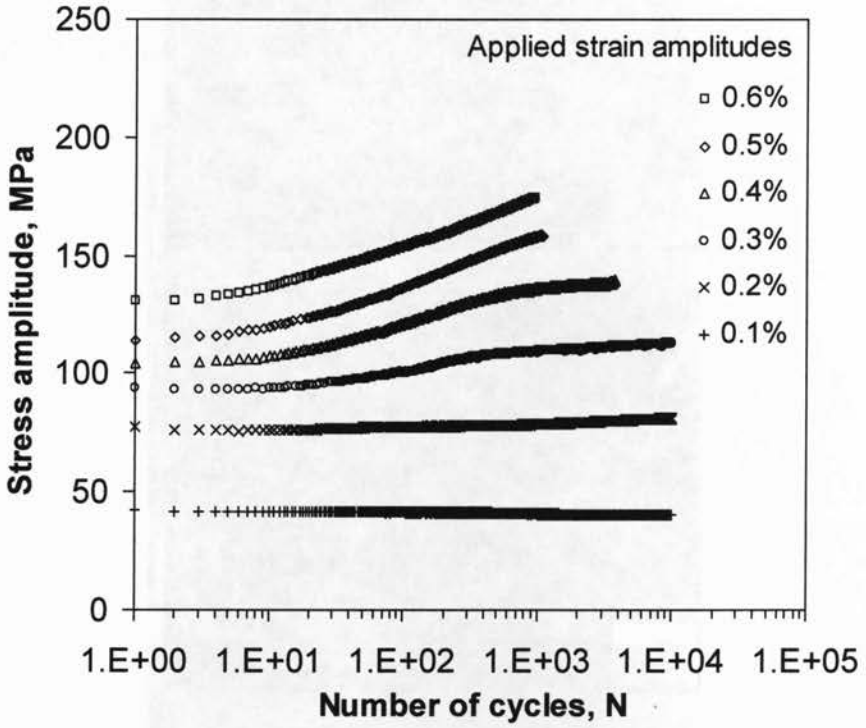

Figure 5.8: Stress amplitude vs. the number of cycles at different total strain amplitudes for AM30 alloy.

High strain amplitudes (0.6%, 0.5% and 0.4%) showed a higher degree of strain hardening than the low strain amplitudes (0.2% and 0.1%). Except for 0.2% and 0.1% tests, strain hardening of AM30 appeared stronger than AZ31 [11]. Noster and Scholtes

[5] reported in their work on AZ31 extruded alloy that strain hardening effect was very small at room temperature; rather, they reported basically the effect of temperature on the stress amplitude response, while the results presented in this investigation and by some others [6-9, 11, 13] showed that at room temperature, the material could undergo cyclic strain hardening at high strain amplitudes.

During the cyclic deformation of the low cycle fatigue process, the evolution of the stress amplitude was an important characteristic. The cyclic response was dominated by the cyclic stability of the microstructural features, dislocation multiplication and slip systems [46]. During stress evolution, the strain hardening phenomenon mainly arose from the interactions among the dislocations that impede the motion of the dislocations. The hcp structure of magnesium alloys facilitated twinning which acted as a barrier to the movement of dislocations and caused the formation of dislocation pile-ups, which initiated the back stress and resulted in the strain hardening [23, 24, 46]. Twinning induced softening was also observed due to the annihilation and rearrangement of dislocations [21].

Plastic deformation of magnesium alloys was largely affected by twinning [8, 19, 21, 24, 35-38, 46, 47, 54-56]. As reported by Brown *et al.* [37], twinning was associated with the low stress flow regime, and typically evolved within a stress level of 70-200 MPa (0.1%-0.8% strain) for the AZ31 alloy. The stress amplitudes for the occurrence of the strain hardening observed in the present investigation was 95-160 MPa, which is within the range reported by Brown *et al.* [37]. In this stress range, twinning occurred to

accommodate the deformation due to tensile or compressive stress. Basically, compression loading introduced twinning, whereas tension led to detwinning in the magnesium alloy [8, 41]. The strain hardening of AM30 alloy was basically related to the formation of residual twins during the cyclic loading. As reported by Wu. *et al.* [8], residual twins formed after the act of twinning and detwining of each cycle, and, with increasing number of cycles, the volume fraction of residual twins increased, leading to an increases hardening rate. In the strain amplitudes between 0.6% and 0.3% in Figure 5.8, the amount of residual twins formed during each cycle in the initial stage of 5-20 cycles might not be enough to initiate the hardening, but, after these cycles, residual twins increased with increasing number of cycles and thus increased the strain hardening rate.

Figure 5.9 shows the variation of mean stress with the applied strain amplitude in the AM30 extruded alloy. The mean stress increased from 0 MPa to about 40 MPa as the strain amplitude increased from 0.1% to 0.6%. Higher mean stresses would decrease the fatigue lifetime [5, 6, 9, 11]. Also, at the higher strain amplitudes, the mean stress initially decreased up to about 50 cycles and then increased. A similar initial reduction and subsequent increase in the mean stress was also observed in the AZ31 extruded magnesium alloy in the strain controlled tests at the higher strain amplitudes [6, 11]. The increase in the mean stress after about 50 cycles was seen to correspond to the decrease of the plastic strain amplitude with increasing number of cycles (Figure 5.10).

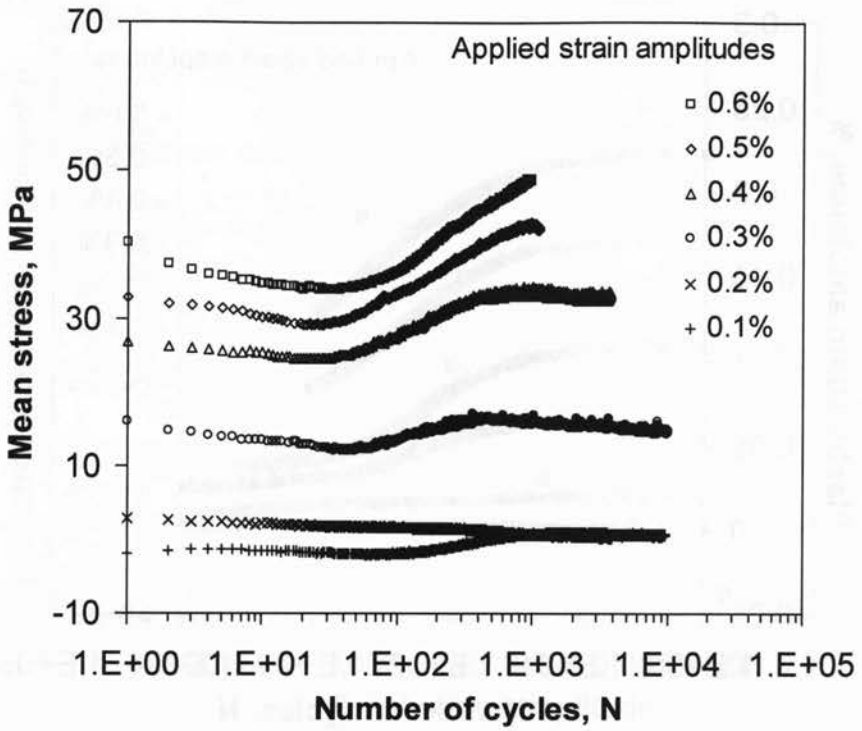

Figure 5.9: Variation of mean stress at different total strain amplitudes for AM30 alloy.

5.4.2 Cyclic Plastic Deformation and Hysteresis Loops

The change of the plastic strain amplitude $\left(\frac{\Delta\varepsilon_p}{2}\right)$ during cyclic deformation is shown in Figure 5.10 at different applied strain amplitudes. As the total strain amplitude increased, the value of plastic strain amplitude also increased and the fatigue life of the material decreased. At lower total strain amplitudes (0.1%, 0.2%), the plastic strain amplitude remained nearly constant over the entire fatigue life.

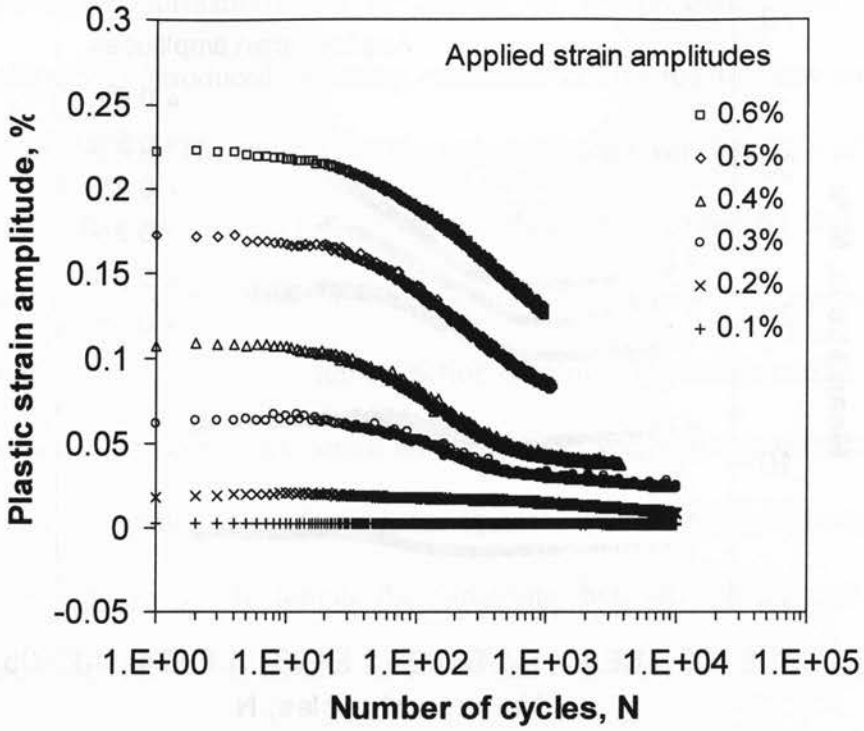

Figure 5.10: Plastic strain amplitude vs. the number of cycles at different total strain amplitudes for AM30 alloy.

However, as the total strain amplitude increased, the slope of the curve on the semi-log scale became steeper, which could also be seen from others reports [5, 6, 8, 11]. At the strain amplitudes of 0.6%-0.3% the plastic strain amplitude was almost horizontal up to about 5-20 cycles, but after about 50 cycles, the slope of the curve decreased with increasing number of cycles, which was also observed in extruded AZ31 [6, 11]. A hardening coefficient (i.e., the slope of the curves in Figure 5.10) β has been defined in [11], which is plotted as a function of the applied total strain amplitudes, as shown in Figure 5.11.

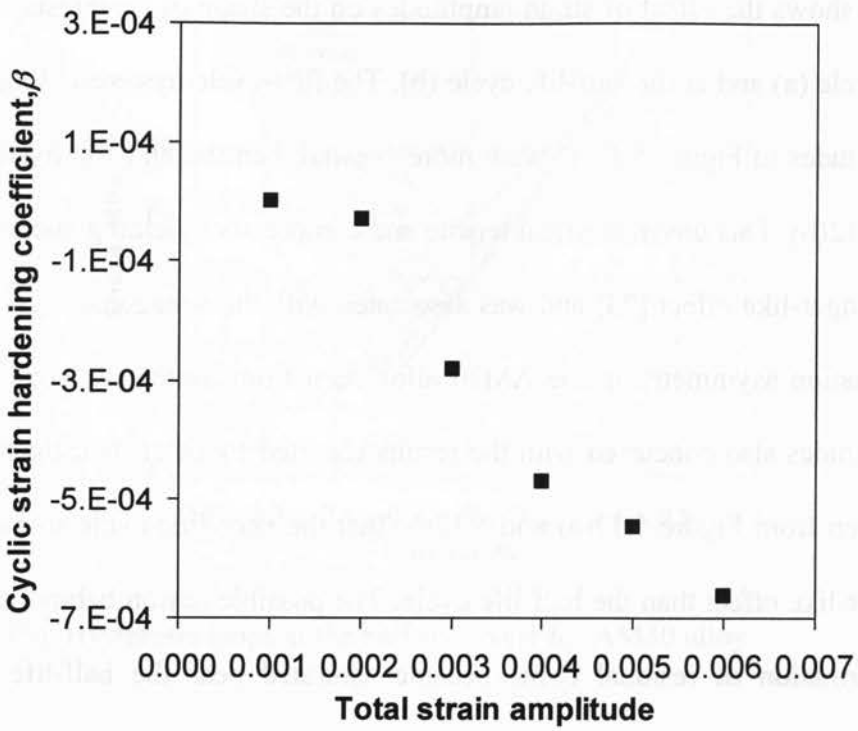

Figure 5.11: Effect of the applied strain amplitude on the strain hardening coefficient β value for AM30 alloy.

At the lower total strain amplitudes, the β value decreased slightly with increasing strain amplitude. When the total strain amplitude was higher than 0.3%, the β value decreased drastically. As a result, the rate of drop-off of plastic strain amplitudes increased more rapidly as the total strain amplitude increased above 0.3% during cyclic deformation. This is in agreement with the observation reported in [5, 11]. However, the absolute value of β for the AM30 alloy was larger than that of the AZ31 alloy when the applied strain amplitude is above 0.3%, indicating that the AM30 magnesium alloy indeed exhibited a stronger cyclic hardening capacity.

Figure 5.12 shows the effect of strain amplitudes on the shape of hysteresis loops, at the very first cycle (a) and at the half-life cycle (b). The first-cycle hysteresis loops at higher strain amplitudes in Figure 5.12(a) were more skewed than the half-life hysteresis loops in Figure 5.12(b). This unsymmetrical tensile and compressive yielding phenomenon was the Bauschinger-like effect [23] and was associated with the hexagonal crystal structure. The deformation asymmetry in the AM30 alloy seen from hysteresis loops at different strain amplitudes also concurred with the results reported by other investigators [5, 6, 8, 11]. It is seen from Figure 5.12(a) and 5.12(b) that the very first cycle showed a higher Bauschinger-like effect than the half-life cycle. The possible reason behind this could be that the formation of residual twins became saturated near the half-life cycle. The yielding asymmetry of several wrought magnesium alloys was also reported in other publications [5, 6, 8, 11, 21, 41] where resemblance to the results presented above was seen. This is basically due to the activity of twinning in compression during unloading and subsequent detwinning in tension during loading [8, 41].

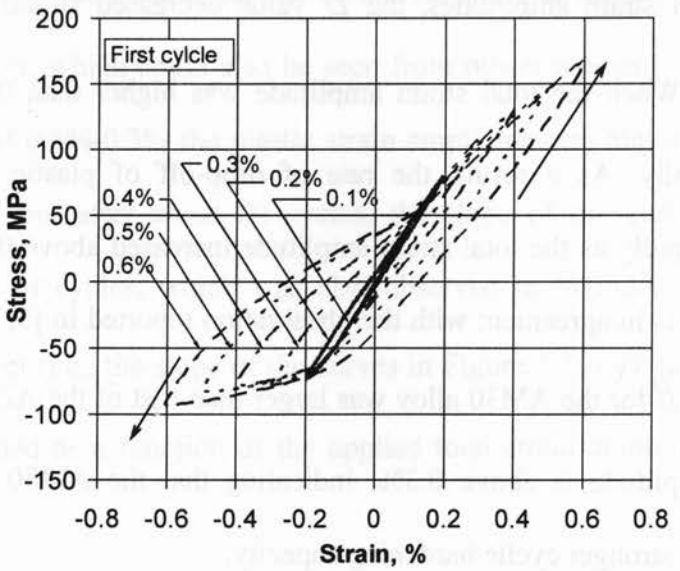

Figure 5.12 (a): Hysteresis loops at the very first cycle for AM30 alloy.

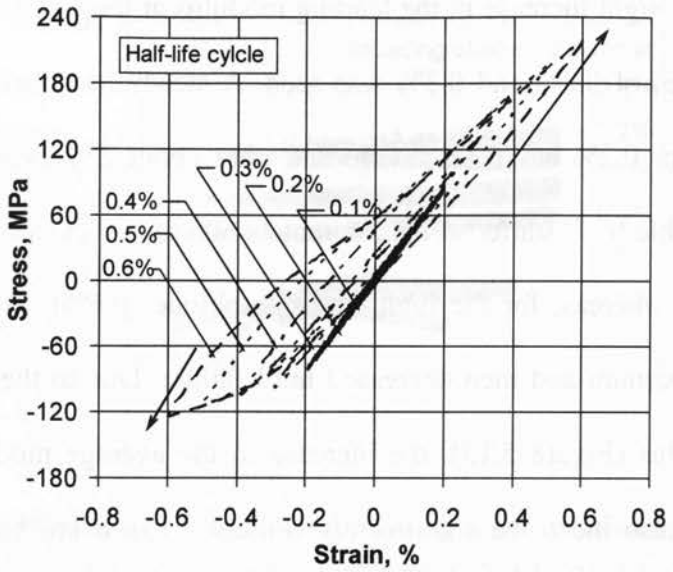

Figure 5.12 (b): Hysteresis loops at the half-life cycle for AM30 alloy.

5.4.3 Change of Modulus of Elasticity during Cyclic Deformation

The variation of modulus of elasticity during cyclic deformation of extruded AM30 was evaluated. Figures 5.13 and 5.14 shows the change of modulus of elasticity during the loading and unloading phases over the entire fatigue life. Figure 5.15 shows the variation of the average modulus of elasticity as a function of the number of cycles. The initial modulus of elasticity at the beginning of low cycle fatigue was higher at small strain amplitudes, which remained almost constant. The increase in the total strain amplitudes led to a decrease in the initial modulus in both loading and unloading phases (Figures 5.13 and 5.14). While the unloading modulus exhibited only a small change with respect to the number of cycles (Figure 5.14), the loading modulus increased as the cyclic deformation progressed, especially at the higher strain amplitudes (Figure 5.13). The loading modulus at a strain amplitude of 0.1% had no change throughout the entire

fatigue process. A slight increase in the loading modulus at the early stage of fatigue life at strain amplitudes of 0.2% and 0.3% was seen. A steady modulus was reached after about 50 cycles for 0.2% strain amplitude and after about 250 cycles for 0.3% strain amplitude. The stable level started at approximately 600 to 850 cycles for 0.4% and 0.5% strain amplitudes, whereas, for the high strain amplitude (0.6%), the loading modulus increased to a maximum and then decreased until failure. Due to the strong increase in the loading modulus (Figure 5.13), the increase in the average modulus at the higher strain amplitudes also increased significantly (Figure 5.15), even though the unloading modulus remained relatively stable (Figure 5.14) as the cyclic deformation proceeded.

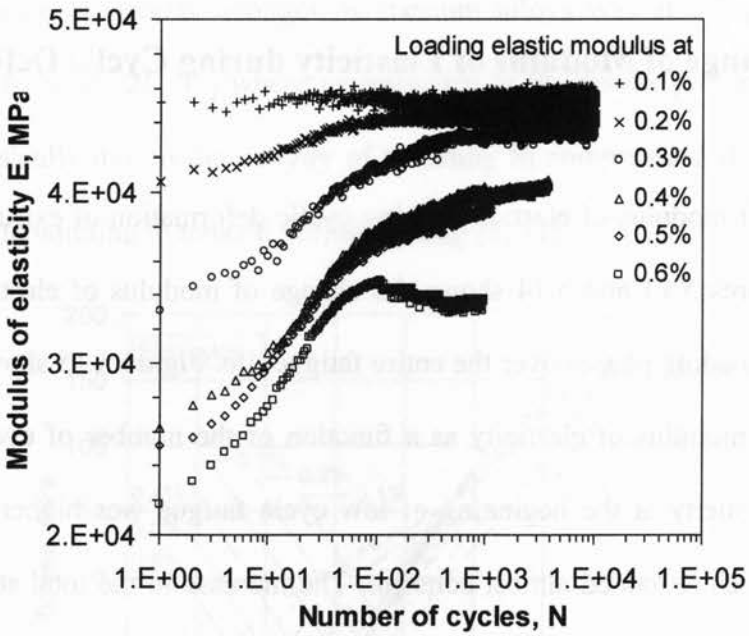

Figure 5.13: Variation of loading modulus with the number of cycles at different strain amplitudes for AM30 alloy.

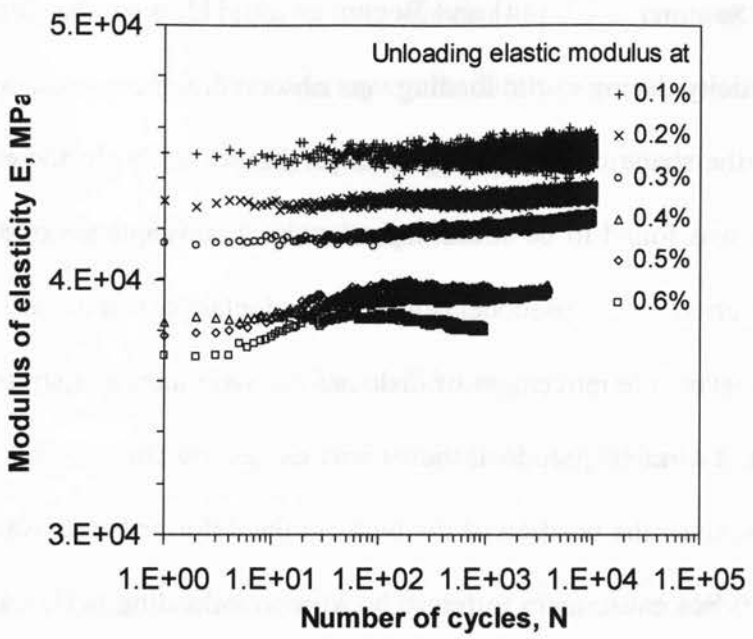

Figure 5.14: Variation of unloading modulus with the number of cycles at different strain amplitudes for AM30 alloy.

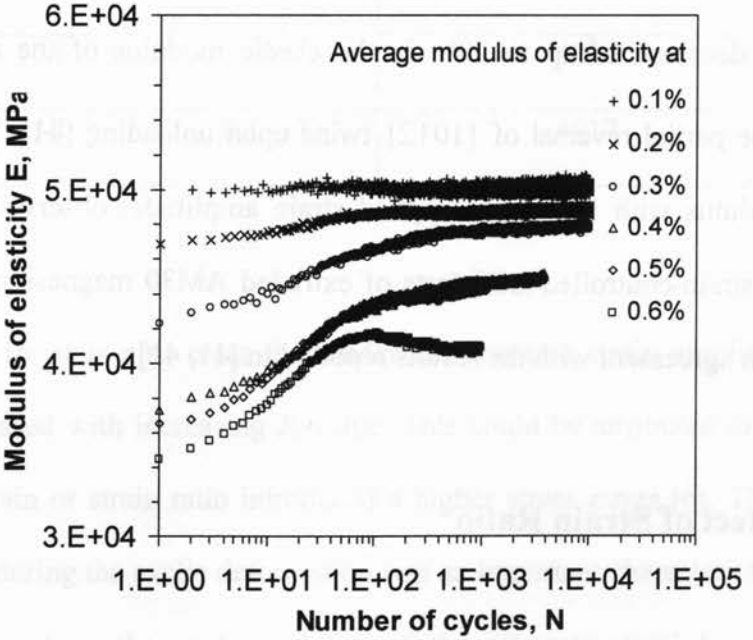

Figure 5.15: Variation of average modulus with the number of cycles at different strain amplitudes for AM30 alloy.

As reported by Sommer *et al.* [44] and Begum *et al.* [11], a similar dependence of the modulus of elasticity during cyclic loading was observed, which was associated with the asymmetries in the shape of the hysteresis loops (Figure 5.12). In the earlier work, the elastic modulus was found to be stress-dependent as a consequence of nonlinear elastic effects, also referred to as pseudoelasticity. Pseudoelasticity may arise from several origins such as reversible movement of dislocations, twinning, and stress induced phase transformations. Twinning pseudoelasticity was caused by the reversible movement of twin boundaries, since the position of the twins in the deformed state was not stable, and a driving force could cause them to return back upon unloading [41]. Caceres *et al.* [41] examined the change of elastic modulus in a cast AZ91 magnesium alloy using tensile loading-unloading procedures, and observed that, with increasing plastic strain up to 1-2%, the elastic modulus decreased drastically, i.e., the anelastic or pseudoelastic strain could cause a decrease of up to 70% in the elastic modulus of the alloy. This was attributed to the partial reversal of $\{10\bar{1}2\}$ twins upon unloading [41]. The decrease of the elastic modulus with increasing applied strain amplitude, observed in the present fully-reversed strain-controlled LCF tests of extruded AM30 magnesium alloy (Figures 5.13-5.15), is in agreement with the results reported in [11, 41].

5.4.4 Effect of Strain Ratio

To examine the effect of strain ratio on the fatigue characteristics of AM30 magnesium alloy, varying strain ratios were applied at a strain amplitude of 0.4% and a strain rate of 1×10^{-2} s^{-1}. The resulting fatigue lives are listed in Table 5-1. It is seen that the fatigue life

increased with decreasing strain ratio, which is similar to that observed in the AZ31 alloy. The evolution of the stress amplitude during cyclic deformation is shown in Figure 5.16. It is of interest to observe that, at the lower (negative) strain ratio, the material showed higher strain hardening than at the higher strain ratio.

Table 5-1: Strain-controlled push-pull low cycle fatigue life data obtained at different strain ratios under an applied strain amplitude of 0.4% and strain rate of 1×10^{-2} s^{-1} for AM30.

Strain ratio, R_s	**Mean strain,** ε_{mean}, **%**	**Number of cycles to failure,** N_f
0.5	1.2	2085
0	0.4	3858
-1	0	4211
-2	-0.13333	4917

From Figure 5.16, it is also clear that under the constant strain amplitude, the stress amplitude increased with increasing R_s value. This could be attributed to the fact that a higher mean strain or strain ratio introduced a higher stress range [6]. The evolution of stress response during the cyclic deformation was an important characteristic of low cycle fatigue process, where the cyclic stability of the microstructural features related to dislocation multiplication mainly dominated the cyclic stress response [46].

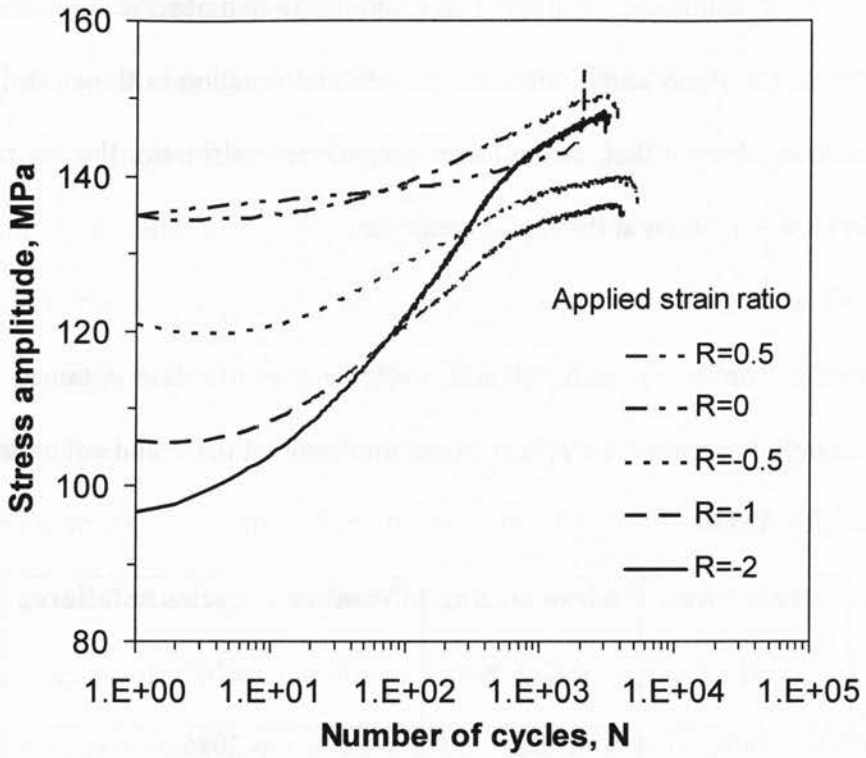

Figure 5.16: Stress amplitude vs. the number of cycles at a strain amplitude of 0.4% under different strain ratios (R_s) for AM30 alloy.

Figure 5.17 shows the variation of the plastic strain amplitude with the number of cycles at different applied strain ratios, R_s. It is seen that, at a high strain ratio of 0.5, there was a sudden drop of the plastic strain amplitude from cycle 1 to cycle 2 and then it remained almost constant until failure. As the R_S value decreased from 0.5 to 0, the magnitude of the sudden change in the plastic strain amplitude decreased. Such a sudden drop disappeared as the R_S value became negative (-0.5, -1, and -2). The plastic strain amplitude after the second cycle decreased with increasing R_S value and increasing number of cycles, especially at lower strain ratios.

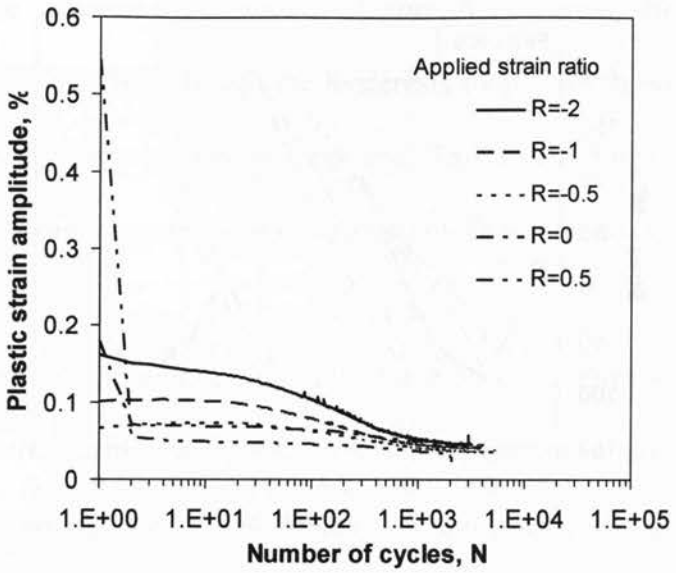

Figure 5.17: Plastic strain amplitude vs. the number of cycles at a strain amplitude of 0.4% under different applied strain ratios (R_s) for AM30 alloy.

The first cycle hysteresis loops and approximate half-life hysteresis loops for each strain ratio at a constant strain amplitude of 0.4% are shown in Figure 5.18 and Figure 5.19, respectively. It is seen from Figure 5.18 that a higher asymmetric deformation occurred at lower strain ratios than at higher strain ratios.

The hysteresis loop at R_s=-2 appeared more skewed than that at R_s=-1 and, eventually it became symmetric at R_s=0.5. At the lower strain ratio, more twins would be generated due to the fact that the lower mean strain gave rise to a more negative compressive stress. Also, detwinning during the tensile loading required a lower stress than the stress needed to activate twinning during the compressive loading. This might also affect the change in the plastic strain amplitude (Figure 5.17).

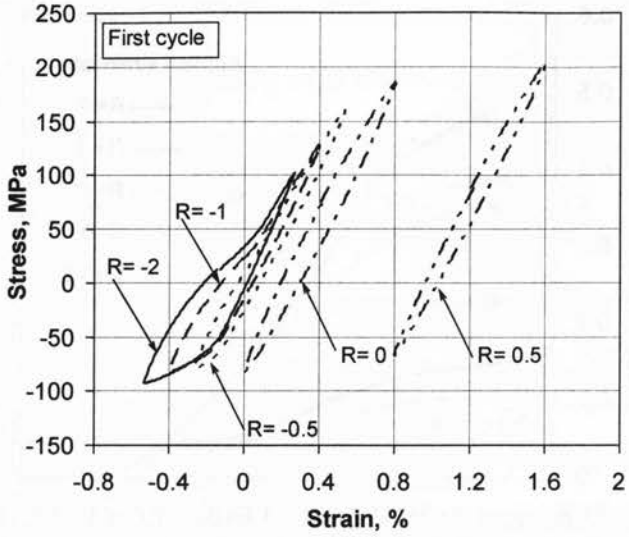

Figure 5.18: Hysteresis loops at the first cycle for different applied strain ratios (R_s) at a strain amplitude of 0.4% for AM30 alloy.

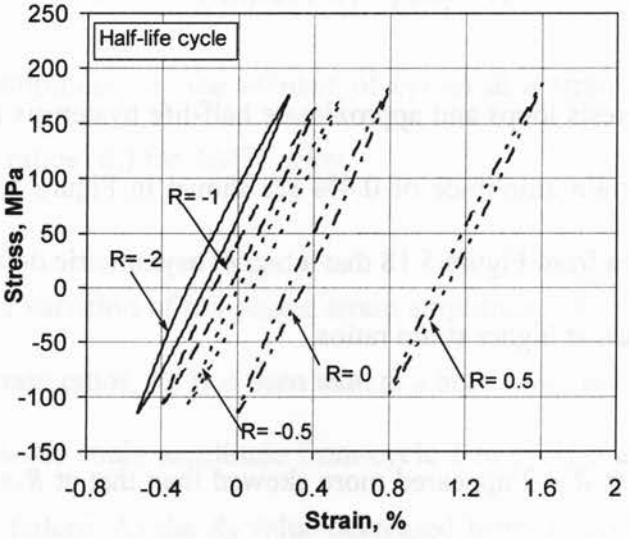

Figure 5.19: Hysteresis loops at the half-life cycle for different applied strain ratios (R_s) at a strain amplitude of 0.4% for AM30 alloy.

At the higher strain ratio R_s=0.5 the skewness of the hysteresis loop disappeared. This is due to the introduction of a higher mean strain and subsequent higher mean stress which

might lead to the absence of twinning. Figure 5.19 shows the hysteresis loops approximately at the half life. Though the hysteresis loops looked normal, a tensile and compressive stress asymmetry was still present. This is attributed to the tensile and compressive yield asymmetry observed in wrought magnesium alloys [39].

Plots of mean stress vs. the number of cycles for each strain ratio are shown in Figure 5.20. It is evident that, at the lower strain ratio a smaller mean stress evolved and the mean stress increased till 600 cycles, which was close to the half life cycle, then it became relatively stabilized. This is in good agreement with the test results reported by Goodenber and Stephens [9]. With increasing strain ratio, the mean stress significantly increased. However, it decreased with increasing number of cycles, representing the mean stress relaxation.

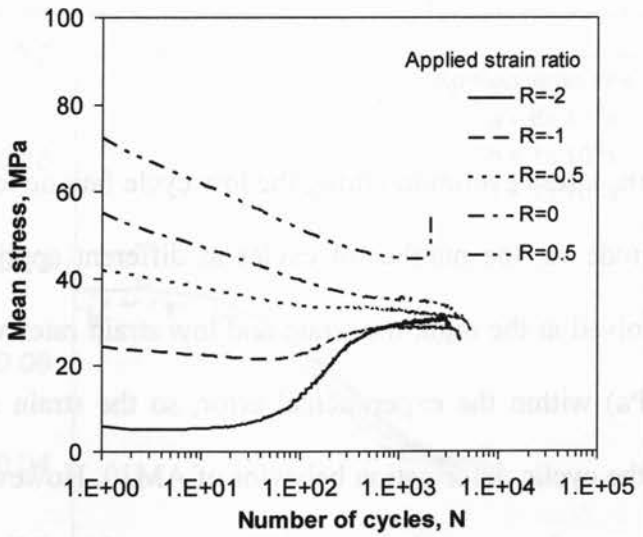

Figure 5.20: Mean stress vs. the number of cycles for different applied strain ratios (R_s) at a strain amplitude of 0.4% for AM30 alloy.

5.4.5 Effect of Strain Rate

Three strain rates ($\dot{\varepsilon}$) were applied to examine the effect of strain rate on the fatigue life of the AM30. Table 5-2 listed the fatigue life obtained at different strain rates. It is seen that the fatigue life increased with increasing strain rate. The same trend was also observed in AZ31 extruded Mg alloy.

Table 5-2: Variation of fatigue lifetime with the strain rate at a strain amplitude of 0.4% and strain ratio of -1 for AM30 alloy.

Strain rate, s^{-1}	**Number of cycles to failure, N_f**
1×10^{-3}	3437
1×10^{-2}	4211
8×10^{-2}	5716

.

Figure 5.21 shows the stress evolution during the low cycle fatigue tests, which is plotted as the stress amplitude vs. the number of cycles at different applied strain rates. The stress amplitude evolved at the high, moderate and low strain rates was almost the same (about 105-109 MPa) within the experimental error, so the strain rate had basically a marginal effect on the cyclic deformation behavior of AM30. However, cyclic hardening occurred at all three strain rates. Similarly, there was no big difference in the plastic strain amplitude vs. the number of cycles (Figure 5.22) and the mean stress vs. the number of cycles (Figure 5.23) at different applied strain rates. Similar results were obtained for the extruded AZ31B alloy [57].

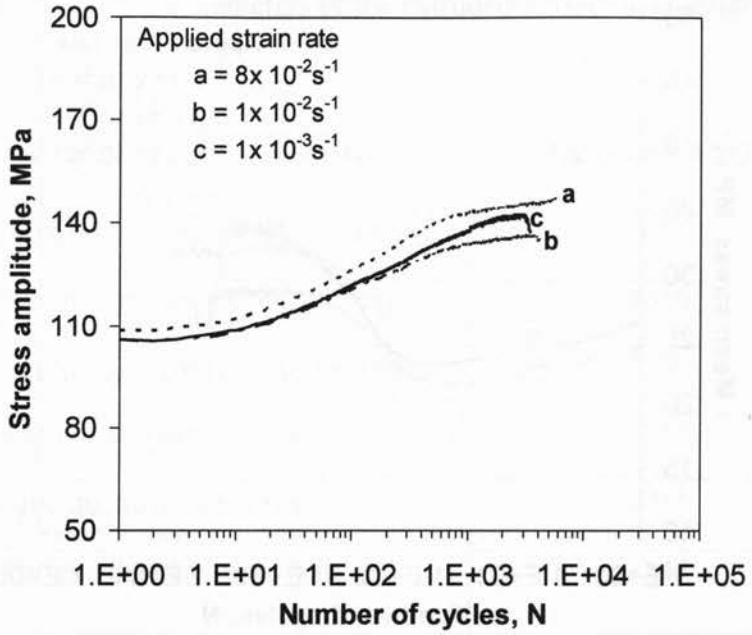

Figure 5.21: Stress amplitude vs. the number of cycles at a strain amplitude of 0.4% and strain ratio of -1 at different strain rates for AM30 alloy.

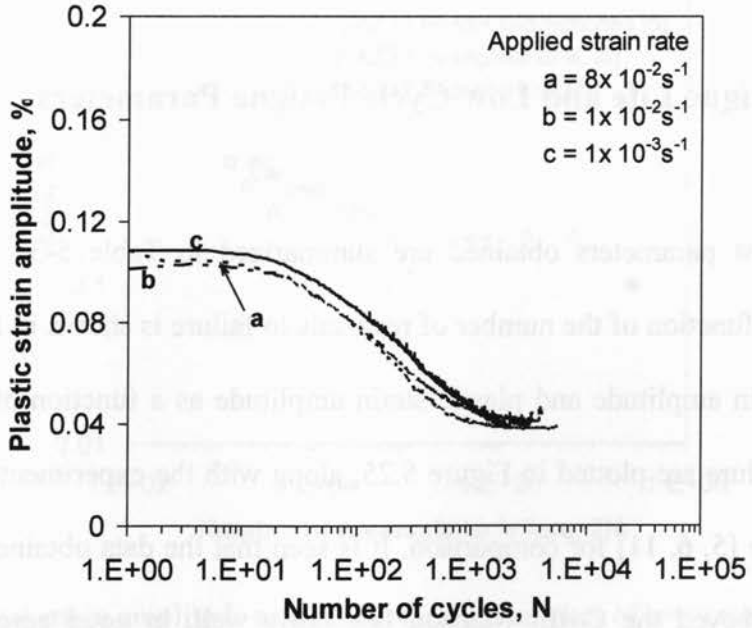

Figure 5.22: Plastic strain amplitude vs. the number of cycles at a strain amplitude of 0.4% and strain ratio of -1 at different strain rates for AM30 alloy.

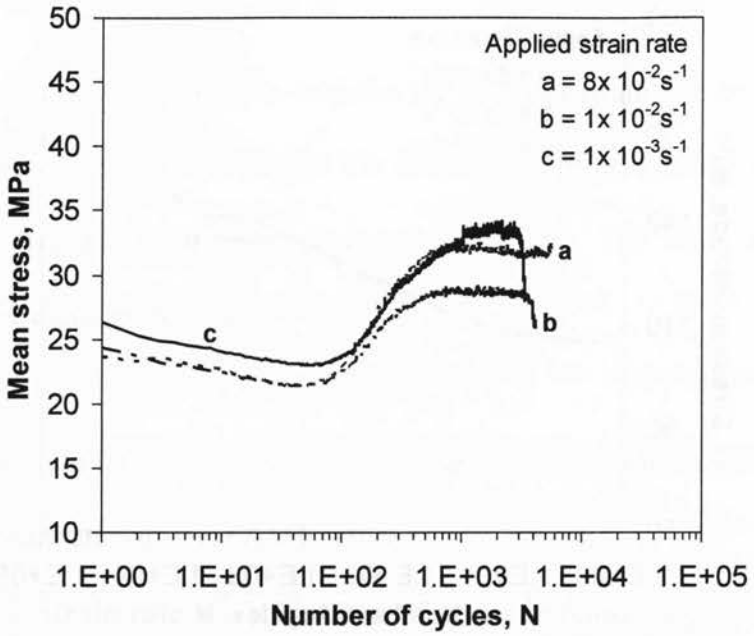

Figure 5.23: Mean stress vs. the number of cycles at a strain amplitude of 0.4% and strain ratio of -1 at different strain rates for AM30 alloy.

5.4.6 Fatigue Life and Low Cycle Fatigue Parameters

The fatigue test parameters obtained are summarized in Table 5-3. The total strain amplitude as a function of the number of reversals to failure is shown in Figure 5.24, and the elastic strain amplitude and plastic strain amplitude as a function of the number of reversals to failure are plotted in Figure 5.25, along with the experimental data obtained in the literature [5, 6, 11] for comparison. It is seen that the data obtained in the present investigation obeyed the Coffin-Manson law fairly well, in good agreement with the literature data [5, 6, 11].

Table 5-3 Low cycle fatigue parameters of the extruded AM30 magnesium alloy.

Low Cycle fatigue parameters	Extruded AM30
Cyclic strain hardening exponent, n'	0.33
Cyclic strength coefficient, K', MPa	1610
Fatigue strength coefficient, $\sigma_f^{'}$, MPa	678
Fatigue strength exponent, b	-0.16
Fatigue ductility coefficient, $\varepsilon_f^{'}$, %	2.97
Fatigue ductility exponent, c	-0.44

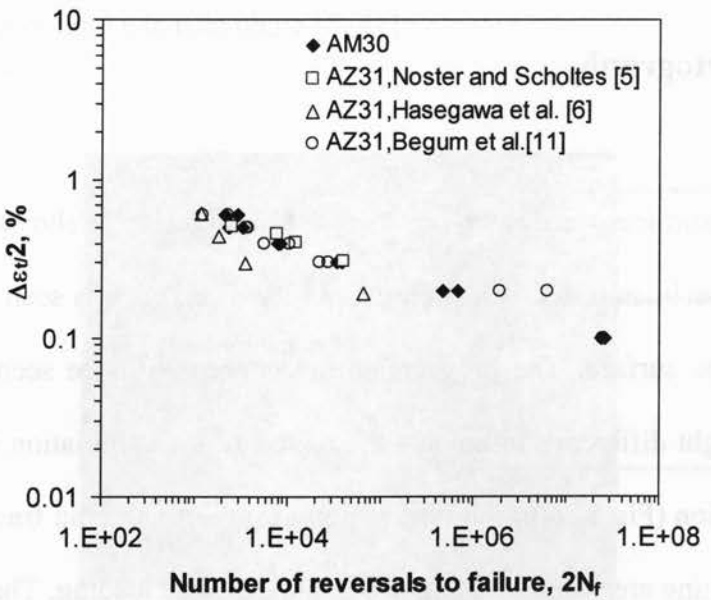

Figure 5.24: Total strain amplitude as a function of the number of reversals to failure.

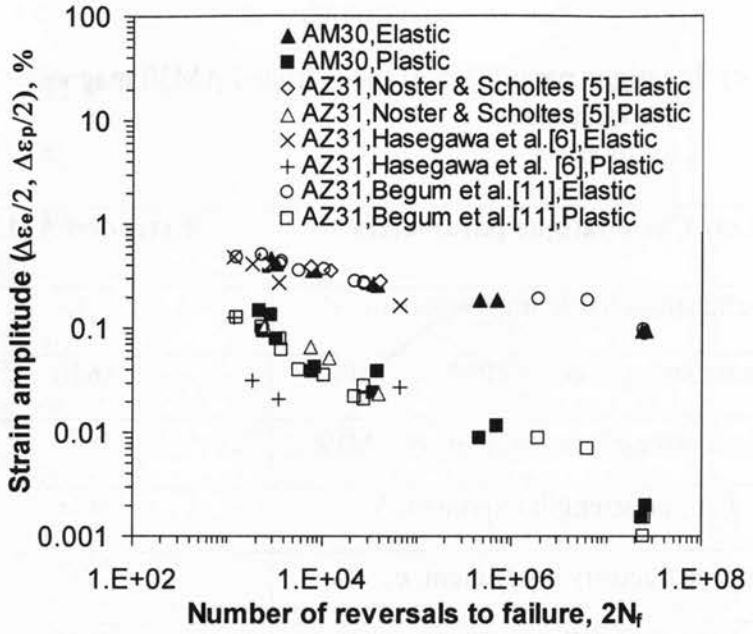

Figure 5.25: Elastic strain amplitude and plastic strain amplitude as a function of the number of reversals to failure.

5.4.7 Fractography

Fatigue fracture surfaces were examined using SEM. Figure 5.26 shows a typical fracture surface of the specimen tested at a strain amplitude of 0.2%. It is seen that fatigue crack initiated from the surface. The propagation area appeared to be seen as three regions based on the slight difference in color – the region near the initiation site (Fig.5.26(b)), intermediate region (Fig.5.26(c)) and the region near the final rapid fracture (Fig.5.26(d)) where the remaining area cannot sustain the applied fatigue loading. The propagation was basically characterized by fatigue striations, in conjunction with tear ridges in the region near the initiation site (Fig.5.26(b)) and a mixture of tear ridges with some secondary cracks and quasi-cleavage facets in the region close to the final rapid fracture

(Fig.5.26(d)). At higher strain amplitudes, multiple crack initiation sites were observed, as shown in Figure 5.27 (0.4%) and Figure 5.28 (0.6%). At higher strain amplitudes, the crack initiation from the corner (the intersection of two surfaces of the specimen) was also seen. These observations indicated that the inside of the extruded AM30 Mg alloy had a fairly high resistance to the crack initiation even through some inclusion particles were present in the material (Figure 5.1). Again, the fatigue crack propagated basically in the form of striations (whose spacing increased with increasing distance from the initiation site) shown in Figure 5.27 (c), together with some tear ridges and cleavage-like facets. While the fatigue striations normally occurred by a repeated plastic blunting-sharpening process in face-centered cubic materials due to the slip of dislocations in the plastic zone at the fatigue crack tip [23, 58], the formation of the fatigue striations in the extruded magnesium alloy was expected to be related to the twinning in the compressive phase and detwinning in the tensile phase [8, 41].

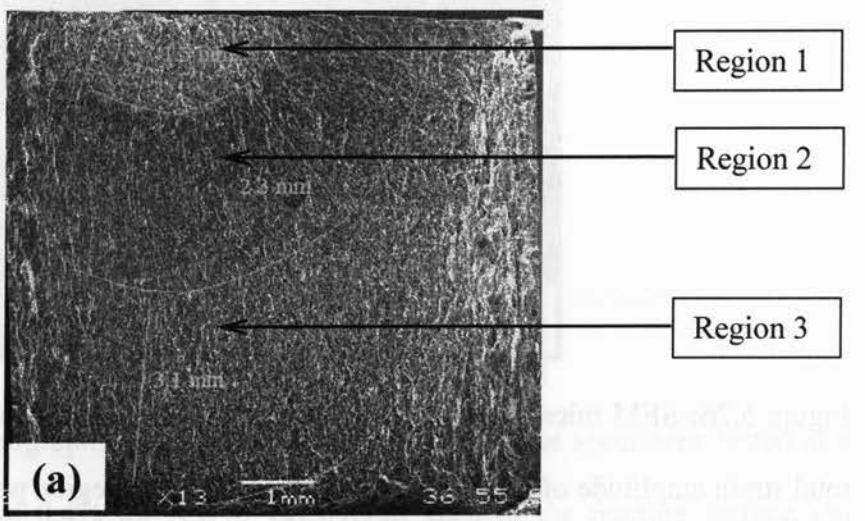

Figure 5.26: SEM micrographs of fatigue fracture surfaces of the specimens tested at a total strain amplitudes of 0.2% for AM30, (a) overall view of the fracture surface.

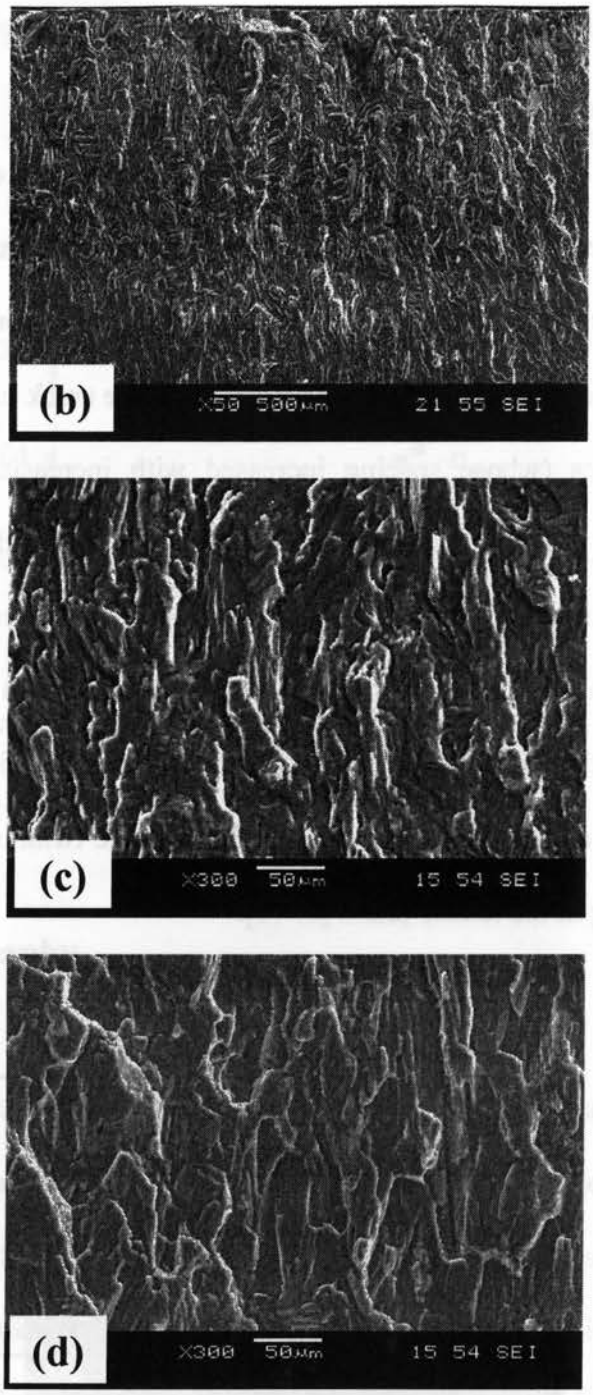

Figure 5.26: SEM micrographs of fatigue fracture surfaces of the specimens tested at a total strain amplitude of 0.2% for AM30, b) propagation region near the initiation site, (c) intermediate propagation region, (d) propagation region near the final rapid fracture.

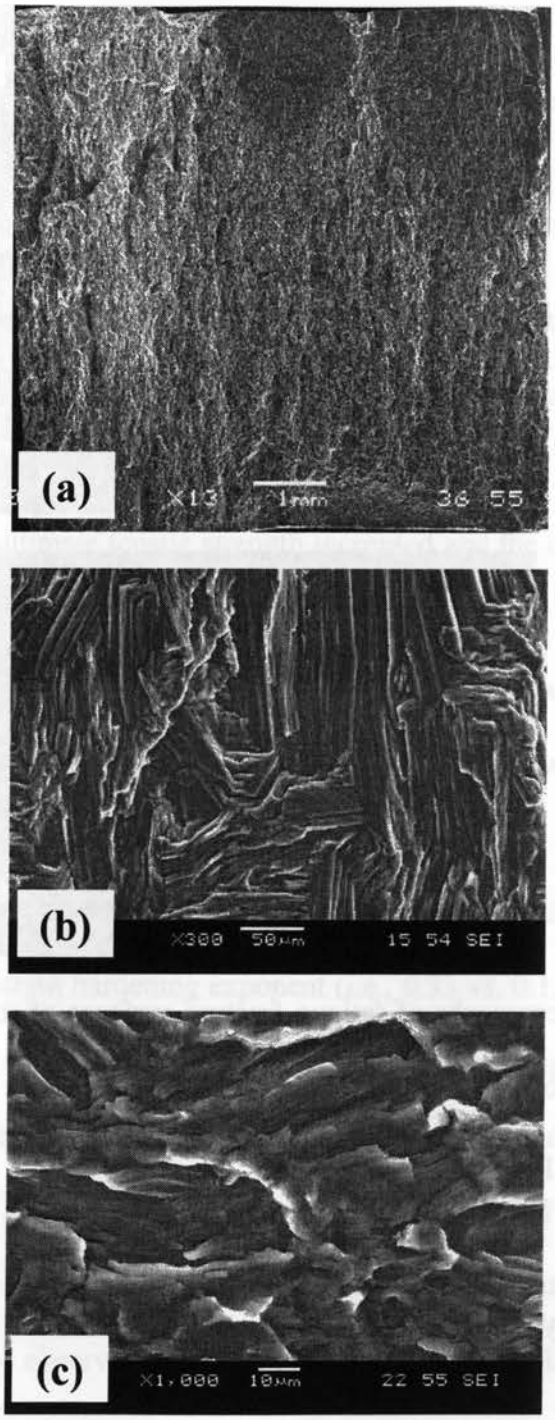

Figure 5.27: SEM micrographs of fatigue fracture surfaces of the specimens tested at a total strain amplitude of 0.4% for AM30, (a) overall view of the fracture surface, (b) magnified view of the initiation area, and (c) crack propagation area with striation-like features.

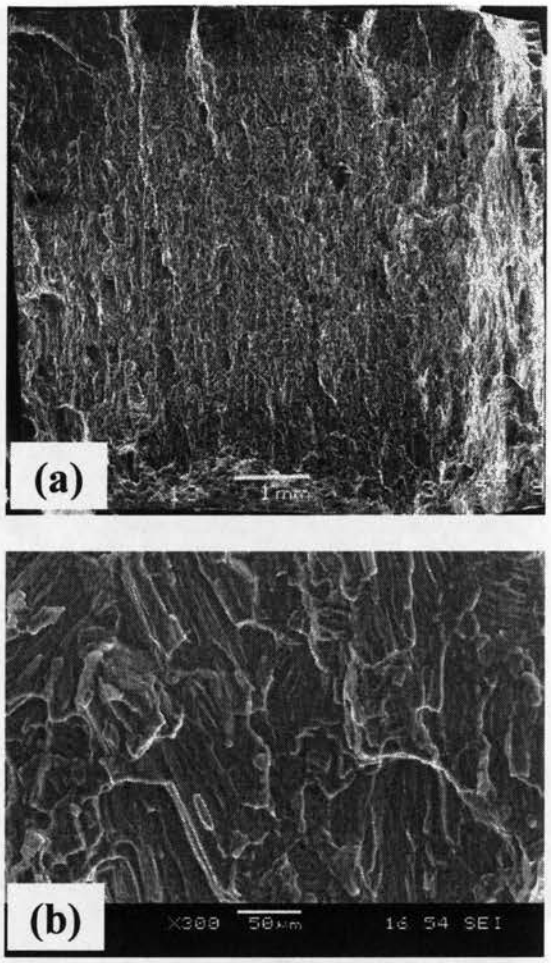

Figure 5.28: SEM micrographs of fatigue fracture surfaces of the specimens tested at a total strain amplitude of 0.6% for AM30, (a) overall view of the fracture surface, and (b) magnified view of the propagation area.

5.5 Summary

1. Microstructural observation of AM30 across the thickness on the cross section of the longitudinal sample showed a non-uniform grain distribution, with a grain size ranging from about 8 μm to about 44 μm. Larger grain sizes were observed near

the top and bottom surfaces, whereas the middle section exhibited small grains of about 15 μm surrounded by clusters of further small grains of about 8 μm.

2. Micro-hardness of this alloy basically varied from 32 to 48 HV due to the non-homogeneous grain size distribution.
3. Tensile tests showed a higher strain hardening exponent at high strain rates which changed from 0.19 to 0.15 from $1\times10^{-5}s^{-1}$ to $1\times10^{-2}s^{-1}$, which led to a different trend but a higher value of the strain hardening exponent than that of AZ31. The yield strength, ultimate tensile strength increased and the ductility decreased with increasing strain rate.
4. Strain controlled fatigue tests of AM30 showed that, at low strain amplitudes, the cyclic stress amplitude basically remained constant; while, at higher strain amplitudes, cyclic hardening occurred until failure.
5. The cyclic strain hardening exponent of AM30 was found to be also higher than the monotonic strain hardening exponent (i.e., 0.33 vs. 0.15) obtained at the same strain rate of $1\times10^{-2}\ s^{-1}$, indicating stronger cyclic hardening capacity.
6. Plastic strain amplitudes decreased with increasing number of cycles after an initial period of a nearly constant value. This corresponded to the cyclic hardening and the increase in the mean stress. The absolute value of cyclic hardening coefficient β was observed to increase with increasing strain amplitude. The mean stress also increased with increasing strain amplitudes.
7. A big difference between the tensile and compressive yield stresses was observed, leading to asymmetric hysteresis loops. This was mainly due to the occurrence of

twinning in the compressive phase and subsequent detwinning in the tensile phase during cyclic deformation.

8. The alloy exhibited non-linear or pseudoelastic cyclic deformation behavior. The elastic modulus during cyclic deformation, being constant at the low strain amplitude, was observed to decrease with increasing strain amplitudes and increase with increasing number of cycles at the high strain amplitudes.
9. The fatigue lifetime decreased with increasing strain amplitude. The Coffin-Manson law and the Basquin equation could be used to describe the fatigue life.
10. Tests conducted at different strain ratios revealed that the lower the strain ratio (or the lower the mean strain), the lower the stress amplitude and mean stress and the stronger the cyclic hardening, but the higher the plastic strain amplitude. This gave rise to a longer fatigue life.
11. While the strain rate seemed to have no significant effect on the cyclic hardening characteristics of AM30 at a strain amplitude of 0.4%, the fatigue life increased with increasing strain rate.
12. Fractography revealed that fatigue cracks initiated from the specimen surface, regardless of the total strain amplitude applied, due to the larger grain sizes at the specimen surface. Multiple initiation sites at the specimen surface or corner were observed at higher strain amplitudes.
13. Fatigue crack propagation was mainly characterized by fatigue striation-like features. The spacing of fatigue striations increased with increasing distance from the initiation site.

CHAPTER 6

CONCLUSIONS AND FUTURE WORK

6.1 Conclusions

1. Microstructural examination revealed that both AZ31 and AM30 showed a non uniform grain distribution along the plate thickness. AZ31 showed a higher variation in the grain size than did AM30. The grain size of AZ31 varied from 60 μm to 6 μm, whereas the grain size of AM30 varied from 44 μm to 8 μm.

2. Tensile tests at different strain rates showed AM30 had a high strain hardening exponent than did AZ31. Unlike the usual trend of increasing value of n with increasing strain rate, AM30 showed an opposite trend. The decrease in the n value for AM30 at higher strain rate, revealed the softening effect. Compared to AZ31 alloy, the higher strain hardening exponent of AM30 indicated slightly better formability than AZ31.

3. Strain controlled fatigue tests showed that, at low strain amplitudes, the stress amplitude basically remained constant for both AZ31 and AM30, while, at higher strain amplitudes, AM30 showed higher cyclic hardening than did AZ31 until failure.
4. Plastic strain amplitudes decreased with increasing number of cycles after an initial period of a nearly constant value. This corresponded to the cyclic hardening

and the increase in the mean stress for both AZ31 and AM30. The absolute value of the cyclic hardening coefficient, β, was observed to increase with increasing strain amplitude. At low strain amplitudes, β for both the alloys was almost the same but, as the strain amplitude increased, β of AM30 increased much more than that of AZ31. This also indicated that AM30 had a higher hardening effect than did AZ31.

5. A big difference between the tensile and compressive yield stress was observed for both AZ31 and AM30, leading to asymmetric hysteresis loops. However, AM30 showed stronger asymmetric hysteresis shape than AZ31. At the very first cycle, the asymmetry in the tensile and compressive yield stresses was much stronger than at the half-life cycle. The higher strain amplitude applied led to stronger asymmetry than did the lower strain amplitude. This was mainly due to the occurrence of twinning in the compressive phase and subsequent detwinning in the tensile phase during cyclic deformation.

6. Both alloys exhibited non-linear or pseudoelastic cyclic deformation behavior. The elastic modulus during cyclic deformation, being constant at the low strain amplitude, was observed to decrease with increasing strain amplitude and increase with increasing number of cycles at the high strain amplitudes. Moreover, the elastic modulus of AM30 was somewhat lower than that of AZ31, but the increase of loading modulus with increasing number of cycles was higher for AM30 than for AZ31.

7. It was observed that both alloys followed the Coffin-Manson law and the Basquin equation very well. The fatigue parameters following the two equations and the equation representing the cyclic stress-strain curve were evaluated for the estimation of fatigue life of both alloys.

8. Tests conducted at different strain ratios for both AZ31 and AM30 revealed that the lower the strain ratio (or the lower the mean strain), the lower the stress amplitude and mean stress and the stronger the cyclic hardening, but the higher the plastic strain amplitude. The overall effect of these changes gave rise to a longer fatigue life. However, for AM30 at the lower strain ratio the strain hardening effect was seen to be stronger than that of AZ31.

9. The effect of strain rate on the cyclic deformation characteristics of AZ31 and AM30 seemed to be not so significant, but the fatigue lives of both alloys were observed to increase with increasing strain rate.

10. The tensile start was observed to result in slightly greater cyclic hardening, larger plastic strain amplitude and higher mean stress, giving rise to a slightly shorter fatigue life for AZ31.

11. SEM examinations of AZ31 alloy revealed that fatigue cracks initiated from the specimen surface due to the larger grain sizes near the specimen surface. The initiation site contained cleavage-like facets, which were observed to decrease as

the strain amplitude increased. However, the flat cleavage-like facets were absent in the initiation site of the AM30 specimens, though the crack initiated from the surface due to the presence of large grains. Multiple initiation sites at the specimen surface or corner were observed at higher strain amplitudes.

12. Fatigue crack propagation of both AZ31 and AM30 was basically characterized by fatigue striation-like features, coupled with the presence of the secondary cracks. The spacing of fatigue striations increased with increasing distance from the initiation sites.

A summary on the tensile and fatigue parameters of both AZ31 and AM30 alloys tested in the present investigation is tabulated in Table 6-1. Tensile properties obtained at a strain rate of $1\times10^{-2}s^{-1}$ only are given in the table, since the low cycle fatigue tests are conducted at the same strain rate. By comparing the tensile properties of AZ31 and AM30 it can be concluded that even though AZ31 has higher yield strength and ultimate tensile strength, the strain hardening exponent of AM30 is higher than AZ31. This would reflect the better formability of AM30 than AZ31. Therefore, AM30 could be deformed at 1.5 times higher extrusion speed than AZ31. While some differences of fatigue parameters between AZ31 and AM30 alloys could be seen in Table 6-1, the fatigue lifetime is almost the same for both AZ31 and AM30 alloys, especially in the low cycle fatigue regime.

Table 6-1: Tensile and fatigue properties of AZ31 and AM30 alloys at a strain rate of $1\times10^{-2}s^{-1}$.

	Properties	AZ31	AM30
Tensile:	Yield strength, MPa	199	189
	Ultimate tensile strength, MPa	264	242
	Elongation, %	15.2	13.4
	Strain hardening exponent, n	0.137	0.145
Fatigue:	Cyclic strain hardening exponent, n'	0.34	0.33
	Cyclic strength coefficient, K', MPa	1976	1610
	Fatigue strength coefficient, $\sigma_f^{'}$, MPa	616	678
	Fatigue strength exponent, b	-0.15	-0.16
	Fatigue ductility coefficient, $\varepsilon_f^{'}$, %	1.78	2.97
	Fatigue ductility exponent, c	-0.40	-0.44

6.2 Scope of Future Work

The research in the field of magnesium for more than decades has greatly improved. The properties of pure magnesium and some useful alloys of magnesium have been developed. For high duty structural applications, such as components that work under high pressure and temperature especially in the LCF conditions, researchers are considering magnesium as a promising alloy, which leads to more and more research efforts in this field. The

structural applications of magnesium alloys inevitably involve the dynamic or alternating loads in service. In case of LCF, the fatigue crack propagation may not be a dominant factor due to the high stresses applied. It can be assumed that the crack propagation in the HCF consumes most of the fatigue life, but, in the LCF, once the crack initiates the crack propagates very quickly, leads to a fast failure. Therefore, the crack initiation in the LCF plays a critical role. Studies on the LCF behavior of magnesium alloys can be used to identify the mechanism and mode of the failure under low cycle fatigue, the microstructural effect, slip characteristics, dislocation nature, and twinning effect on the low cycle fatigue. The obtained results would provide direct guidelines for developing fatigue resistant lightweight structural magnesium alloys for automotive and aerospace applications.

1. In this study, the microstructure and mechanical properties of AZ31 and AM30 in the extrusion or longitudinal direction were investigated. Considering the fact that Mg alloys have a HCP structure and its texture alignment has a great effect on the mechanical properties of this alloy, it would be of interest if the LCF tests can be done for the transverse direction (i.e., perpendicular to the extrusion direction). So far, few studies have been reported on the fatigue properties along the transverse direction for AZ31, and no results have been seen for AM30 in this aspect.

2. Load control fatigue tests for AM30 would be another interesting aspect in future works since no such results have been reported in the literature.

3. The observed pseudoelastic behavior in both alloys is an interesting characteristic. This kind of behavior is only observed in the low cycle fatigue tests. It is probably related to the time-dependent deformation. However, to understand the mechanisms of the time-dependent deformation, future work needs to be done in this area.

4. Micro-crack propagation behavior during fatigue deformation would also be an important aspect for both AZ31 and AM30.

5. Considering the defect or damage tolerant design, the fatigue crack propagation behavior of both AZ31 and AM30 needs to be evaluated.

REFERENCES

[1] K.U. Kainer, Magnesium Alloys and Technology, Wiley-VCH, Cambridge, 2003.

[2] H.E. Friedrich, B.L. Mordike, Magnesium Technology- Metallurgy, Design Data, Applications, Springer-Verlag Berlin Heidelberg, Germany, 2006.

[3] A.A. Luo, Magnesium: Current and potential automotive applications, JOM (Journal of Metals), 2002, 54(2), 42-48.

[4] A.A. Luo, Wrought magnesium alloys and manufacturing processes for automotive applications, SAE 2005 Transactions - Journal of Materials and Manufacturing, SAE, Warrendale, PA, U.S.A., 411-421.

[5] U. Noster and B. Scholtes, Isothermal strain-controlled quasi-static and cyclic deformation behavior of magnesium wrought alloy AZ31, Z. Metallkd, 2003, 94(5), 559-563.

[6] S. Hasegawa, Y. Tsuchida, H. Yano and M. Matsui, Evaluation of low cycle fatigue life in AZ31 magnesium alloy, Inter J. Fatigue, 2007, 29, 1839-1845.

[7] U. Noster and B. Scholtes, Cyclic deformation behavior of magnesium alloys AZ31 and AZ91 in the temperature range 20-300°C, Mater. Sci. Forum, 2003, 419-422, 103-108.

[8] L. Wu, A. Jain, D.W. Brown, G.M. Stoica, S.R. Agnew, B. Clausen, D.E. Fielden and P.K. Liaw, Twinning- detwinning behavior during the strain controlled low cycle fatigue testing of a wrought magnesium alloy, ZK60A, Acta Materialia, 2008, 56, 688-695.

[9] D.L. Goodenber and R.I. Stephens, Fatigue of AZ91E-T6 cast magnesium alloy, Journal of Engineering Materials and Technology, 1993, 115, 391-397.

[10] L. Feng, W. Yue, C. Lihia, L. Zheng and Z. Jiyang, Low-cycle fatigue behavior of two magnesium alloys, J. Mater. Sci., 2005, 40, 529-1531.

[11] S. Begum, D.L. Chen, S. Xu and A.A. Luo, Low cycle fatigue properties of extruded AZ31 magnesium alloy, International Journal of Fatigue (2008), doi: 10.1016/j.ijfatigue.2008.03.009.

[12] L. Chen, C. Wang, W. Wu, Z. Liu, G.M. Stoica, L. Wu, and P.K. Liaw, Low-cycle fatigue behavior of an as-extruded AM50 magnesium alloy, Metallurgical and Materials Transactions A, 2007, 38A, 2235-2241.

[13] Z. Liu, Z.G. Wang, Y.L. Wang, H. Chen, H.J. Zhao and F. Klein, Cyclic deformation behavior and fatigue crack propagation in AZ91HP and AM50HP, Mater. Sci. Technology, 2001, 17(3), 264-268.

[14] A.A. Luo and A.K. Sachdev, AM30-a new wrought magnesium alloy, Magnesium technology, 2007, TMS, 321-326.

[15] A. Staroselsky and L. Anand, A constitutive model for HCP materials deforming by slip and twinning: application to magnesium alloy AZ31B, International Journal of Plasticity, 2003, 19, 1843–1864.

[16] W.F. Smith, Structure and properties of Engineering alloys, McGraw-Hill, Inc, New York, 1993.

[17] E. El-Magd and M. Abouridouane, Characterization, modeling and simulation of deformation and fracture behavior of the light-weight wrought alloys under high

strain rate loading, International Journal of Impact Engineering, 2006, 32, 741-758.

[18] T. Yokoyama, Tensile and compressive properties of wrought magnesium alloys at high strain rates, Journal of Physics, 2003, 110, 69-74.

[19] L. Jiang, J.J. Jonas, A.A. Luo, A.K. Sachdev and S. Godet, Microstructural and texture evolution during the uniaxial tensile testing of AM30 magnesium alloy, Magnesium Technology, 2006, TMS, 233-238.

[20] C.S. Roberts, Magnesium and its alloys, John Wiley & Sons Incorporated, New York, 1960.

[21] S. Xu, V.Y. Gertsman, J. Li, J.P. Thompson and M. Sahoo, Role of mechanical twinning in tensile compressive yield asymmetry of die cast Mg alloys, Canadian Metall. Quarterly, 2005, 44(2), 155-166.

[22] M.H. Yoo, J.R. Morris, K.M. Ho and S.R. Agnew, Nonbasal deformation modes of HCP metals and alloys: role of dislocation source and mobility, Metallurgical and Materials Transactions A, 2002, 33A, 813-822.

[23] G.E. Dieter, Mechanical Metallurgy, McGraw-Hill series, USA, 1986.

[24] A. Serra, D.J. Bacon, and R.C. Pond, Twins as barriers to basal slip in hexagonal close-packed metals, Metallurgical and Materials Transactions A, 2002, 33A, 809-812.

[25] M. Marya, L.G. Hector, R. Verma and W. Tong, Microstructural effects of AZ31 on its tensile deformation and failure behavior, Mater. Sci. Eng. A, 2006, 418, 341-356.

[26] Y. Yunqi, Z. Tingjie, D. Ju, Z. Lian, C. Changqi and L. Peiying, Microstructural evolution and tensile properties features of wrought Mg-Nd alloy, Rare Metal Materials and Engineering, 2005, 34 (6), 845-849.

[27] S. Suresh, Fatigue of Materials, 2nd edition, Cambridge University Press, 1998, 132-133, 141-143, 149-152, 165-168, 179-180.

[28] S.S. Manson, Thermal stress and low cycle fatigue, McGraw Hill Book Company, New York, 1960.

[29] C. Potzies and K.U. Kainer, Fatigue of magnesium alloys, Advanced Engineering Materials, 2004, 6(5), 281-289.

[30] V.V. Ogarevic and R.I. Stephens, Fatigue of magnesium alloys, Annual Reviews of Materials Science, 1990, 20, 141-177.

[31] Y. Kobayashi, T. Shibusawa and K. Ishikawa, Fatigue crack propagation behavior of magnesium-aluminum alloy in air and argon, Proc. of the 6th International Fatigue Congress, Berlin, 1996, Vol. I, 703.

[32] Annual Book of ASTM Standards, Standard test methods for tension testing of metallic materials [Metric], Designation: ASTM E 8M - 04, Vol. 03.01, 2006, 88-111.

[33] Annual Book of ASTM Standards, Standard practice for Strain-Controlled fatigue testing, Designation: ASTM E 606-04(2004), Vol. 03.01, 2006, 611-626.

[34] M.R. Barnett, Z. Keshavarz, A.G. Beer and D. Atwell, Influence of grain size on the compressive deformation of wrought Mg-3Al-1Zn, Acta Mater., 2004, 52, 5093-5103.

[35] M.M. Myshlyaev, H.J. McQueen, A. Mwembela and E. Konopleva, Twinning, dynamic recovery and recrystallization in hot worked Mg-Al-Zn alloy, Mater. Sci. Eng. A, 2002, 337, 121-133.

[36] A.A. Salem, S.R. Kalidindi, R.D. Doherty and S.L. Semiatin, Strain hardening due to deformation twinning in [alpha]-titanium: mechanisms, Metall. Mater. Trans. A, 2006, 37A, 259-268.

[37] D.W. Brown, S.R. Agnew, M.A.M. Bourke, T.M. Holden, S.C. Vogel and C.N. Tome, Internal strain and texture evolution during deformation twinning in magnesium. Mater. Sci. Eng. A, 2005, 399, 1-12.

[38] M.R. Barnett, Twinning and ductility of magnesium alloys: Part I "Tension" twins. Mater. Sci. Eng. A, 2007, 464, 1-7.

[39] J.P. Nobre, U. Noster, M. Kornmeier, A.M. Dias and B. Scholtes, Deformation asymmetry of AZ31 wrought magnesium alloy, Key Eng. Mater., 2002, 230-232, 267-270.

[40] F. Thomas, U. Noster, B. Scholtes and P. Uggowitzer, Microstructural influences on the cyclic deformation behavior of magnesium wrought alloys, Proceedings of the 2nd International Light Metals Technology Conference, Switzerland, 2005.

[41] X.Y. Lou, M. Li, R.K. Boger, S.R. Agnew and R.H. Wagoner, Hardening evolution of AZ31B Mg sheet, Inter. J. Plasticity, 2007, 23, 44-86.

[42] Y.N. Wang and J.C. Huang, The role of twinning and untwinning in yielding behavior in hot-extruded Mg–Al–Zn alloy, Acta Mater., 2007, 55, 897-905.

[43] E.A. Ball and P.B. Prangnell, Tensile-compressive yield asymmetries in high strength wrought magnesium alloys, Scripta Metall. Mater., 1994, 31(2), 111-116.

[44] C. Sommer, H.J. Christ and H. Mughrabi, Non-linear elastic behavior of the roller bearing steel SAE 52100 during cyclic loading, Acta Metall. Mater., 1991, 39(6), 1177-1187.

[45] C.H. Caceres, T. Sumitomo and M. Veidt, Pseudoelastic behaviour of cast magnesium AZ91 alloy under cyclic loading–unloading, Acta Mater., 2003, 51, 6211-6218.

[46] M.H. Yoo, S.R. Agnew, J.R. Morris and K.M. Ho, Non-basal slip systems in HCP metals and alloys: source mechanisms, Materials Science and Engineering A, 2001, 319-321, 87-92.

[47] Q. Gaofeng, Twinning and twinned bands turning during plastic deformation in rolled Mg alloy AZ31, Key Engineering Materials, 2007, 345-346, 717-720.

[48] R. Gehrmann, M.M. Frommert and G. Gottstein, Texture effects on plastic deformation of magnesium, Materials Science and Engineering A, 2005, 395, 338-349.

[49] N. Munroe and X. Tan, Orientation dependence of slip and twinning in HCP metals, Scripta Mataialia, 1997, 36(12), 1383-1386.

[50] L. Jiang, J.J. Jonas, R.K. Mishra, A.A. Luo, A.K. Sachdev and S. Godet, Twinning and texture development in two Mg alloys subjected to loading along three different strain paths, Acta Materialia, 2007, 55, 3899-3910.

[51] S.M. Yin, H.J. Yang, S.X. Li, S.D. Wua and F. Yanga, Cyclic deformation behavior of as-extruded Mg–3%Al–1%Zn, Scripta Materialia, 2008, 58, 751-754.

[52] D.W. Brown, A. Jain, S.R. Agnew and B. Clausen, Twinning and detwinning during cyclic deformation of Mg alloy AZ31B, Mater. Sci. Forum, 2007, 539-543, 3407-3413.

[53] H. Zenner and F. Renner, Cyclic material behavior of magnesium die castings and extrusions, International Journal of Fatigue, 2002, 24, 1255-1260.

[54] G. Robert, M.F. Matthias and G. Gunter, Texture effects on plastic deformation of magnesium, Materials Science and Engineering A, 2005, 395, 338-349.

[55] M. Norman and T. Xiaoli, Orientation dependence of slip and twinning in HCP metals, Scripta Mataialia 1997, 36 (12), 1383-1386.

[56] J. Levesque, K. Inal, K.W. Neale, R.K. Mishra, A.A. Luo and L. Jiang, Numerical modeling of large strain deformation in magnesium alloy AM30, Magnesium technology, 2007, 11-16.

[57] S. Begum, D.L. Chen, S. Xu and A.A. Luo, Effect of strain ratio, strain rate and initial strain direction on the fatigue behavior of AZ31 wrought magnesium alloy, MRS-2008 International Materials Research Conference, Chongqing, China, June, 2008, submitted to Journal of Materials Research (under review).

[58] C. Laird, Fatigue Crack Propagation, ASTM STP 415, 1967, 131-168.

SANJIDA BEGUM

EDUCATION

Master of Applied Science (August 2008)
Ryerson University, Toronto, ON
Major: Mechanical Engineering
Bachelor of Applied Science (Feb 2003)
Bangladesh University of Engineering & Technology, Bangladesh
Major: Mechanical Engineering

EXPERIENCE

Teaching Assistant, Sep. 2006- Aug 2008
Ryerson University, Toronto, ON, Canada

Junior Mechanical Engineer, Mar 2003- Jul 2005
Omni Technologies Co., Dhaka, Bangladesh

AWARDS

Ryerson Graduate Scholarship for academic excellence, 2006-2008
Ryerson Graduate Stipend, 2006-2008
Bangladesh Government Merit Scholarship, 1997-2003

LIST OF PUBLICATIONS (over the past two years during my MASc. study)

A. Refereed journal papers (accepted or under review):

1. S. Begum, D.L. Chen, S. Xu and A.A., Luo Low cycle fatigue properties of extruded AZ31 magnesium alloy, ***International Journal of Fatigue*** (2008), in print, doi: 10.1016/j.ijfatigue.2008.03.009.
2. S.Begum, D.L.Chen, S.Xu and A.A.Luo, Strain-controlled low cycle fatigue properties of a newly developed extruded magnesium alloy, submitted to ***Metallurgical and Materials Transactions A***, 2008 (under review).
3. S. Begum, D.L. Chen, S. Xu and A.A. Luo, Effect of strain ratio, strain rate and initial strain direction on the fatigue behavior of AZ31 wrought magnesium alloy, selected as one of "the top 4% original research papers" by the Symposium Organizers at the MRS-2008 International Materials Research Conference, Chongqing, China, June 9-12, 2008, and recommended to submit to ***Journal of Materials Research*** (under further review).
4. A.R.Emami, S. Begum, D.L. Chen, T. Skszek, Y. Zhang and F. Gabbianelli, Cyclic deformation behavior of a cast aluminum alloy, to be submitted to ***Materials Science and Engineering A*** (currently under the review of Magna COSMA International).

B. Conference presentations:

1. S.Begum, D.L.Chen, S.Xu and A.A.Luo, Mechanical properties of an extruded AZ31 alloy, the 20th Canadian Materials Science Conference, Edmonton, Alberta, edited by R. Eadie and T. Etsell, Met Soc, June 16-19, 2008, p.2. (oral presentation given by S.Begum).
2. S.Begum, D.L.Chen, S.Xu and A.A.Luo, Fatigue properties of an extruded AM30 alloy, the 20th Canadian Materials Science Conference, Edmonton, Alberta, edited by R. Eadie and T. Etsell, Met Soc, June 16-19, 2008, p.24. (poster given by S.Begum). This poster was also shown at 2008 AUTO21 Conference, London, Ontario, June 2-4, 2008.
3. S.Begum, D.L.Chen, S.Xu and A.A.Luo, Effect of strain ratio, strain rate and initial strain direction on the fatigue behavior of AZ31 wrought magnesium alloy, Abstracts Book, MRS International Materials Research Conference, Chongqing, China, June 9-12, 2008, p.301. (oral presentation given by Dr. Chen).